BOSE-EINSTEIN CONDENSATION IN SPIN DIMER COMPOUNDS

A DISSERTATION
SUBMITTED TO THE DEPARTMENT OF APPLIED PHYSICS
AND THE COMMITTEE ON GRADUATE STUDIES
OF STANFORD UNIVERSITY
IN PARTIAL FULFILLMENT OF THE REQUIREMENTS
FOR THE DEGREE OF
DOCTOR OF PHILOSOPHY

Suchitra E. Sebastian
March 2006

© Copyright by Suchitra E. Sebastian 2006
All Rights Reserved

I certify that I have read this dissertation and that, in my opinion, it is fully adequate in scope and quality as a dissertation for the degree of Doctor of Philosophy.

Dr. Ian R. Fisher Principal Advisor

I certify that I have read this dissertation and that, in my opinion, it is fully adequate in scope and quality as a dissertation for the degree of Doctor of Philosophy.

Dr. Neil Harrison

I certify that I have read this dissertation and that, in my opinion, it is fully adequate in scope and quality as a dissertation for the degree of Doctor of Philosophy.

Dr. Sebastian Doniach

I certify that I have read this dissertation and that, in my opinion, it is fully adequate in scope and quality as a dissertation for the degree of Doctor of Philosophy.

Dr. Malcolm R. Beasley

Approved for the University Committee on Graduate Studies.

Acknowledgements

Above all, I thank God for joy, laughter, passion, and a universe full of wonder. I am thankful that my time at Stanford has been immeasurably enriched by unforgettable friends and colleagues, whom I shall always cherish.

The Fisher group members have been truly delightful to work with, they have survived my whimsical ways with admirable aplomb, and have managed to create a fun workplace where physics is only a part of what we do. Ian, thank you for being a nurturing advisor I have grown under and learnt from, for not being afraid to give me the flexibility to experiment until I found my own path through the research maze - and for sharing in my delight when I did. From physics facts of life: 'no, all magnets are *not* metals', to laboratory survival rules: acid does *not* go well with metal, *nor* sticky tape with the SQUID, and much more... I learnt, you survived, thank you! Yana, thank you for your superheroic abilities in keeping me unscathed and moderately responsible in lab, Kyungyun for your philosophical outlook on life and all its curious ways, tales of which never failed to cause us merriment, Ann for your unflappable calm and optimism even amidst chaos. Nancy and I might have spent more hours reflecting on life and planning creative activities than we did working in lab together - thank you for being my enthusiastic partner in crime, for keeping me laughing and encouraging me while I was low, and for being all-in-all an incomparable lab mate. All the undergrads who endured my tender mercies

- Tony, Brian, David, Philip, Peter and Michael, thank you for being cheerful and willing inspite of tasks that were not always fun, and for your undimmed wonder. Philip, thank you for friendship, food, flippancy, balloon animals, liquid Nitrogen ice cream, and the joy you took in plunging wholeheartedly into whatever surprising thing our research together entailed - I couldn't find a better research companion.

Los Alamos was my 'lab away from lab', I might not be too enthusiastic about the city, but the lively people I interacted with at the magnet lab more than made up for what the city lacked in charm. Paul and Ross, thank you for putting up with the ridiculously long hours and for making my magnet time surprisingly fun... we'll win that million someday. Paul, thank you for mirth-filled companionship - for keeping me laughing through the most distressful magnet situations, and for rescuing me from clouds of Helium. Peter, John, Vivien, Chuck, Pat and Alex, thank you for the support, encouragement and magnet shots. Marcelo, Cristian and Neil, thank you for co-opting me into an amazing research team. It was the most intense, and yet doubtless the most enjoyable and rewarding experience of my time in graduate school - I learnt more from you than I could have imagined or hoped for, thank you for the fun-filled camaraderie and the truly infectious enthusiasm. Cristian, I learnt more theory from you than from all the books I've read, thank you for being the most willing, patient and encouraging teacher and collaborator. Neil, thank you for your devastating forthrightness, inimitable humour, ability to enliven the most mundane situation, and for being an unparalleled teacher - in expecting the impossible from me, but making sure I got there somehow, aided by your unique brand of physical intuition, experimental skill and flair for 'unboringisation'.... and for ducks, escapes from dented Jags, and prank emails. Luis,

thank you for making Tallahassee runs a smooth affair, and for putting up with our continuously changing plans and my unceasing mirth!

This thesis would not be complete if not for the numerous collaborators with whom I worked extensively through the course of my research, thanks to whom I was introduced to a rich variety of experimental techniques. Christian, Henrik and Des introduced me to the world of neutron scattering and French jazz clubs; Kenny, Catalin and Stan taught me about TDO's and more eventfully, how to make a sorb; Sergei and Jurek were the trusty ESR resource people; Yurij and Gordie showed what true crystallographers can do and helped our crystal characterisation efforts immeasurably; Raivo is in a sense this research project's godfather - thanks Raivo for introducing 'Han Purple' to Marcelo; Omid and Stephan showed me what Monte Carlo simulators do, and gave me my first experience as a seminar speaker... maybe some day I will understand why an audience member at that seminar raised the question of how much a box at the S.F. opera cost!

All my friends at GLAM - Droni, Corinna, Mark, Lily, Bob, Cyndi, Judy, Roberta, thank you for making working in GLAM such a pleasure, I appreciate your enthusiasm, love of life, and good cheer despite the attendant harum scarum of a research institution. Lily, thank you for everything - for food, laughter, sharing, cheering and teasing... for being a friend. Paula, thank you for rescuing me from all those desperate last-minute situations willingly and cheerfully - I've had the best times swapping stories in your office, your humour and refreshingly unorthodox views have always made me smile.

Much of what I have learnt during my time as a graduate student has been from walking the corridors of GLAM and knocking on various professors' doors... with-

out fail they have been gracious enough to give ear as I launched into my research mundanities, and have invariably offered profoundly useful insights. Several of those professors are on my thesis committee - an enormous thank you to Mac Beasley, Seb Doniach, Aharon Kapitulnik, Steve Kivelson, and Neil Harrison for signing away several hours of your already crowded schedules to be at my thesis defence. A special thanks also to Walt Harrison and Ted Geballe, who have helped me time and again with knotty research problems and encouraging words of advice. I am grateful to Martin Greven for generously permitting use of the image furnace for seemingly endless amounts of time!

David, thank you for being my unofficial mentor, for explaining the most basic of theories to me, and yet managing to introduce me to the most sophisticated of theoretical nuances... and for keeping it real. Cherrill, thanks for looking out for me - your oodles of practical advice, home-grown oranges and tips on how to survive the big bad world of physics, have kept me relatively unscathed through it all. Tanja and Hatice, thank you for being the most incredibly talented, fun, supportive and warm study group companions, I couldn't have survived those classes without you. Li, Guichuan and Eugene, thank you for all the help, generosity, companionship and encouragement during those long hours with the image furnace. Sonya, thank you for your warmth and generosity, and for making sure I got out of lab and had my dose of culture. I am grateful to the Mustard Seed foundation for financial support in the form of a Harvey Fellowship through my time at Stanford.

And finally, it is entirely inadequate to thank my mother - who has always been my biggest cheerleader: for dreams, for passion, for joyful abandon, for mirth and carefreeness, and for childlike delight... thank you.

Abstract

Magnetic materials and ultracold atomic gases are extremely disparate physical systems, yet universal principles of organization cause them to exhibit the identical phenomenon of 'Bose-Einstein condensation' (BEC) at low temperatures. This unique correspondence is established by an experimental study of magnetic spin-dimer materials in high magnetic fields, presented in this thesis. These model systems are especially attractive for experimentation, since the external magnetic field provides an experimental handle to tune the system in the vicinity of the quantum critical region.

Spin dimer materials consist of a weakly coupled network of spin pairs (dimers) such that the ground state at low magnetic fields is a direct product of singlets (i.e.) a quantum paramagnet. Novel magnetic order is observed above a critical magnetic field H_{c1} where the triplet and singlet levels become degenerate. Experimental results are presented here on two families of new materials in the rapidly developing class of spin dimer compounds.

Results from magnetisation, magneto-caloric effect, specific heat, magnetic torque, and inelastic neutron scattering measurements are presented on single crystals of $A_2Cu(BO_3)_2$ (A = Sr, Ba) and $BaCuSi_2O_6$. Critical scaling analysis was performed on the measured phase boundary separating the magnetically ordered phase from the paramagnetic phase in $BaCuSi_2O_6$, which has a relatively accessible crit-

ical magnetic field. Critical scaling analysis of the measured phase boundary reveals power law behaviour consistent with the three dimensional ($3d$) BEC universality class down to T $\sim$ 0.6 K, unambiguously identifying the ordered state as a $3d$ BEC of triplets, corresponding to a canted XY antiferromagnet

Extremely unusual critical scaling behaviour is observed in $BaCuSi_2O_6$ nearer the QCP, close to T $\sim$ 0.03 K, characteristic of the two dimensional ($2d$) BEC universality class. We identify inter-layer decoupling due to geometrical frustration as the mechanism responsible for this unique manifestation of a lower dimensional QCP in the $3d$ $BaCuSi_2O_6$ spin system. This is the first experimental realisation of dimensionally reduced criticality, and constitutes a proof of principle that dimensionality can become an emergent property of a QCP.

Contents

Chapter 1

Introduction

"Well my dear", said Miss Marple, "human nature is very much the same everywhere, and of course, one has opportunities of observing it at closer quarters in a village".

- 'The Tuesday Club Members', Agatha Christie

Much of research in condensed matter physics is about looking for patterns - in experiment and in theory, one searches for perceptible refrains, which taken together tell the whole story. Patterns are everywhere in nature - the 'frozen' groundstate of spin pyrochlores retains a residual (zero-point) entropy due to frustration just like hexagonal water ice [1], the quantum mirage effect seen in Kondo behaviour of the lone cobalt atom in a 'quantum corral' is similar to how sound waves are focused at resonance modes in a whispering gallery [2], vortices in superfluid ^{4}He transition from turbulent flow at low temperatures to regular laminar flow at higher temperatures like water flowing from a tap [3], ball bearings placed in a shallow bowl form spontaneous patterns like crystals; the list is endless. We understand some patterns better than we do others, for example - why does the outline of a lightning bolt mirror the spread of branches on a tree? There is as yet no good answer. To make my PhD research task simpler, the area

I chose to study focusses on the theoretically well-understood, but experimentally overlooked area of correspondences between bosonic and magnetic systems.

An analogy can be drawn between spin dimer systems comprising an arrangement of antiferromagnetically coupled pairs of $s = \frac{1}{2}$ spins (dimers) and hardcore bosonic systems, due to the integer spin of the constituent particles. The singlet groundstate ($s = 0$) of each dimer is interpreted as the absence of a hardcore boson, and the lowest triplet excited state ($s = 1$, $s^z = 1$) is interpreted as the presence of a hardcore boson [4]. The ground state of these systems in the absence of an external magnetic field is a disordered paramagnet comprising a product of singlets, described as 'empty' in terms of bosons; but at high magnetic fields, the lowest spin triplet state ($s = 1$, $s^z = 1$) enters the ground state, such that the system orders as an XY-antiferromagnet. The magnetically ordered state can be equivalently described as a network of interacting bosons, with particle density proportional to the magnetic field strength [5].

Spin dimer compounds in an external magnetic field, therefore provide a remarkable experimental opportunity to study dilute bosonic fluids for which the particle density is tuneable by way of the external magnetic field strength. Bosonic fluids are otherwise extremely challenging to create, a few examples of other systems which provide an experimental realisation of a bosonic fluid include cooled atomic gases [6], and exciton bilayers [7]. At very low temperatures, the groundstate of a bosonic fluid in which interparticle repulsive interactions dominate is a classical crystal. If on the other hand, the kinetic energy of the bosons dominates, the system condenses at low temperatures into a macroscopically occupied single-particle ground state known as a Bose-Einstein condensate (BEC) [8].

In this dissertation, results of experiments on two families of spin dimer compounds are discussed, both in which the kinetic energy drives the groundstate, which is therefore expected to be a spin realisation of a BEC. Experiments performed as part of my research were aimed

at better understanding the correspondence between these spin dimer materials and Bosonic systems. Of particular interest is the experimental study of areas of phase space for a Bosonic fluid which are currently experimentally inaccessible. One such important area is critical scaling behaviour in the vicinity of the quantum critical point separating the insulating and BEC groundstates. Due to the Heisenberg uncertainty principle, quantum systems have characteristic fluctuations that can drive phase transitions at zero temperature, known as quantum phase transitions (QPT).Second order QPT's occur at a singular quantum critical point (QCP) characterized by a diverging characteristic length. Since experimentally only finite temperatures can be accessed, the underlying QCP is identified by scaling behaviour characterising the approach toward absolute zero temperature. The QCP of an insulator to BEC transition induced by varying the chemical potential is particularly simple to understand, and its critical scaling properties have been theoretically well established [10; 11]. The order parameter of this quantum phase transition is the boson creation operator $\langle b^{\dagger} \rangle$, which means that the QCP is the point at which the number of bosons becomes finite, and they begin to condense. Spin dimer compounds are ideal systems in which to study this QCP, since we have direct experimental access to tune the boson density by varying the external magnetic field. In these systems, the QCP occurs at critical magnetic field $H_{\rm c1}$ at which the lowest spin triplet ($s = 1$, $s^z = 1$) becomes degenerate with the spin singlet state [4].

Fig. 1.1 shows the schematic phase boundary separating the disordered quantum paramagnetic phase from the XY-ordered BEC phase in the category of systems under study. A significant part of my research was to experimentally study the power law scaling that describes the approach of the phase boundary (that separates the disordered from the ordered ground state) towards the QCP. As will be described later, the scaling law describing the dependence of ordering temperature on the proximity to the QCP is expected to follow the universal power law behaviour $T_{\rm c} \propto (H - H_{\rm c1})^{\nu}$, where $\nu = 2/d$ (d = dimensionality of the system) for $d \geq 2$.

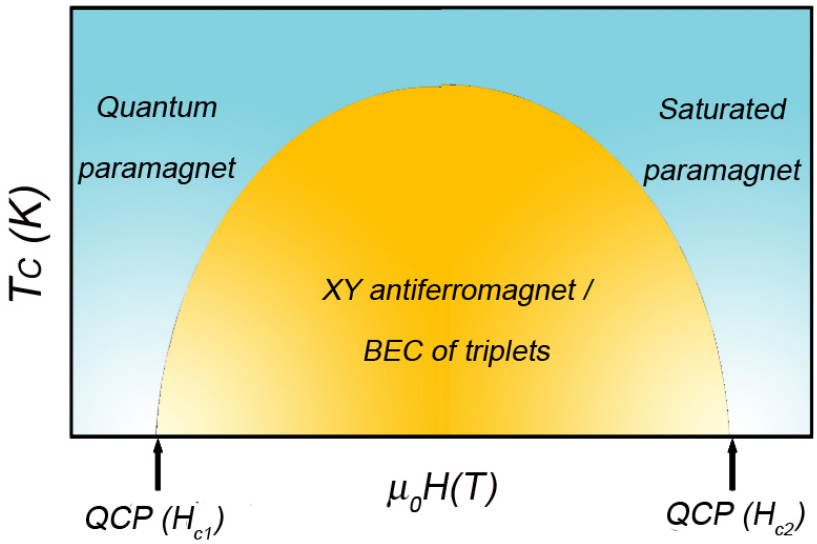

Figure 1.1. Phase boundary separating a quantum paramagnet from a BEC. Quantum properties drive collective behaviour in the vicinity of the QCP at H_{c1} and H_{c2} (lighter shading). The collective state of spins in a magnetically ordered system is analogous to condensed bosons in a BEC. The shape of the phase boundary determines the characteristic power law describing collective behaviour.

The critical exponent is dependent only on the dimensionality of the system, and not on other microscopic system details.

Experiments on the spin dimer compounds $A_2Cu(BO_3)_2$ (A=Sr, Ba) [31] and $BaCuSi_2O_6$ [12; 13] were carried out in high magnetic fields up to 65 T and low temperatures down to 0.03 K. Crystal growth techniques were developed to grow clean single crystals of these families of spin dimer compounds. Experiments conducted measured thermodynamic quantities such as magnetisation, magnetic torque, heat capacity and the thermal response to entropy conservation (through the magnetocaloric effect), each of which exhibit a clear feature at the ordering transition. The evolution of the ordering transition was mapped out as a function of temperature

and magnetic field to obtain the experimental phase boundary.

The experimental results obtained on the $BaCuSi_2O_6$ system, which is thought to be a realisation of a U(1) symmetric spin lattice, measured for the first time $\nu = 2/3$ power law behaviour characteristic of the $3d$-BEC universality class in the temperature range down to 0.6 K [12]. In unexpected fashion, the results also revealed an abrupt crossover to $\nu = 1$ behaviour characteristic of the $2d$-BEC universality class in the temperature range down to 0.03 K [13].

This is the first observation of a $2d$ QCP in a $3d$ material. While it is well known that the physical properties of a system are often substantially modified near the QCP due to the plethora of competing interactions in this region, the experimental observation of $2d$-BEC behaviour in the bulk $3d$-$BaCuSi_2O_6$ system is particularly surprising, being the first experimental observation of a change in dimension by tuning parameter space near the QCP. Careful study indicates that the dimensional reduction is a consequence of bilayer decoupling due to geometric frustration in the $BaCuSi_2O_6$ lattice, which is effective only at low particle densities near the amplitude fluctuation-driven QCP [13].

Future research directions are manifold. Experiments are currently underway to confirm that the U(1) rotational spin symmetry in the $BaCuSi_2O_6$ system is not explicitly broken by additional interaction terms or structural transitions to a lower symmetry, which would preclude a BEC. Experiments involving pressure as a tuning parameter instead of magnetic field are also underway, this experimental mapping of the phase boundary along another axis will provide a complement to the area of phase space accessed by high magnetic field measurements. Promising future experiments exploit the $2d$ QCP of this system characterised by purely $2d$ quantum fluctuations. $BaCuSi_2O_6$ provides us with a model system, which if doped with charge carriers, may prove ideal to test several theoretical predictions of novel phenomenon such as high temperature superconductivity resulting from $2d$-quantum fluctuations [14; 15; 16]. Other

promising experiments include exploring the dynamics of the vector ‘spin current’ carried by the BEC of triplets in these spin dimer compounds.

The outline of this dissertation is as follows: Chapter 2 contains relevant theoretical and materials specific background in two parts: in the first part, I describe specifics of the two families of spin dimer materials studied as part of the research presented in this dissertation, in the second part, I describe details of the analogy between these systems and bosonic systems, and derive the theoretical expressions used to compare with experimental results in the following sections. Chapter 3 contains experimental details of crystal growth techniques developed to grow these materials, and characterisation of single crystal quality. Chapter 4 describes specifics of the experimental systems used to perform measurements, particularly in high magnetic fields. Chapter 5 contains results of experiments on the $A_2Cu(BO_3)_2$ spin dimer systems and a discussion of those results. Chapter 6 contains results of experiments on the $BaCuSi_2O_6$ spin dimer systems and a discussion of those results. Chapter 7 provides a summary of the conclusions drawn from the research presented here, and Chapter 8 outlines future research ideas.

Chapter 2

Theoretical Background

"That's the whole problem with science. You've got a bunch of empiricists trying to describe things of unimaginable wonder." - Calvin (& Hobbes)

This chapter is divided into two parts, the first of which provides the reader with requisite background information about the specific materials we study as examples of the spin dimer class of systems; and the second of which describes the appropriate theoretical tools to map the spin dimer system onto a bosonic system, and derive scaling relations near the BEC QCP of a Bose gas.

2.1 Crystal structure

In this section, the two families of spin dimer compounds under study are discussed: $A_2Cu(BO_3)_2$ (A = Sr, Ba) and $BaCuSi_2O_6$. These materials are quasi-two dimensional Mott insulators, which comprise a lattice of Cu^{2+}($3d^9$, s = $\frac{1}{2}$) ions.

2.1.1 $Sr_2Cu(BO_3)_2$

$Sr_2Cu(BO_3)_2$ exists in two structural phases: the phase studied in this dissertation is high temperature β-$Sr_2Cu(BO_3)_2$. This material is in the PNMA space group, with an orthorhombic unit cell with lattice parameters a = 7.612 Å, b = 10.854 Å and c = 13.503 Å [17]. Two views of the quasi-two dimensional crystal structure are shown in figures 2.1 and 2.2. Fig. 2.1 shows the two-dimensional layers of $Cu_2B_4O_{12}$, which are separated from each other by Sr (Ba) ions [17] Fig. 2.2 shows a side view of the layers stacked above each other. Each layer comprises distorted octahedral Cu(1)O_6 units, square planar Cu(2)O_4 units and triangular B(1,2,3)O_3 units.

In a simple analysis of the structure shown in Fig. 2.1, the Cu^{2+} ions are seen to be coupled to their nearest neighbours via three different superexchange pathways (shown as J, J' and J'') via triangular BO_3 units. Orthorhombic distortion of the Cu(1)O_6 octahedra lifts the e_g degeneracy of this ion (apical oxygen ions are further from the central Cu(1) ion at 2.49 Å and 2.42 Å, than the equatorial oxygen ions, at 1.99 Å and 1.92 Å [17; 18]), such that the highest energy level is the antibonding combination of Cu $3d_{x^2-y^2}$ and the equatorial O $2p_\sigma$ orbitals (shown in Fig. 2.3b). Since the Cu(1) $3d^9$ hole resides in the equatorial plane, the dominant exchange pathway is therefore J, through the equatorial oxygen ions of the Cu(1)O_6 octahedra. The equivalent magnetic lattice then comprises planes of Cu(1)-Cu(2) dimers (a single dimer unit is shown in Fig. 2.3a) coupled by J via B(3)O_3 triangular units. The dimers are connected by the weak intra-layer coupling J' and J'', and inter-layer coupling can be considered weak enough for the layers to be treated as separated from each other. The equivalent magnetic lattice corresponding to each layer is represented by a network of Cu^{2+} ions linked by exchange interactions (shown in Fig. 2.4 a), which can be mapped to a square lattice of dimers (shown in Fig. 2.4 b). Inelastic neutron scattering experiments are in progress to more directly probe the network of exchange couplings.

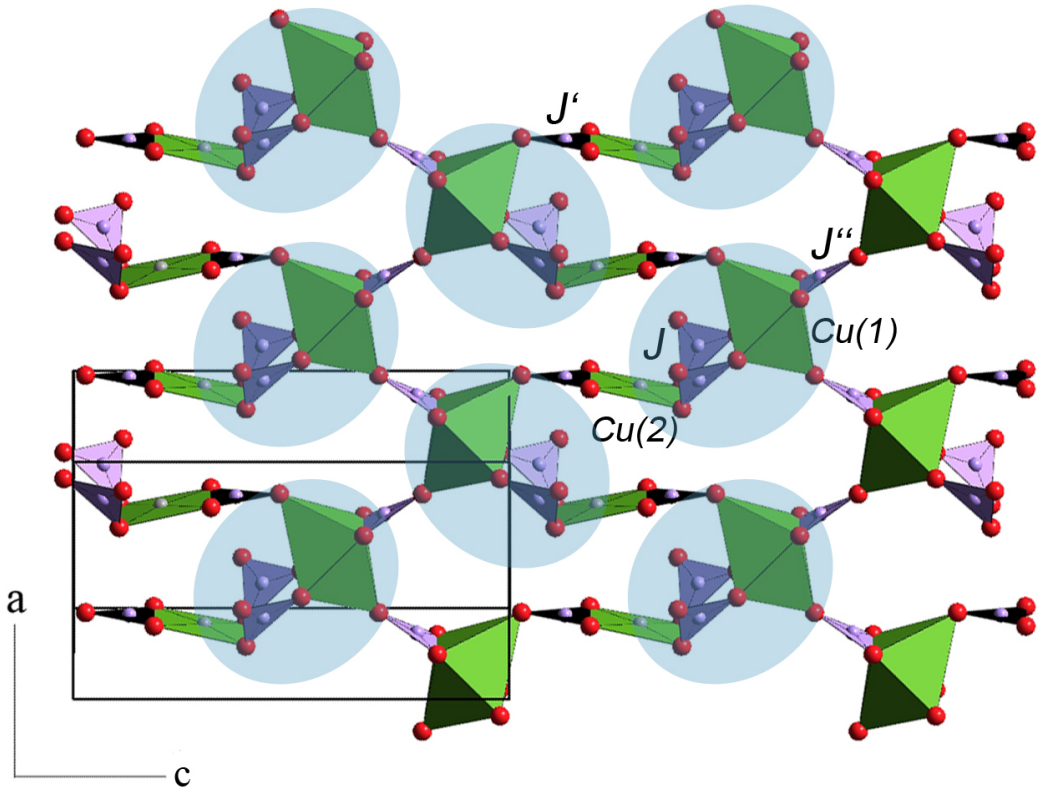

Figure 2.1. $Cu_2B_4O_{12}$ layers from $Sr_2Cu(BO_3)_2$. The red circles represent O, the green circles Cu and the purple circles B. The square planar units are $Cu(2)O_4$ groups, and the octahedra are $Cu(1)O_6$ groups. Dimer units (shaded) comprise Cu(1) and Cu(2) ions linked by an exchange interaction J via $B(3)O_3$ groups. Sr ions separating the layers are not shown. Solid lines show the unit cell. The $Cu_2B_4O_{12}$ plane has been tilted slightly out of the plane of the page to more clearly show the co-ordination of the Cu ions.

2.1.2 $Ba_2Cu(BO_3)_2$

The effect of substituting the larger Ba^{2+} ion (ionic radius 1.35Å) for Sr^{2+} (ionic radius 1.13Å) is to modify the exchange interactions through changes in bond lengths and angles. The Ba^{2+} substitution distorts the Cu(1)-O_6 octahedron even more than in $Sr_2Cu(BO_3)_2$. Table 2.1 lists the relevant bond lengths, and the incremental change between the two compounds calculated from published structures [17; 19]. While bond lengths Cu(1)-O(1) and Cu(1)-

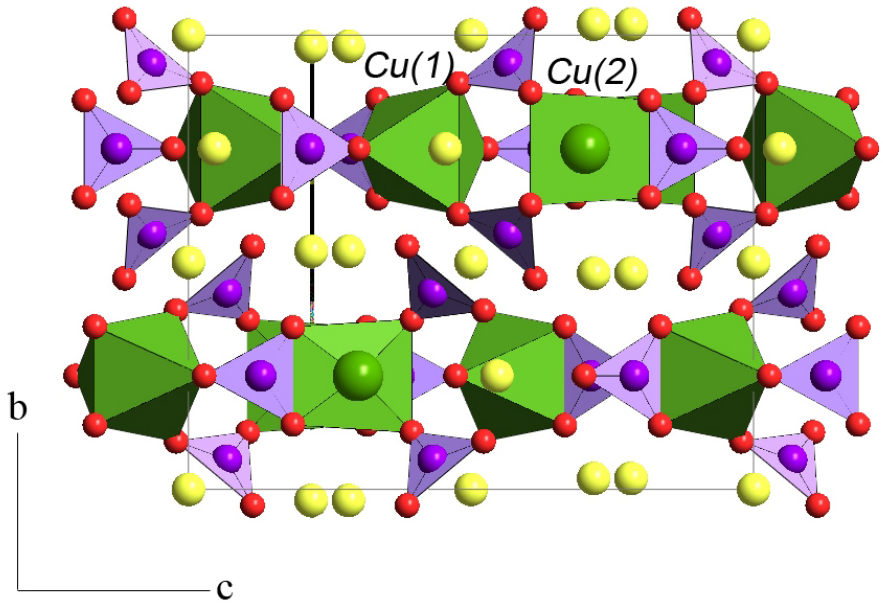

Figure 2.2. Side view of stacked $Cu_2B_4O_{12}$ layers in $Sr_2Cu(BO_3)_2$. The red circles represent O, the green circles Cu and the purple circles B. Dimer units comprise Cu(1) and Cu(2) ions linked via $B(3)O_3$ groups. The yellow spheres are Sr ions separating the layers.

O(2) between the central Copper and apical Oxygen ions increase by $\sim 6\%$ in $Ba_2Cu(BO_3)_2$ over $Sr_2Cu(BO_3)_2$ (table 2.1), the bond lengths to the equatorial Oxygen ions, Cu(1)-O(3) and Cu(1)-O(7) remain the same. As will be shown later, this increased distortion of the Cu(1)-O_6 octahedron leads to a substantial change in relative coupling strengths.

2.1.3 $BaCuSi_2O_6$

$BaCuSi_2O_6$ crystallises at room temperature in a tetragonal body-centred structure (represented by the space group I41/acd with Z = 16), with unit-cell parameters a = 7.042 Å and c = 11.133 Å [20]. Each layer comprises magnetic $Cu^{2+}(3d^9, s = \frac{1}{2})$ ions in square planar CuO_4 units and SiO_4 tetrahedra are arranged in layers parallel to the (001) crystallographic plane (shown in Fig. 2.5). Pairs of layers are staggered in the vertical direction (shown in Fig. 2.6), and within each $Cu_2Si_4O_{12}$ layer the Cu^{2+} ions form a square-lattice of $s = \frac{1}{2}$

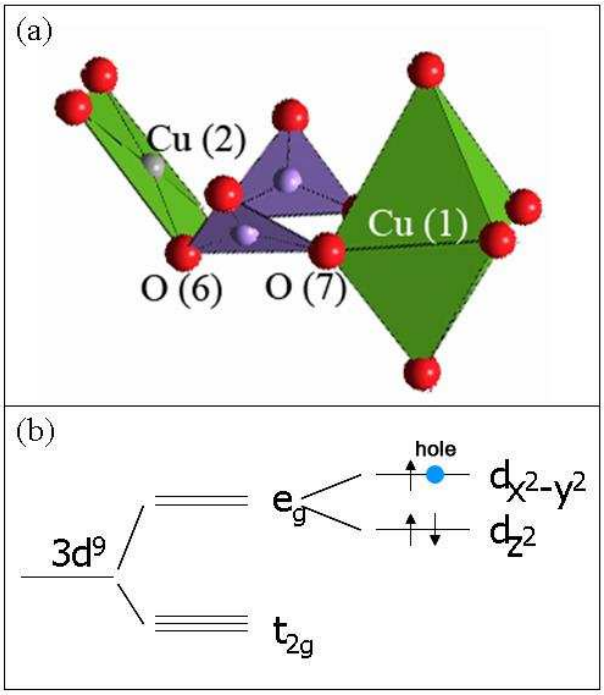

Figure 2.3. (a) A single dimer unit with constituent Cu(1) and Cu(2) ions, from an $Cu_2B_4O_{12}$ layer in $Sr_2Cu(BO_3)_2$. (b) Crystal electric field splitting of $Cu(1)^{2+}$ energy levels in $Cu(1)O_6$ octahedron. Orthorhombic distortion of the octahedron lifts the e_g degeneracy, such that the hole resides in the highest energy level: the antibonding combination of Cu $3d_{x^2-y^2}$ and the equatorial O $2p_\sigma$ orbitals.

Table 2.1. Lattice parameters and Selected Bond lengths (Å) for $Sr_2Cu(BO_3)_2$ and $Ba_2Cu(BO_3)_2$

Lattice parameter(Å)	$Sr_2Cu(BO_3)_2$	$Ba_2Cu(BO_3)_2$	△
$\hat{a}$	7.61	8.02	5.4%
$\hat{b}$	5.43	5.65	4.0%
$\hat{c}$	13.50	13.89	2.9%
Bond Length(Å)			
Cu(1)-O(1)	2.49	2.65	6.4%
Cu(1)-O(2)	2.42	2.56	5.8%
Cu(1)-O(3)	1.99	2.00	0.5%
Cu(1)-O(7)	1.92	1.93	0.5%

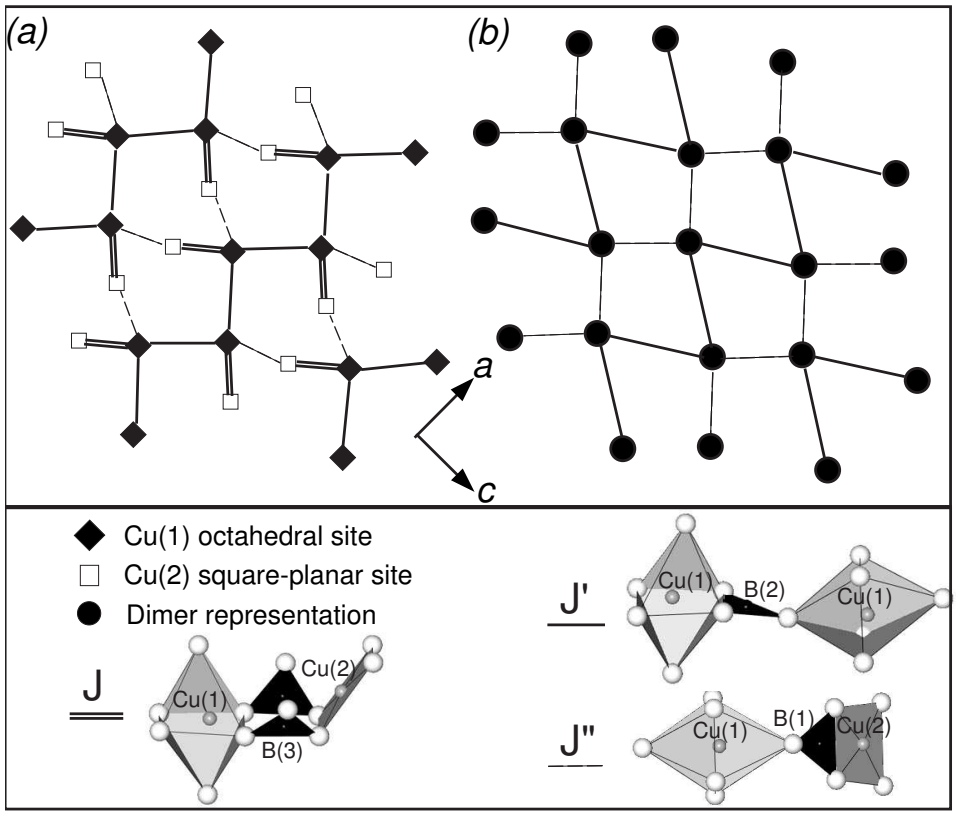

Figure 2.4. (a) Magnetic lattice representing nearest neighbour exchange interactions in $Cu_2B_4O_{12}$ planes in $Sr_2Cu(BO_3)_2$. Atomic positions of Cu(1) and Cu(2) are taken from the real crystal structure. Exchange pathways are labelled in the legend. (b) Equivalent square lattice of dimers, each dimer unit is represented by a solid circle positioned in the geometric center of the Cu(1) and Cu(2) ions.

sites [20].

The shortest Cu-Cu separation, 2.72 Å, is that between sites from complementary planes, which is considerably shorter than the nearest-neighbor in-plane Cu-Cu distance (equal to the lattice constant 7.043 Å, shown in Fig. 2.6). Hence the antiferromagnetic coupling between pairs of Cu^{2+} ions in complementary planes is expected to be much stronger than the in-plane coupling. This has been verified by previous neutron scattering measurements [21], which indicate the dimerisation of vertical pairs of Cu^{2+} ions. Each vertical pair of CuO_4 square

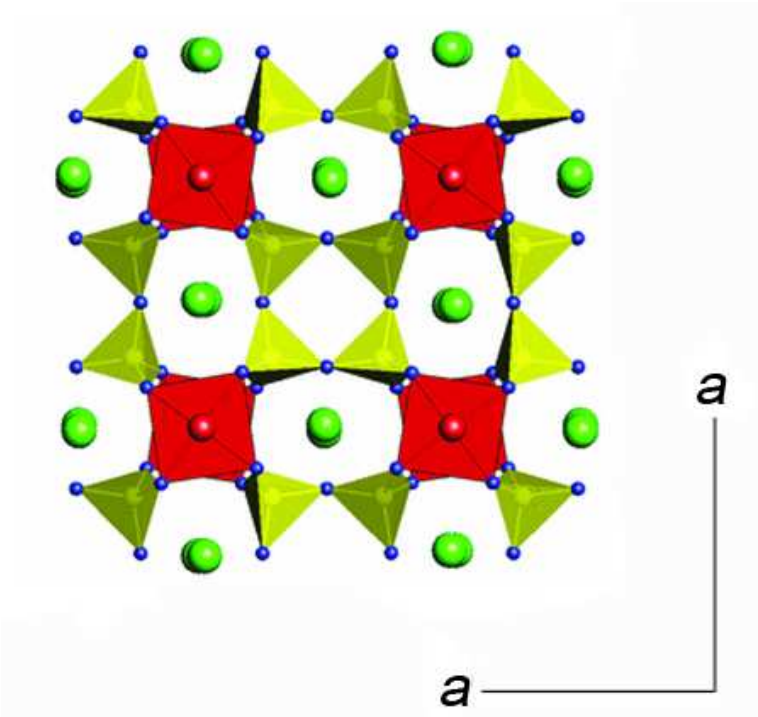

Figure 2.5. $BaCuSi_2O_6$: room temperature structure. Projection of a $Cu_2B_4O_{12}$ layer from $BaCuSi_2O_6$ onto the a-b plane. The green spheres represent Ba ions, the tetrahedra the SiO_4 groups, and the square planar units the CuO_4 groups. Figure from Ref. [20]

planar units on complementary planes (shown in Fig. 2.5), is seen to be twisted (i.e.) each square planar unit does not lie exactly parallel to the neighbouring vertical unit, but is at a small angle. This structural description is valid at room temperature. Above a temperature of 610 K, $BaCuSi_2O_6$ undergoes a structural phase transition to a space group I4/mmm with higher symmetry. The CuO_4 square planar units in complementary planes are parallel to each other in this structure, and the unit-cell volume is reduced by four.

The equivalent magnetic lattice of $BaCuSi_2O_6$ comprises layers of vertical Cu^{2+} dimers arranged in a square lattice (shown in Fig. 2.7), which are staggered in the vertical direction. J represents the strong intra-dimer Heisenberg AF exchange constants, and J' the in-plane coupling between nearest neighbour dimers. There is also an even weaker AF coupling J_f

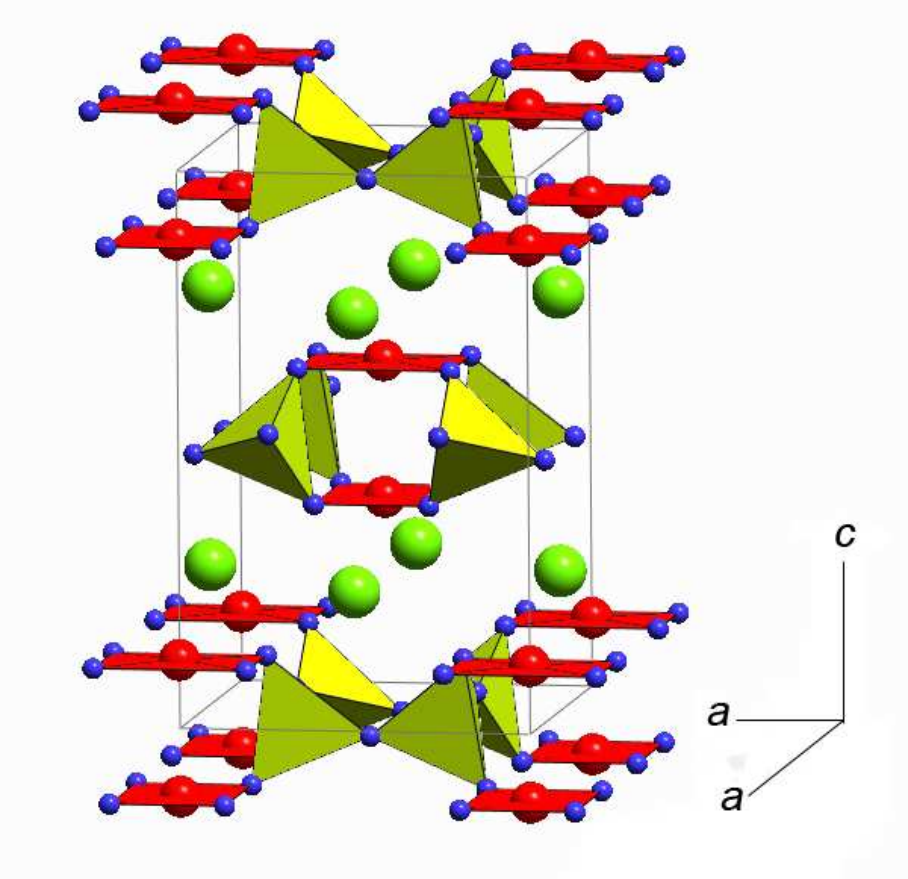

Figure 2.6. $BaCuSi_2O_6$: room temperature structure. Side view of stacked vertically staggered $Cu_2B_4O_{12}$ layers in $BaCuSi_2O_6$. The vertical dimers comprising a pair of Cu^{2+} ions from the square planar CuO_4 groups are linked via SiO_4 tetrahedra.

between dimers on adjacent layers [21].

2.2 Effective spin and bosonic representations of spin dimer systems

This section contains a detailed discussion of a representation which makes clearer the analogy between the family of spin dimer compounds and bosonic systems, and enables a description of the ordered state in magnetic and bosonic language. This representation was introduced in references [22], [4], [23], and [24]. The section ends with a brief derivation of simple scaling

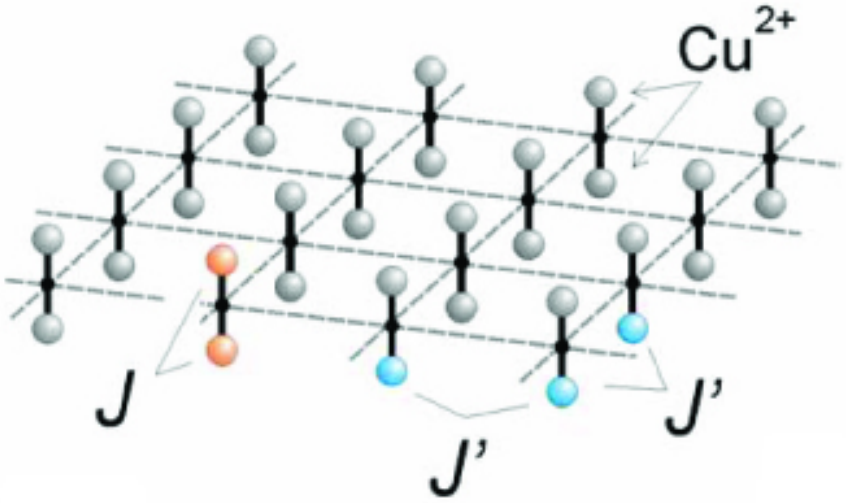

Figure 2.7. Cu^{2+}-dimer plane in $BaCuSi_2O_6$ in a square lattice arrangement. J and J' are the intra-dimer and inter-dimer exchange constants. Figure from Ref. [43].

relations in the vicinity of the quantum critical point in these systems, as a useful tool to analyse experimental results described in later sections.

2.2.1 Microscopic spin Hamiltonian

Each of these families of spin dimer compounds may be represented by the Hamiltonian:

$$\mathcal{H} \;=\; \sum_i \hat{J}\mathbf{s}_{i1}\cdot\mathbf{s}_{i2} + \sum_{(ij)}\sum_{\alpha,\beta}\hat{J}'_{i\alpha,j\beta}\mathbf{s}_{i\alpha}\cdot\mathbf{s}_{j\beta} \;-\; g\mu_B\sum_{i\alpha}Hs^z_{i\alpha} \tag{2.1}$$

Here, $\hat{J} > 0$ is the antiferromagnetic coupling constant that binds a pair of spins, i the index of the dimer and $\mathbf{s}_{i1}$ and $\mathbf{s}_{i2}$ the two spins that form the pair i. H is the applied magnetic field, and g is the g-factor in the direction along which H is applied. The inter-dimer antiferromagnetic coupling is represented by $\hat{J}'_{i\alpha,j\beta}$. While the lattice structure and the magnitude of the coupling constants are specific to each compound, the theory described here that maps spin dimer to

bosonic systems is generic for this class of systems, given that the inter-dimer couplings are much smaller (in magnitude) than $\hat{J}$.

2.2.2 Spin dimer representation

The ground state of each dimer is a singlet (s = 0) and the excited state is a set of three degenerate triplets (s = 1, s^z = 1, 0, -1), such that the ground state of the whole spin lattice is a quantum paramagnet comprising a product of singlets. In the absence of inter-dimer interactions, the triplet excitations are localised (Fig. 2.8a). The effect of inter-dimer coupling is to cause triplet delocalisation, creating a dispersive band of triplets (triplons) (shown in Fig. 2.8b), as we shall see below. In an applied external magnetic field, the degenerate triplet states are split, with a linear decrease in energy of the $s^z = 1$ triplet band as the field increases. Between lower and upper critical magnetic fields H_{c1} and H_{c2}, the lowest $s^z = 1$ triplet excitation band overlaps with the non-magnetic ground state, creating an ordered state. The spin gap Δ of the system is determined by the energy difference between the minimum of the dispersive triplon band and the singlet ground state in zero magnetic field, and is measured by $g\mu_B H_{\mathrm{c1}}$.

Since the ordered state in the vicinity of H_{c1} is the region of interest, we can neglect the unoccupied higher energy $s^z = -1, 0$ triplet states. The remaining two states, the lowest $s^z = 1$ triplet state and the singlet state may be regarded as the up and down states, respectively of an effective $s = \frac{1}{2}$ spin. The original Heisenberg Hamiltonian can be projected on the new singlet-triplet subspace, and new effective spin $\frac{1}{2}$ operators defined.

The effective spin $\frac{1}{2}$ up and down states are the $s^z = 1$ triplet and $s = 0$ singlet state respectively:

$$|\tilde{\downarrow}\rangle = \frac{1}{\sqrt{2}}[|\uparrow\downarrow\rangle - |\downarrow\uparrow\rangle] \qquad |\tilde{\uparrow}\rangle = |\uparrow\uparrow\rangle$$

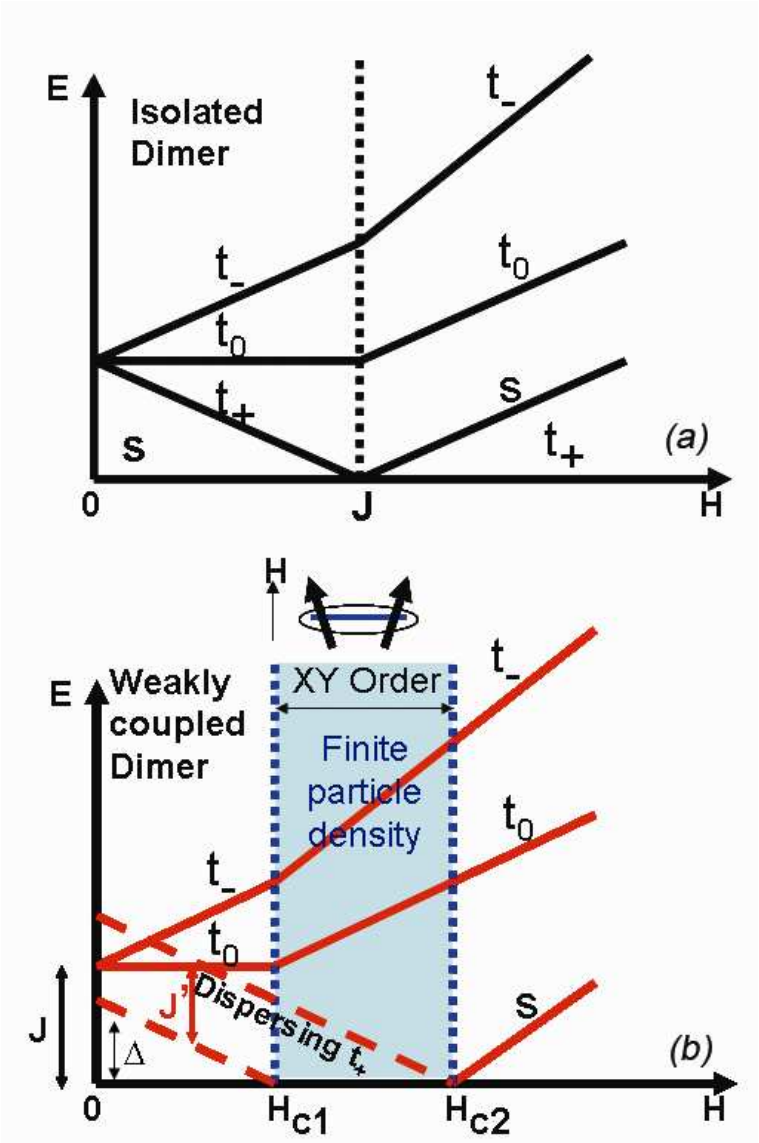

Figure 2.8. Ordering transition in an applied magnetic field. (a) represents the Zeeman splitting of degenerate triplet states in an isolated dimer system (b) represents the Zeeman splitting of triplet bands in a weakly interacting system, leading to an ordered state between H_{c1} and H_{c2}. Figure adapted from Ref. [9].

The effective spin operators are defined as:

$$\begin{aligned} \sigma^z|\tilde{\downarrow}\rangle &= -\frac{1}{2}|\tilde{\downarrow}\rangle \qquad \sigma^z|\tilde{\uparrow}\rangle = +\frac{1}{2}|\tilde{\uparrow}\rangle \\ \sigma^+|\tilde{\downarrow}\rangle &= |\tilde{\uparrow}\rangle \qquad \sigma^+|\tilde{\uparrow}\rangle = 0 \\ \sigma^-|\tilde{\downarrow}\rangle &= 0 \qquad \sigma^-|\tilde{\uparrow}\rangle = |\tilde{\downarrow}\rangle \end{aligned}$$

The original spin $s = \frac{1}{2}$ operators can be expressed in terms of the new effective spin $\frac{1}{2}$ operators by the following transformation:

$$s^+_{1,2} = \mp\frac{1}{\sqrt{2}}\sigma^- \qquad s^-_{1,2} = \mp\frac{1}{\sqrt{2}}\sigma^- \qquad s^z_{1,2} = \frac{1}{2}[\sigma^z + \frac{1}{2}] \tag{2.2}$$

When expressed in term of the effective spin operators, up to first order in perturbation theory, the original Hamiltonian becomes

$$\mathcal{H} = \sum_{(ij)} \frac{\tilde{J}_{ij}}{2}\left(\sigma_i^-\sigma_j^+ + \sigma_i^+\sigma_j^- + \frac{1}{2}\sigma_i^z\sigma_j^z\right) - g\mu_B\sum_i \tilde{H}\sigma_i^z + C, \tag{2.3}$$

or

$$\mathcal{H} = \sum_{(ij)} \tilde{J}_{ij}\left(\sigma_i^x\sigma_j^x + \sigma_i^y\sigma_j^y + \frac{1}{2}\sigma_i^z\sigma_j^z\right) - g\mu_B\sum_i \tilde{H}\sigma_i^z + C, \tag{2.4}$$

where $\tilde{J}_{ij}$ is a linear combination of inter-dimer couplings $\hat{J}'_{i\alpha,j\beta}$. The system is in an effective magnetic field $g\mu_B\tilde{H} = g\mu_B H - J - \frac{\tilde{J}_{ij}}{2}$, and C is a simple energy shift. We assume here that the effective Hamiltonian is translationally invariant and nonfrustrated as appears to be the case for the compounds under study. Eqn. 2.4 represents a uniform $s = \frac{1}{2}$ XXZ model in three dimensions with a spatial anisotropy and an easy-plane spin anisotropy. It is useful to note that the Hamiltonian in Eqs. 2.3 and 2.4 is symmetric with respect to reversal of the magnetisation. (i.e. $\mathcal{H}(\sigma_z) = \mathcal{H}(\sigma_{-z})$) This implies that the system is symmetric about a field $H = H_{\text{symm}}$ at which $\tilde{H} = 0$, where $g\mu_B H_{\text{symm}}$ is given by $J + \frac{\tilde{J}_{ij}}{2}$.

2.2.3 Representative lattice

As an example of a representative lattice, we briefly consider a structure comprising coupled square layers of dimers coupled in the vertical direction (Fig. 2.9) (the lattices of the families of compounds studied in this work can be simplified to this representation) with $J_{||}$ intra-layer coupling on a square side and $J_{\perp}$ inter-layer coupling. This representative lattice is described by the Hamiltonian

$$\begin{aligned}\mathcal{H} &= \sum_{(i\alpha)} \frac{J_{||}}{2}\left(\sigma_i^- \sigma_{i+\hat{e}_\alpha}^+ + \sigma_i^+ \sigma_{\mathbf{i}+\hat{e}_\alpha}^- + \frac{1}{2}\sigma_i^z \sigma_{\mathbf{i}+\hat{e}_\alpha}^z\right) \\ &+ \sum_i \frac{J_{\perp}}{2}\left(\sigma_i^- \sigma_{i+\hat{z}}^+ + \sigma_i^+ \sigma_{i+\hat{z}}^- + \frac{1}{2}\sigma_i^z \sigma_{i+\hat{z}}^z\right) \\ &- \sum_i \left(g\mu_B H - (J + \frac{J_{||}}{2} + \frac{J_{\perp}}{4})\right)\ \sigma_i^z + C, \end{aligned} \tag{2.5}$$

from which we obtain $g\mu_B H_{\text{symm}} = J + \frac{J_{||}}{2} + \frac{J_{\perp}}{4}$

The difference in coordination number of each dimer in the vertical and horizontal directions is accounted for by the number of neighbouring sites being summed in the representation of the Hamiltonian in Eqn. 2.5, and may differ for each specific lattice.

2.2.4 Triplet dispersion

From Eqn. 2.3, it can be seen how the inter-dimer interactions $\tilde{J}_{ij}$ lead to triplet dispersion. While the inter-dimer interactions acting on a direct product of singlets have no effect up to much higher orders of perturbation, the effect of the inter-dimer interaction on nearest neighbour singlets and triplets is to flip spins on each, thereby causing the singlet and triplet to switch positions. This is equivalent to triplet hopping, which leads to gapped delocalised triplet excitations (triplons) with single particle dispersion relation $e(\mathbf{k}) = \tilde{J}_{ij}(\cos k_x + \cos k_y)$ (the

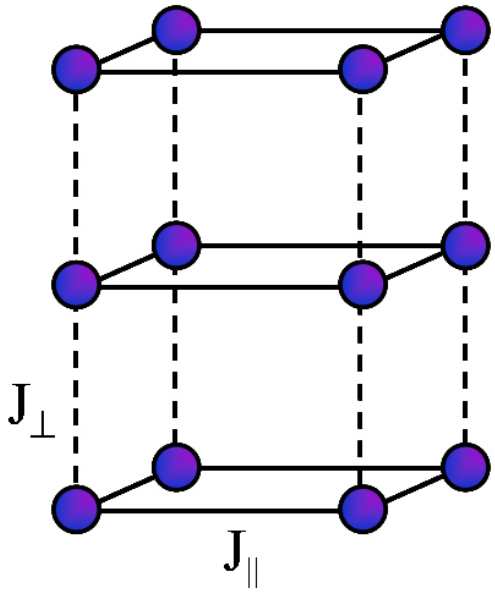

Figure 2.9. Representative magnetic lattice comprising coupled layers of square dimers. The spheres represent dimers, and $J_{||}$ and $J_{\perp}$ are the intra-layer and inter-layer exchange constants between dimers.

tight binding calculation is shown in Appendix C, we shall see in the next section that the potential V in Appendix C is equivalent to $\frac{\tilde{J}_{ij}}{2}$), such that the smallest excitation gap occurs at $\mathbf{q} = (\pi, \pi)$ in zero magnetic field (shown in Fig. 2.10).

Eqn. 2.3-2.5 also reflects the effect of a magnetic field, which is to lower the energy of the triplet band in linear fashion. The spin gap Δ between the singlet level and the lowest energy s^z = 1 triplet band is closed at a critical magnetic field $H_{\rm c1} = \frac{\Delta}{g\mu_B}$. The magnetic field can be considered as a chemical potential (μ) which is prohibitively large below $H_{\rm c1}$ thereby preventing triplet population, but crosses a critical value at $H_{\rm c1}$, giving rise to a precisely field-tunable concentration (or density) $\rho = M \equiv \langle s^z \rangle$ of triplons between critical magnetic fields $H_{\rm c1}$ and $H_{\rm c2}$, at which the magnetisation saturates. The system is an ordered XY antiferromagnet in this region.

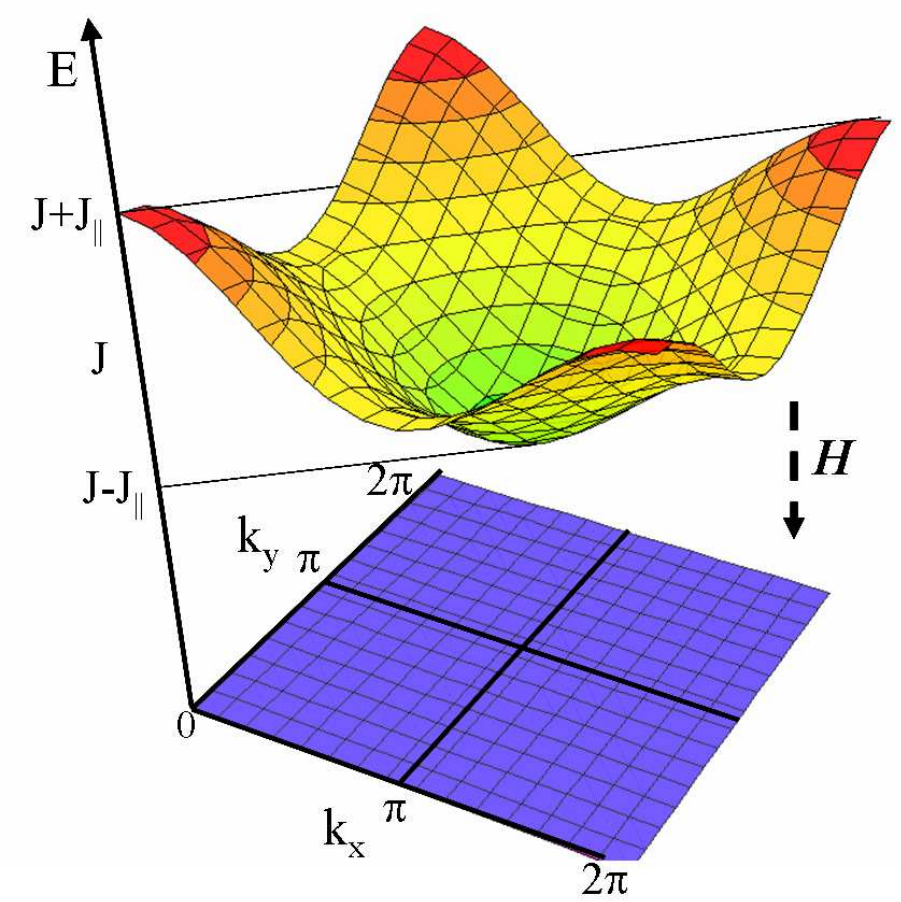

Figure 2.10. Dispersing s_z = 1 triplon band with exchange couplings from the representative lattice in Fig. 2.9. The shape of the dispersion is the same in any magnetic field $H \leq H_{c1}$, but the gap to the singlet state decreases with increasing H. At $H = H_{c1}$, the gap to the singlet state is closed at wavevector $k_x = k_y = \pi$, resulting in finite triplet population

2.2.5 Correspondence with bosonic system

Finally, we draw the correspondence between the magnetic system and a bosonic system. The system can be considered as a Bose gas of interacting particles by neglecting the unoccupied higher energy $s^z = -1, 0$ triplet bands (since $\hat{J}'_{i\alpha,j\beta} \ll J$), and replacing each dimer by an effective site that can be either empty (singlet state) or occupied by a hardcore boson ($s^z = 1$

triplet state):

$$|\tilde{\downarrow}_{\mathbf{i}}\rangle \rightarrow |0\rangle_{\mathbf{i}} \qquad |\tilde{\uparrow}_{\mathbf{i}}\rangle \rightarrow b^{\dagger}_{\mathbf{i}}|0\rangle_{\mathbf{i}} \tag{2.6}$$

where $|0\rangle_{\mathbf{i}}$ represents the empty state at the site $\mathbf{i}$.

The spin operators are transformed to hardcore boson operators as:

$$\sigma^{+}_{i} \;=\; b^{\dagger}_{i} \qquad \sigma^{-}_{i} \;=\; b_{i} \qquad \sigma^{z}_{i} \;=\; \hat{n}_{i} \;-\; \frac{1}{2} \tag{2.7}$$

with the constraint

$$\hat{n}_{i} \equiv b^{\dagger}_{i} b_{i} \;=\; 0, 1. \tag{2.8}$$

In this language, the effective low energy Hamiltonian is:

$$\mathcal{H} \quad = \quad \sum_{(ij)} t_{ij} \left(b^{\dagger}_{i} b_{j} + b^{\dagger}_{j} b_{i} \right) + \sum_{(ij)} V_{ij} \hat{n}_{i} \hat{n}_{j} + \mu \sum_{i} \hat{n}_{i}, \tag{2.9}$$

with new parameters t_{ij}, V_{ij} and μ corresponding to the old ones as $t_{ij} \;\sim\; V_{ij} \;\sim\; \dfrac{\tilde{J}_{ij}}{2}$ and $\mu \sim J \;-\; H$. The kinetic energy t of the interacting bosons is provided by the XY-component of the inter-dimer Heisenberg interaction, while the short range repulsion V between them arises from the Ising or Z-component.

The effective Hamiltonian for the representative lattice shown in Fig. 2.9 is:

$$\begin{aligned} \mathcal{H} \quad &= \quad t \sum_{\mathbf{i},\alpha} (b^{\dagger}_{\mathbf{i}+\hat{e}_{\alpha}} b_{\mathbf{i}} + b^{\dagger}_{\mathbf{i}} b_{\mathbf{i}+\hat{e}_{\alpha}}) + t' \sum_{\mathbf{i}} (b^{\dagger}_{\mathbf{i}+\hat{z}} b_{\mathbf{i}} + b^{\dagger}_{\mathbf{i}} b_{\mathbf{i}+\hat{z}}) \\ &+ \quad V \sum_{\mathbf{i},\alpha} n_{\mathbf{i}} n_{\mathbf{i}+\hat{e}_{\alpha}} + V' \sum_{\mathbf{i}} n_{\mathbf{i}} n_{\mathbf{i}+\hat{z}} + \mu \sum_{\mathbf{i}} n_{\mathbf{i}} \end{aligned} \tag{2.10}$$

where the chemical potential is $\mu \;=\; J \;-\; g\mu_{B}H$, $t \;=\; V \;=\; \dfrac{J_{\|}}{4}$, and $t' \;=\; V' \;=\; \dfrac{J_{\perp}}{4}$.

The critical magnetic field H_{c1} corresponds to a critical value of chemical potential at which a finite number of bosons are populated, the particle number increasing with magnetic

field in approximately linear fashion until the entire lattice is populated at H_{c2} (where the magnetisation saturates.) The expressions for H_{c1} and H_{c2} are derived in the next section. The ordered state between H_{c1} and H_{c2} is determined by the balance between the kinetic energy and the repulsive interactions. In the case under consideration, the kinetic energy dominates (since $2t > V$ always), resulting in a BEC ground state.

2.2.6 Dependence of H_{c1}, H_{c2} on inter-dimer coupling constants

Since H_{c1} corresponds to the chemical potential at which the population of bosons becomes finite, in that limit the repulsion term is irrelevant because the density of bosons vanishes. In the representative case of vertically coupled square layers of dimers (shown in Fig. 2.9), the chemical potential corresponding to H_{c1} is given by $\mu = 4t + 2t'$ (i.e. the chemical potential must be lowered until it equals the mimimum of the single particle dispersion in order for particles to be populated.) For this representative lattice, we obtain the result:

$$g\mu_B H_{c1} = J - J_{||} - \frac{J_\perp}{2} \tag{2.11}$$

To estimate H_{c2}, the repulsion term cannot be neglected. Taking into account the particle-hole symmetry of the Hamiltonian of Eqn. 2.9, we can perform a particle-hole transformation on this Hamiltonian: $b_i^\dagger \rightarrow d_i$. Up to a constant, the new Hamiltonian reads

$$\mathcal{H}_{\text{hole}} = t\sum_{(ij)}\left(d_i^\dagger d_j + d_j^\dagger d_i\right) + V\sum_{(ij)}\hat{n}_i^d\hat{n}_j^d - \mu_h\sum_i \hat{n}_i^d, \tag{2.12}$$

In terms of holes, H_{c2} corresponds to the chemical potential where the number of holes becomes finite, and one can again neglect the repulsion term. This is not, however equivalent to neglecting the repulsion in Eqn. (2.9) since V appears in the expression of μ_h. In the represen-

tative case of vertically coupled square layers of dimers, $\mu_h = -\mu - 4V - 2V'$, and holes begin to populate at $\mu_h = 4t + 2t'$ which leads to the result $g\mu_B H_{\rm c2} = J + 2J_{||} + J_{\perp}$.

Equivalently, $H_{\rm c2}$ can be obtained by exploiting the symmetry of the Hamiltonian in Eqn. 2.5, for which $H_{\rm c1}$ and $H_{\rm c2}$ are symmetric about $g\mu_B H_{\rm symm} = J + \frac{J_{||}}{2} + \frac{J_{\perp}}{4}$, which leads to the same result.

2.2.7 Ordered state in bosonic and spin representation

The BEC ordered state is equivalent to an XY antiferromagnet in terms of the original spin degrees of freedom. The bosons that form the condensate are represented by a coherent superposition between a singlet and the lowest s^z = 1 triplet states: $u \cdot e^{i\phi}|\tilde{\uparrow}\rangle + v \cdot |\tilde{\downarrow}\rangle$ (where $u^2 + v^2 = 1$) as shown in Fig. 2.11. The spins on each dimer are at an in-plane angle of 180° with respect to each other, and are canted by an angle $\tan^{-1}\frac{u}{\sqrt{2}v}$ above the XY plane (shown in Appendix A). The angle ϕ represents the orientation of the entire XY-plane of spins, which is free to rotate uniformly about the Z-axis. The order parameter of the BEC is the boson creation operator $b^\dagger$, which corresponds to the in-plane staggered magnetisation (perpendicular to the magnetic field) $M_x + iM_y$ of the XY- or canted antiferromagnet. The phase of the Bose condensate is simply the orientation of the spins in the XY plane (ϕ) and the density of bosons is proportional to the uniform magnetisation M (in the direction of the applied magnetic field.)

2.2.8 Low energy effective theory

Precisely at the QCP separating the disordered from the ordered state, low momenta excitations can carry arbitrarily low energy, and these therefore dominate the low temperature properties. It is useful to describe the system by a universal continuum quantum field theory that describes the critical properties in its vicinity. The continuum Boson field (representing the local order

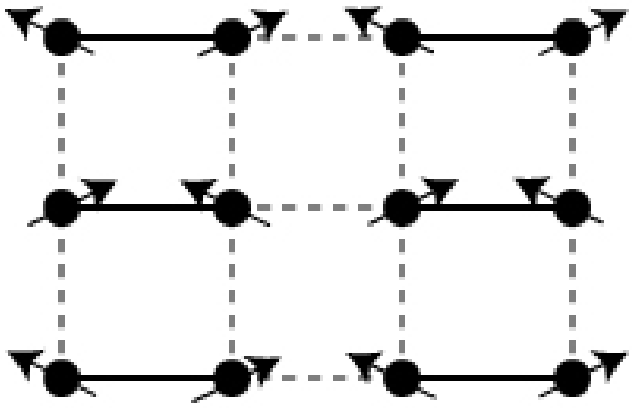

Figure 2.11. XY antiferromagnetic order represented by canted spins (i.e. a superposition of singlet and triplet states). The magnetic field is oriented out of the page, and the static moments in the canted phase can rotate uniformly about the the out-of-page axis [10].

parameter) is defined as:

$$\psi^*(x,\tau) \text{ which is associated with } \frac{1}{\sqrt{a}} b^\dagger \tag{2.13}$$

(i.e. $\langle \psi^* \rangle \neq 0$ in the ordered BEC phase). We can obtain this critical theory by expressing the Hamiltonian Eqn. 2.9 in terms of ψ, expanding in spatial and time gradients, and taking the limit of the lattice parameter $\rightarrow 0$ at fixed ψ. We thus obtain the continuum field theory representing a dilute Bose gas in the grand canonical ensemble at a chemical potential μ, with a repulsive short-range interaction characterized by the action

$$S = \int \mathrm{d}^d \mathbf{x} \int \mathrm{d}\tau \left(\psi^* \frac{\partial \psi}{\partial \tau} + |\nabla \psi|^2 - \mu |\psi|^2 + u |\psi|^4 \right). \tag{2.14}$$

Here, $\mu \propto (H_{c1} - H)$, and we have retained only leading order temporal and spatial gradients and the leading dependence of u. For $\mu > 0$ we have a finite density of ψ^* bosons which Bose

condense in the ground state, so that $\langle \psi^* \rangle \neq 0$.

From a simple dimensional analysis of the action, the effect of the scale transformation up to the scale b yields the following relations [25]:

$$\beta \to \tilde{\beta} \equiv \beta b^{-2},\ L \to \tilde{L} \equiv L b^{-1},\ \psi \to \tilde{\psi} \equiv \psi b^{\frac{d}{2}},$$
$$\mu \to \tilde{\mu} \equiv \mu b^2,\ u \to \tilde{u} \equiv u b^{2-d},$$

where L is the system size.

We see that the dynamical critical exponent $z = \dfrac{[\beta]}{[L]}$ is 2. The physical origin of $z = 2$ in this case is the quadratic dispersion relation of the lowest triplet (bosonic) excitation when the energy gap of the disordered phase goes to zero at the QCP, since the Zeeman (or chemical potential) term commutes with the rest of the Hamiltonian. The upper critical dimension d_c is determined by the scaling dimension of the quartic coupling u, which tells us up to what dimension the free-field fixed point is stable (i.e. a mean field theory will be exact) and is in this case equal to 2.

Since $d_c = 2$, a meanfield scaling analysis is valid for $d \geq 2$, and can be used to obtain universal power law behaviour for measurable quantities in close proximity to the QCP:

$$T_{\mathrm{c}} \propto (H - H_{\mathrm{c1}})^{2/d}, \quad \rho(T = 0) \equiv M(T = 0) \propto (H - H_{\mathrm{c1}}), \quad M(H_{\mathrm{c1}}) \propto T^{d/2}. \tag{2.15}$$

where T_{c} is the ordering temperature, H_{c1} is the critical magnetic field, ρ is the particle density, and M is the uniform magnetisation.

Chapter 3

Single crystal synthesis and characterisation

"We are men of groans and howls, Mystic men who eat boiled owls,

Tell us what you wish, oh king, Our magic can do anything"

-'Bartholomew and the Oobleck' by Dr. Seuss

Clean single crystals are essential to perform high precision measurements of new materials. This chapter details growth techniques and structural characterisation methods used for the single crystals on which experiments have been performed as part of this dissertation.

3.1 Single crystal growth

Single crystals are particularly important for measurements near the QCP which require clean materials with a low disorder and anisotropic characterisation. Polycrystalline material consists of small randomly oriented grains; boundaries between these grains often comprise a different phase, and hence a large source of impurities. Further, anisotropic properties, which are often important to study in new materials, are averaged out in polycrystalline samples. Single crystals

are also likely to be significantly less disordered than polycrystalline samples, since the grains are large, and not strained during crystal growth by numerous densely packed neighbouring grains. This is particularly important in measurements near the QCP, where small quantities of disorder can profoundly affect ordering over large length scales. Single crystals can vary widely in quality, and careful characterisation is important to detect flaws such as impurity inclusions, grain boundaries, residual flux, and misoriented crystallites.

3.1.1 Equilibrium phase diagram

The principle behind different crystal growth techniques is sketched out by means of a prototypical phase diagram. The example shown in Fig. 3.1 is the binary phase diagram for the intermetallic system Ce-Sb [26]. All phases that may form between Ce and Sb at various temperatures are represented. The 'liquidus' temperature (represented by the curved line) is the temperature above which no crystals exist. It is the locus of temperatures at which crystals first begin to appear on cooling the melt under equilibrium conditions. The horizontal 'peritectic' lines connect conjugate phases in equilibrium. A vertical line drawn on the phase diagram (such as the one labelled S in Fig. 3.1) represents a constant composition, and is referred to as an 'isopleth'.

Tracing the isopleth S through a cooling process, the starting melt M comprises a starting composition 80% Sb : 20% Ce heated to 1900° C. On cooling M, at the temperature T corresponding to the intersection of the isopleth with the liquidus line, crystals of $CeSb_2$ begin to precipitate from the melt. As cooling continues, at a given temperature, say X, there are two phases in equilibrium: $CeSb_2$, and liquid of composition Y_1. The ratio of $CeSb_2$ to liquid is given by XY_2 / XY_1.

These simple principles of chemical equilibrium form the basis of all crystal growth methods. Compounds can be classified into two types according to their behaviour during melting.

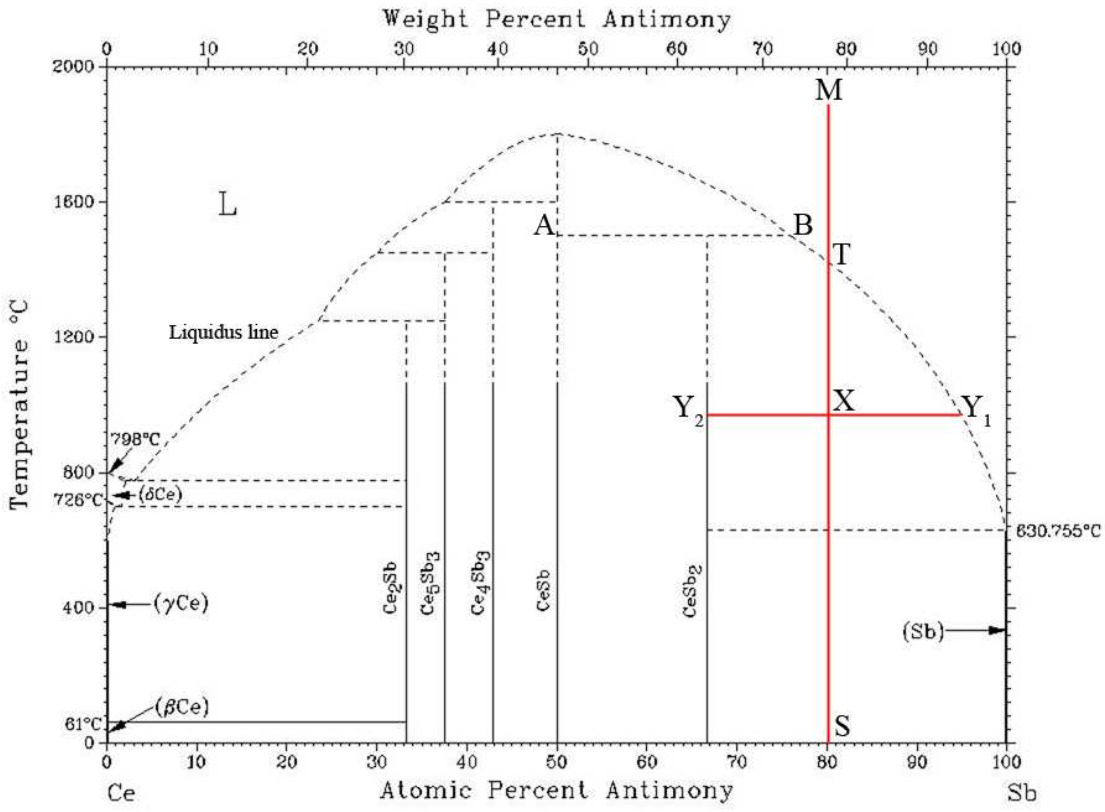

Figure 3.1. Phase diagram of binary system Ce-Sb. Figure from Ref. [26]

For instance, the compound CeSb (isopleth at 50% Ce: 50% Sb) melts directly to a liquid of chemical composition identical to that of the crystalline compound. Conversely, on cooling liquid of the same composition, it recrystallises into the compound CeSb. Compounds of this nature are called congruently melting compounds. A compound such as $CeSb_2$ (isopleth at 66.7 % Sb : 33.3 % Ce) on the other hand, does not melt to a liquid of the same composition, but decomposes to a different liquid (of composition B) and the crystalline phase CeSb at the peritectic temperature. Along the peritectic line AB, three phases are in equilibrium as shown by the reaction at 1480° C:

$$CeSb_2 \leftrightarrows CeSb + melt \tag{3.1}$$

3.1.2 Terracotta warriors

At this juncture, a digression regarding the historical synthesis [27] of one of these compounds $BaCuSi_2O_6$ may be of interest. The earliest occurrence of $BaCuSi_2O_6$ (termed *Han Purple*) was as far back as 480 BC when it was used as a pigment on the Terracotta warriors from the Han dynasty (Fig. 3.2). This was an extremely unusual archeological find, one of the reasons being that blue pigments were rarely found in such early civilisations, naturally occurring organic or mineral sources for stable blue dyes being exceptionally hard to come by. They could only be mined from deposits that were difficult to access. The pigment used on the Terracotta warriors were man-made (since $BaCuSi_2O_6$ does not occur in nature), and required high technical expertise, with temperatures higher than 1000° required for long periods of time during synthesis.

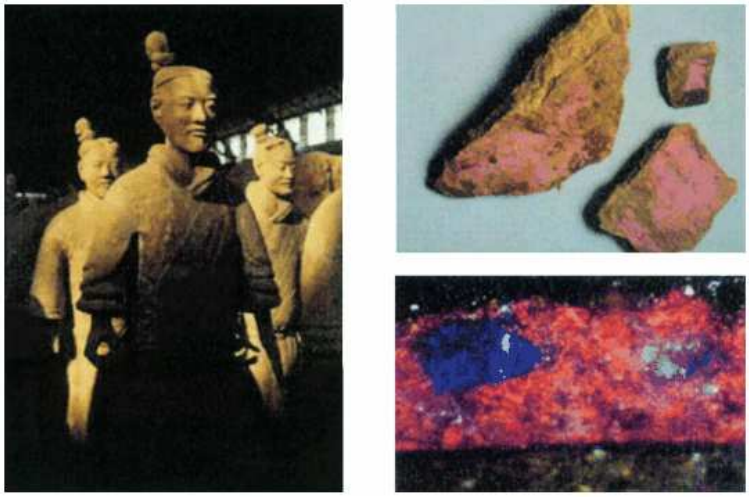

Figure 3.2. Sample of the Terracotta Army Xi'an, China. Left: a group of terracotta soldiers. Top right: fragments of the purple trousers of a soldier. Bottom right: A microscopic view (enlargement 500 times) of a cross section of its pigment layer. The displayed part has a horizontal extension of 0.22 mm. The pigment layer contains grains of Han Purple and Cinnabar. Under the pigment layer there is a dark lacquer and under that the terracotta. Figure from Ref. [27].

The greatest problem for the production of this purple pigment, however was the barium

source. A possible raw material is witherite ($BaCO_3$), which would lead to products of satisfactory quality, but witherite is very rare and was not readily available in ancient China. Nevertheless some samples indicate its use. If Baryte ($BaSO_4$) is used in a mixture with quartz and copper minerals, only small amounts of blue or purple barium-copper silicates form. Chinese chemists, however found an innovative method to circumvent these problems: they added lead salts (lead carbonate or lead oxide) that catalyse a dismutase reaction leading to the in situ decomposition of $BaSO_4$. Since $PbSO_4$ decomposes at 1000° C (much lower than the 1560° C needed for $BaSO_4$), it is reasonable to assume that the PbO formed acts as a flux, while BaO is removed from the equilibrium as *Han Purple* is formed.

Interestingly, this is exactly the same principle we use now, 2500 years later to perform a flux growth! PbO was the Chinese chemists' version of a flux used to reduce the temperature of the high temperature solute. In order to grow single crystals of $BaCuSi_2O_6$ in the laboratory, we borrowed from the ancient Chinese chemists and used PbO as one of different fluxes which we experimented with to try and grow $BaCuSi_2O_6$ out of a high temperature solution.

3.1.3 Polycrystalline precursor

The first step in the growth process used for the families of compounds discussed in this dissertation is the synthesis of polycrystalline material. The polycrystalline precursor was prepared by a solid state reaction of constituent materials ground together in stoichiometric ratios and heated in flowing O_2. In the case of $Sr_2Cu(BO_3)_2$, the starting materials are $SrCO_3$, CuO and B_2O_3 [17]. These materials are ground together in a centrifugal ball-mill in order to reduce the particle size and promote reactivity, and then pressed into pellets in a steel die under high pressures. For this purpose, custom-made tungsten carbide pellets were found to perform better than commercial steel pellets in the die, since steel pellets are softer and more prone to being scratched by pressing hard powders. The pellets are then placed in a Lindberg tube furnace

through which flowing O_2 is passed, and heated in temperatures progressively increasing from 900° C to 950° C for approximately 100 hours with intermediate grindings. While higher temperatures are better for faster reaction rates and denser final products, these can only be reached progressively, since the unreacted starting materials have a lower melting point, and need to be at least partially reacted (to form the final product with a higher melting point), before sinters at higher temperatures can be performed. To prepare $Ba_2Cu(BO_3)_2$, the starting materials are $BaNO_3$, CuO and B_2O_3. The reaction is performed between 600° C to 1000° C for approximately 100 hours with intermediate grindings. $BaCuSi_2O_6$ requires considerably more reaction time, due to the formation of impurity phases during intermediate stages of the polycrystalline growth process. $BaCuSi_4O_{10}$ in particular (a blue compound) is stable up to $\sim 900^\circ$ C, and the reaction must be performed at higher temperatures for significantly long periods for the bulk of material to form $BaCuSi_2O_6$. The reaction is performed between 900° C and 1050° C for approximately 300 hours with intermediate grindings.

3.2 Flux growth

One of the methods used to grow single crystals is the flux growth technique. This is typically used to grow incongruently melting compounds. A flux refers to a material used in addition to the stoichiometric ratio of constituent elements of the required compound. A flux can either be an excess of one of the constituent elements (self flux) or an entirely different material which is soluble in the melt. The flux growth technique is a spontaneous nucleation technique where the starting materials are heated to high temperatures to form the melt. As the melt is slowly cooled, single crystals of the target material are precipitated out of the solution, and form from multiple nucleation sites.

From the description of congruently melting and incongruently melting compounds in the previous section, it is clear that in order to form an incongruently melting compound, a flux is

essential. To grow crystals of an incongruently melting compound, such as $CeSb_2$ for example, it is necessary to start with a non-stoichometric composition - a possible starting composition may be S (80 % Sb : 20 % Ce). In this case, the flux is a self flux: Sb. On cooling from the melt above the liquidus, crystals of $CeSb_2$ are precipitated in equilibrium with the melt in the temperature range 1400° C down to the solidus line at 630.7° C. The chosen starting composition and temperature range of the reaction is determined by factors such as controlled number of nucleation sites, physical space for single crystal growth in the melt, and reduced melting temperature. Another essential requirement for single crystals to grow in equilibrium with a liquid is an exposed liquidus, such as the curve along which Y_2 lies in the Ce-Sb phase diagram. Once the grown crystals are in equilibrium with the solution, the remaining liquid is decanted, and the crystals allowed to cool rapidly in air. More details about the flux growth technique can be found in Ref. [28].

3.2.1 Flux grown single crystals

All three materials: $Sr_2Cu(BO_3)_2$, $Ba_2Cu(BO_3)_2$ and $BaCuSi_2O_6$ were grown for the first time by the flux technique using as starting materials the polycrystalline precursor, and $LiBO_2$ as a flux. Since the equilibrium phase diagram is not known for these mixtures of compounds, the flux growth recipe was chosen and refined empirically.

The growth recipe for both $Sr_2Cu(BO_3)_2$ and $Ba_2Cu(BO_3)_2$ was similar, with a starting molar ratio of 1 : 1.4 polycrystalline material to $LiBO_2$. The crucibles used for the growth were made of platinum. The mixture in the crucible was heated in a box furnace to 925° C, cooled at approximately 1° C per hr to 860° C and the remaining liquid decanted using a centrifuge technique. Crystals of $Sr_2Cu(BO_3)_2$ grown by this technique are multi-faceted, purple, and up to 5 mm on a side, whereas the $Ba_2Cu(BO_3)_2$ crystals are rod-shaped (shown in Fig. 3.4). It was later found that for the purpose of pulsed magnetic field experiments in particular, crystals

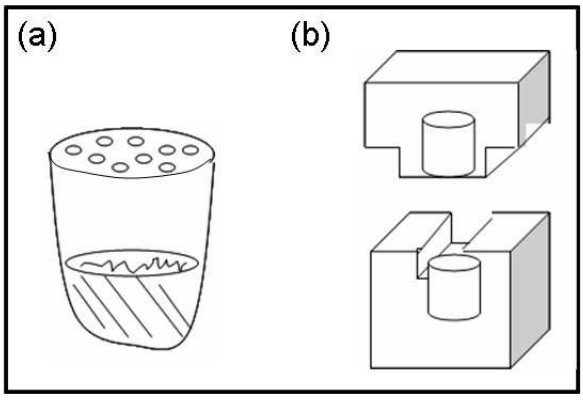

Figure 3.3. (a) Pt crucible and strainer used for the flux growth (b) Alumina brick used as enclosure for the Pt crucible inside the furnace to provide an isothermal environment, and to physically contain the crucible during the decanting process.

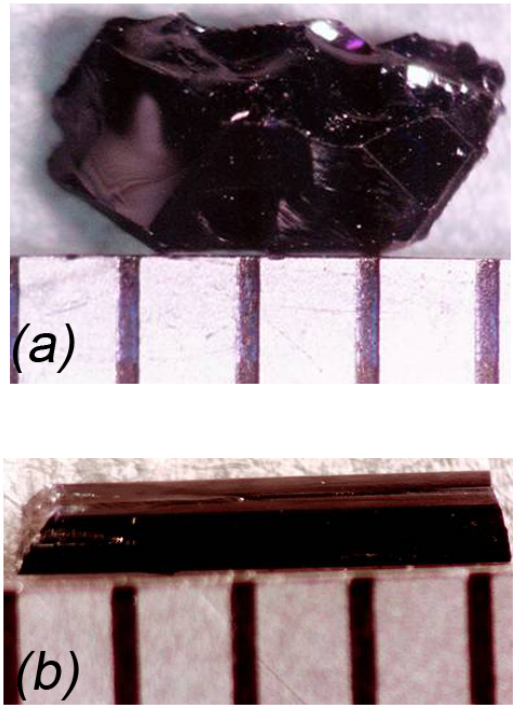

Figure 3.4. Typical single crystals of (a) $Sr_2Cu(BO_3)_2$ and (b) $Ba_2Cu(BO_3)_2$ grown using the flux growth technique (shown on a mm scale).

needed to be oriented and shaped into cylindrical pieces to precisely fit inside the detection coils and thereby maximise the filling factor. For this purpose, crystals grown by the flux-growth technique were too small, and the image furnace technique was used instead (described in the next section.)

$BaCuSi_2O_6$ was grown using $LiBO_2$ as a flux, with a starting molar ratio of 2 : 1 polycrystalline material to flux. The mixture was heated in a Pt crucible to 1100° C, cooled at approximately 1° C per hr to 875° C and the remaining liquid decanted. Single crystals of $BaCuSi_2O_6$ grown by this technique are plate-like with the $c-$axis oriented perpendicular to the plane of the plate, purple in color, with dimensions of up to 3 cm on a side and 1 mm thickness (shown in Fig. 3.5). These crystals were found to be superior to image-furnace grown crystals, which have the disadvantage of significant impurity phase inclusions and greater disorder, leading to a smearing out of the Schottky anomaly associated with the magnetic dimers, and broad NMR lines [29].

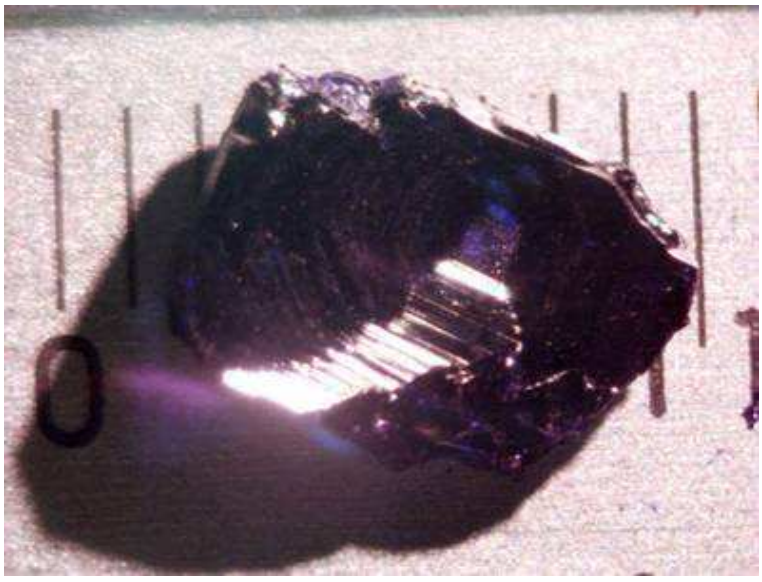

Figure 3.5. Typical single crystal of $BaCuSi_2O_6$ grown using the flux growth technique (shown on a mm scale).

3.3 Image furnace growth

Growth in an image furnace is by a technique known as the 'Travelling-Solvent Floating-Zone' growth process, involving single crystal nucleation at one nucleation site, instead of spontaneous nucleation at multiple sites.

The starting material for this technique is the polycrystalline precursor, as for the flux growth technique. In this case, however, the polycrystalline material needs to be shaped into dense, uniform rods which serve as a starting point for nucleation of a single crystal. After the sintering process described in the previous section is complete, the pellet of polycrystalline material is ground into fine powder in a centrifugal ball mill, and shaped into a rod about 10 cm in length and 0.5 mm in diameter by packing it into a rubber tube. Conventionally, latex tubes are used to pack the polycrystalline material, but it was found during the course of my research that party balloons are a better alternative: in addition to being more interesting multi-functional additions to the laboratory, they also make for better polycrystalline rods! The kind of balloon used was 'Qualatex Pearl 260 (2" $\times$ 60") White'. Party balloons are made of stiffer latex, to which greater tension can be applied to stretch the balloon while packing the powder. This means that a greater pressure acts on the material from the wall of the balloon, helping hold it together while it is being shaped into a rod. An important step in forming the rod is to make sure it is entirely smooth and uniform in diameter along the entire length of the rod. This is critical for the next step, which is to evacuate the air from the balloon, tie a knot to seal it, and place it in a hydrostatic press to compact the powder into a dense polycrystalline rod. Any non-uniformities in the surface of the packed powder will cause the rod to break. The rod is then sintered for another 100 hours at the highest temperature at which it was previously sintered so as to achieve maximum density.

Crystal growth is performed using an infrared radiation furnace equipped with high power

elliptical halogen lamps (a typical furnace setup is illustrated in Fig. 3.6.) A polycrystalline rod (prepared using the method described earlier) serves as the 'feed' rod which hangs from the upper shaft in the furnace. The lower 'seed' rod may be a single crystal from a previous growth, or a piece of another polycrystalline rod attached to a mount. The growth process is illustrated in Fig. 3.7. The molten end of the feed rod is initially attached to the seed rod by bringing the two together. As the mirror stage moves upwards, the molten zone is held in place by means of surface tension, and multiple crystal grains begin to nucleate out of the seed crystal surface. However, only those preferred crystal grains with a faster growth rate dominate, and as the mirror moves upward, one grain will expand faster than the other grains, eventually taking up the entire growth volume. For the rest of the growth process, it is this single crystal that is grown.

For congruently melting compounds, the 'feed' and 'seed' rods used are of the same stoichiometric composition as the required compound. Incongruently melting compounds require a solvent (that serves as a flux) to be attached to the end of the seed rod in order to access the region of the phase diagram where the required compound is in equilibrium with the liquidus.

3.3.1 Image furnace grown single crystals

Single crystals of $A_2Cu(BO_3)_2$ were successfully grown for the first time using the image furnace technique, in a Crystal Systems Inc. infrared radiation furnace equipped with four 100 W halogen lamps. In spite of $A_2Cu(BO_3)_2$ being an incongruently melting compound, these growths could be carried out satisfactorily without a solvent, presumably because the peritectic temperature is not significantly lower than the liquidus for a stoichiometric mixture of elements. Polycrystalline rods were premelted at 18 mm/hr to form dense feed rods. Subsequently, crystal growth was carried out at a growth (upward mirror movement) speed of 0.5 mm/hr in 1 atm. of flowing O_2 to yield single crystals of several cm in length. In some cases, air trapped in the

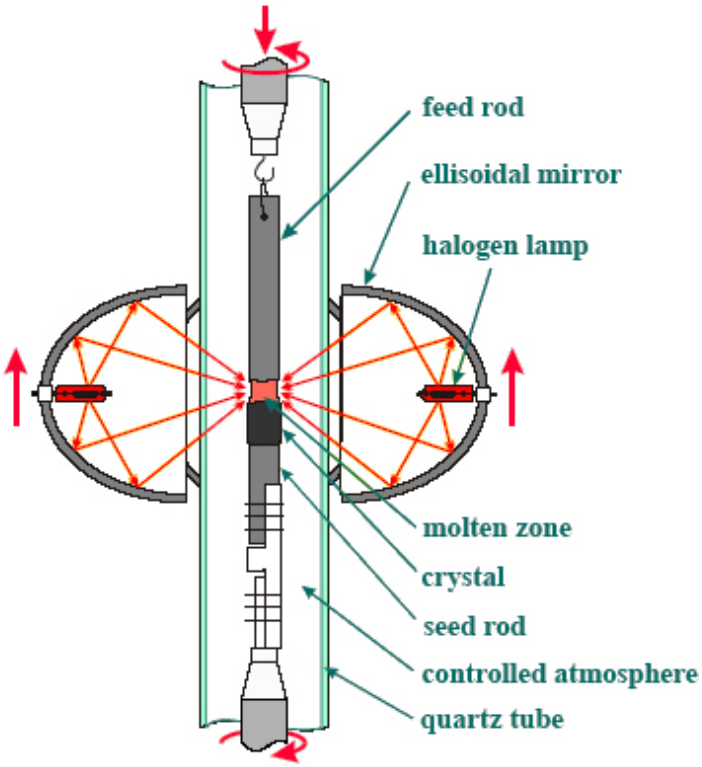

Figure 3.6. Travelling-solvent floating-zone (TSFZ) furnace schematic. Four elliptical mirrors focus the light from high-power halogen lamps onto a small volume of melt (the floating zone) suspended by surface tension between the polycrystalline feed rod and the grown crystal. As the hot zone slowly moves upward along with the mirror stage, material melts from the feed rod and joins the growing crystal. The upper shaft can also be moved upward or downward independently in order to adjust the rate at which material is added to the melt, so that the diameter of the crystal can be adjusted. The upper and lower shafts rotate in opposite directions, which mixed the melt, evens out any azimuthal asymmetries in the heating profile from the lamp images, and prevents the feed rod and grown crystal from fusing. The pressure and composition of the gas inside the quartz tube can be controlled to optimise the growth conditions. A video camera is used to monitor the growth. Figure from Crystal Growth Service Group, Max Planck Institute for Solid State Research.

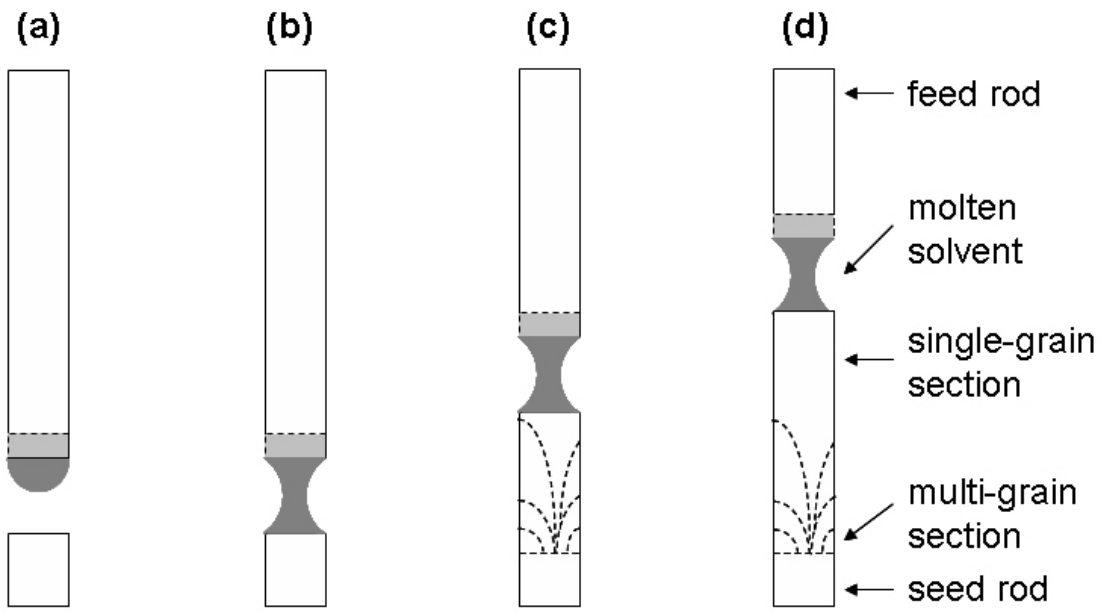

Figure 3.7. TSFZ growth schematic. (a) The feed rod is suspended from the upper shaft, and a seed rod is attached to the lower shaft. Mirrors melt the end of the feed rod, which remains suspended by surface tension. Some solvent penetrates into the feed rod on the surface (light gray). Denser rods are better to reduce the extent of penetration and thereby control the composition of the molten region. The dashed line inside the molten solvent indicates interior solid-liquid boundary. (b) Initial attachment is accomplished by lowering the upper shaft until the molten solvent contacts the seed crystal. (c) Growth proceeds by slowly raising the mirror stage (not shown) at 0.5 mm per hour. As the hot zone moves upward, material from the feed rod melts into the solvent and solidifies onto the seed crystal. During attachment, nucleation of multiple grains can occur in addition to extension of the seed crystal grain. (d) Crystal growth rates are not isotropic, and certain grains have preferentially faster growth rates. The grain with the best orientation for growth will expand faster than other grains, until it pushed other grains out completely. The remaining growth will then be single grain. Figure courtesy of O. Vajk.

polycrystalline feed rods was expelled during the growth process, leading to instability of the molten zone. In this case, a fraction of N_2 was added to the flowing O_2 to maintain stability of the molten zone. Typical single crystals grown of $Sr_2Cu(BO_3)_2$ and $Ba_2Cu(BO_3)_2$ were approximately 6 cm in length (shown in Fig. 3.8).

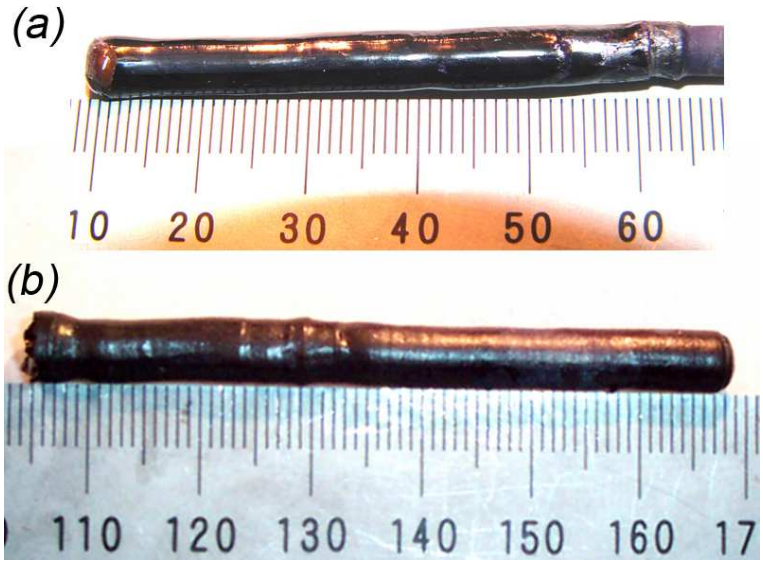

Figure 3.8. Typical single crystal grown using the travelling-solvent floating-zone technique in an image furnace (shown on a cm scale) (a) $Sr_2Cu(BO_3)_2$ (b) $Ba_2Cu(BO_3)_2$.

3.4 Structural characterisation

Structural characterisation of the grown single crystals was performed by X-ray and neutron diffraction. Powder X-ray diffraction patterns were taken at room temperature on pulverised single crystals to detect the presence of any impurity phases by comparing the diffraction pattern with calculated or previously reported patterns, and to confirm unit cell dimensions. Single crystal x-ray diffractometry was used to align smaller samples, while larger TSFZ-grown crystals (shown in Fig. 3.8) were aligned using neutron diffraction by collaborators at Paul Scherrer Insitute [30].

3.4.1 X-Ray diffraction

Powder X-ray diffraction patterns taken on pulverised single crystals can be used to detect the presence of any impurity phases by comparing the diffraction pattern with calculated or previously reported patterns, and to confirm unit cell dimensions. Measurements reported in this thesis were made using a Philips X'Pert PRO X-ray diffraction system using CuK_{α} radiation.

Real-time Laue X-ray backscattering is a tool to confirm the single-orientation of each single crystal. A small beam of broad-band X-rays is directed onto a spot on the sample. The location of backscattered photons is detected by ionization of a gas between wire grids. Bragg reflection of the incident beam occurs for diffraction planes with a wide range of diffraction plane spacing, and produces a spot pattern on the detector determined by the orientation of the crystal with respect to the incident beam. If the incident beam lies along a crystal symmetry axis, the spot pattern will reflect that symmetry. Crystals are mounted on a motorised goniometer, and a real-time display of the back-scattered X-rays can be monitored while the crystal orientation is adjusted.

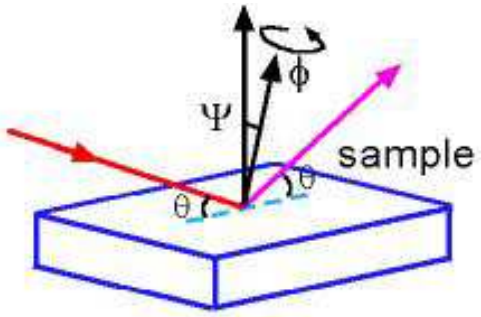

Figure 3.9. Schematic of pole figure measurement. An in-plane ϕ-scan at an azimuthal Ψ-angle tilt is illustrated.

Texture measurements are used to detect any misaligned crystalline grains by measuring the distribution of orientations in a sample. A texture measurement is also referred to as a pole figure as it is often plotted in polar coordinates consisting of the tilt and rotation angles with

respect to a given crystallographic orientation. A pole figure is measured at a fixed scattering angle θ (constant d-spacing) and consists of a series of ϕ-scans (in-plane rotation around the center of the sample) at different tilt or Ψ (azimuth) angles, as illustrated in Fig. 3.9.

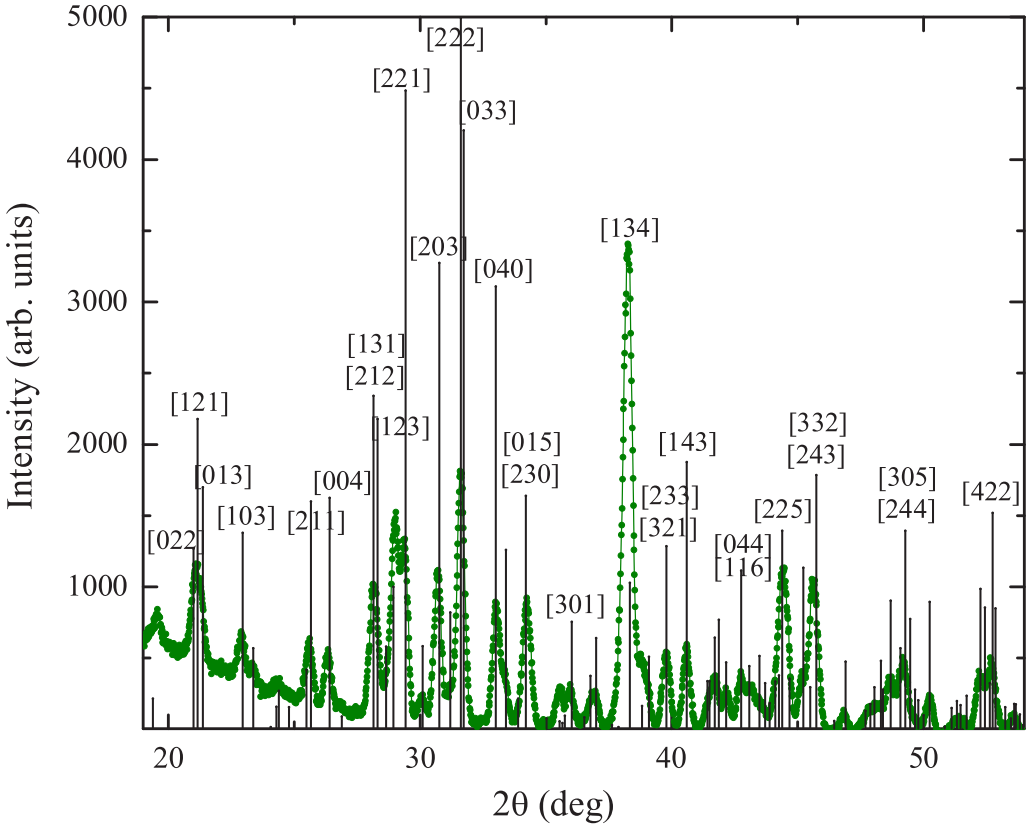

Figure 3.10. $Sr_2Cu(BO_3)_2$: X-ray diffraction pattern of a powdered single crystal (shown in green) compared with the calculated pattern (shown in black). Most intense diffraction peaks are labelled.

3.4.2 Single crystal purity

The grown crystals were verified to be of the right phase using powder X-Ray diffraction (XRD). Powder XRD patterns taken at room temperature on single crystals of $Sr_2Cu(BO_3)_2$

are compared with calculated patterns in Fig. 3.10. Fig. 3.11 compares powder XRD patterns on single crystals of $BaCuSi_2O_6$ with calculated patterns. The peaks match well, and there are no additional peaks from additional impurity phases.

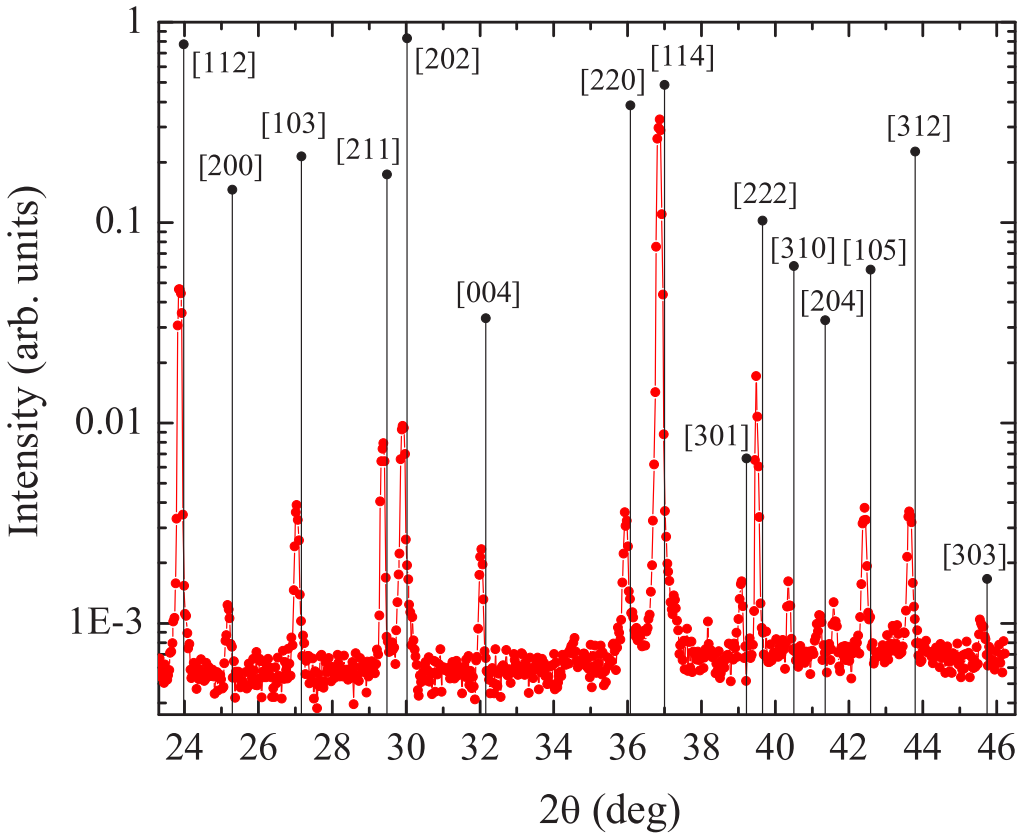

Figure 3.11. $BaCuSi_2O_6$: Xray diffraction pattern of a powdered single crystal (shown in red) measured at the Stanford Synchrotron Radiation Laboratory, compared with the calculated pattern (shown in black).

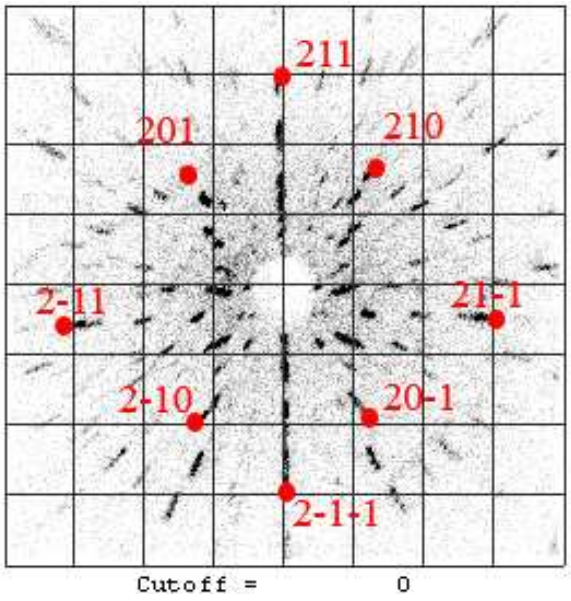

Figure 3.12. $Sr_2Cu(BO_3)_2$: Laue X-ray backscattering image with incident X-rays parallel to the orthorhombic a-axis (out of the page). The most intense peaks are labelled.

3.4.3 Single crystal orientation

The well defined spots of high intensity arranged in a high symmetry pattern in the Laue XRD pattern obtained (shown for a representative single crystal of $Sr_2Cu(BO_3)_2$ in Fig. 3.12 and $BaCuSi_2O_6$ in Fig. 3.13) indicates well defined single crystals in a single orientation. In practice, the intensity of Laue patterns was often inadequate for precise orientation due to the large unit cell (i.e densely filled reciprocal space), and large number of light atoms (i.e. reduced scattering power). In order to align single crystals along particular orientations, XRD in the X'Pert PRO system using a single x-ray wavelength to map the real space orientation to peaks in reciprocal space was favoured to orient samples. Pole scans were performed on $BaCuSi_2O_6$ samples, which revealed the spread in crystallite orientation to be $\leq 0.03°$.

An interesting feature of single crystals of $BaCuSi_2O_6$ is the polarisation of light emitted through the crystal. The wavelength of light emitted differs depending on the orientation of the

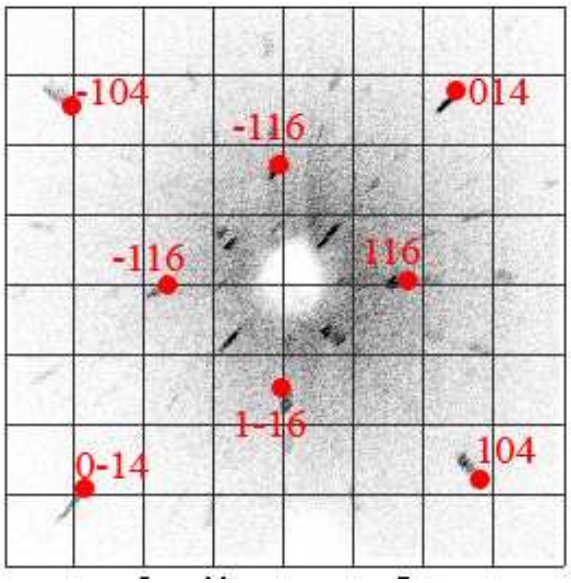

Figure 3.13. $BaCuSi_2O_6$: Laue X-ray backscattering image with incident X-rays parallel to the tetragonal c-axis (out of the page). The most intense peaks are labelled.

crystal (Fig. 3.14 shows the optical emission spectrum using a laser beam of 532 nm wavelength (2.33 eV) [52]). These experiments were performed by transmitting the laser beam through the crystal to a detector, the crystal is rotated to obtain an angular dependence of the transmitted frequency. This provides a useful tool to check for crystal orientation by optical inspection under a transmission microscope. While the light transmitted in the [001] direction is in the purple part of the spectrum, light transmitted perpendicular to the [001] direction is in the pink part of the spectrum. If light of different wavelengths is transmitted through a sample in a single orientation, it can be inferred that the sample comprises differently oriented grains.

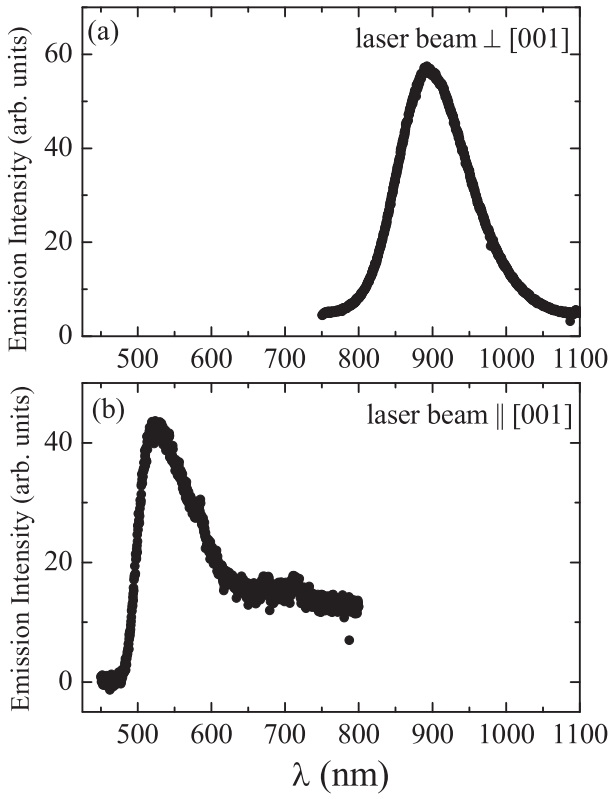

Figure 3.14. $BaCuSi_2O_6$: Optical emission data using a laser of 532 nm wavelength (2.33 eV) (a) with the laser beam perpendicular to the crystalline c-axis (b) with the laser beam parallel to the crystalline c-axis.

Chapter 4

Experimental Techniques

"So this is how the world works, all energy flows according to the whims of the great magnet."

-Hunter S. Thompson

Much of the experimental work performed as part of this dissertation requires high magnetic fields. These experiments were conducted at the National High Magnetic Field (NHMFL) laboratories at Tallahassee and Los Alamos. Discussion in this chapter contains a summary of the various types of magnets used for this purpose, and details of experimental techniques used. This chapter also contains a brief introduction to the experimental technique of inelastic neutron scattering, which was performed on powdered samples of the spin dimer compounds as part of the research presented in this thesis.

4.1 Magnets Used For High Fields

Very high magnetic fields can only be generated with electromagnets; solenoids are an efficient geometry. They are wound from superconducting wires, or conductors with normal resistivity. Superconductors are constrained by critical current density, temperature and field, as well

as mechanical properties, such as ultimate strength and strain tolerance. Typically, superconducting magnets are used for fields below 20 T. While resistive magnets are not constrained by any critical properties as are superconductors, they require electric power, efficient cooling and competent stress management - power requirements become excessively large with size of field. Currently, resistive magnets provide fields up to 33 T, whereas continuous fields of up to 45 T are produced by a superconducting / resistive hybrid magnet. For magnetic fields as high as 65 T, short pulsed magnets are used.

4.1.1 Resistive magnets

A resistive magnet generates its magnetic field by passing current through a coil of wire. To increase the magnetic field strength, a resistive magnet requires a larger current passing through the wire. As the current level increases, so does the resistance in the wire, resulting in energy losses (through heat dissipation), thereby limiting the maximum field strength attainable. It is crucial for these magnets to be continuously water cooled to counter the enormous heat dissipation. The bulk capital outlay involved is in the power supply required to drive the magnet. Some of the experiments described in this dissertation (requiring fields up to 33 T) were performed in the resistive magnets at NHMFL, Tallahassee. These resistive magnets are built using the Florida-Bitter design. A Bitter magnet is constructed of perforated, round, wide conductor plates, the 'Bitter disks' made from sheet metal of copper or copper alloys, interleaved with insulators which are stacked to form a thick monolayer winding (shown in Fig. 4.1). The insulators cover less than 360° of the surface to provide the contact surface between the disks. The disks and insulators are clamped together with tie rods between two endplates to provide contact pressure and sufficient mechanical support. The current through the conducting disks distributes radially inversely proportional to the radius. The holes in the stacked disks and insulators form circular cooling channels through which water is pumped at a high flow rate to

remove the dissipated electrical power. The Florida-Bitter design used in the NHMFL, Tallahassee improves on the Bitter magnet by using cooling slits instead of holes, thereby increasing the cooling surface without a penalty in electrical resistance from the radial space factor. These design improvements and conducting alloy development have enabled the generation of 33 T magnetic fields with electric power consumption of the order of 17 MW.

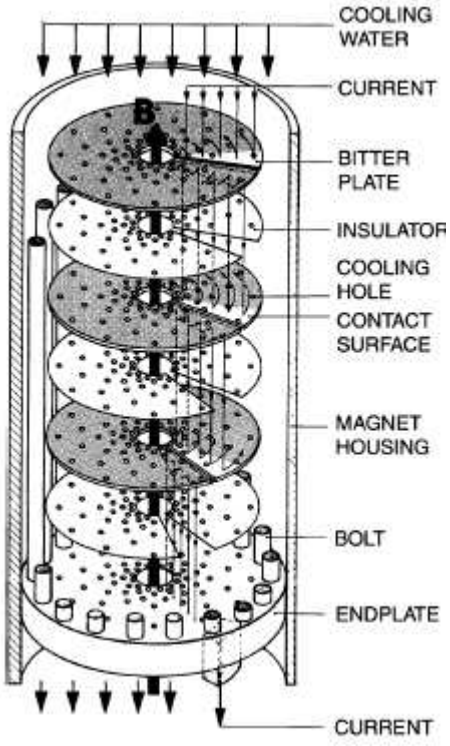

Figure 4.1. Schematic of a Bitter resistive magnet used for generating high magnetic fields up to 33 T. Figure from Ref. [53].

4.1.2 Superconducting magnets

Superconducting magnets minimise the energy losses characteristic of resistive magnets. The coils of wire of superconducting material that carry the electrical current are maintained below the superconducting temperature. At these low temperatures, the current that is flowing in the coils can be increased to very high levels, resulting in very high magnetic field strengths. Once

the desired field strength is established, the electrical current source is shut off (via a superconducting switch) and the coil of superconducting wire becomes a closed loop. In the ideal non-dissipative case, as long as the low temperatures are maintained for the superconducting wire, the electrical current will flow indefinitely. In practical application, the current flowing in the wire will encounter some degradation due to a low level of resistance in the wire. As the wire heats up slightly, its resistance increases and opposes the flow of current, which therefore begins to reduce the strength of the magnetic field. To avoid this, the main magnetic coils in a superconducting magnet remain immersed in liquid helium to maintain low temperatures. The magnetic field that can be produced by a superconducting magnet is limited to the critical field of the superconductor at the temperature of operation. In the case of a superconducting magnet, the chief operating cost is the need for constant cryogenic cooling. Several of the experiments described in this dissertation, performed as part of characterisation of spin dimer compounds at moderate fields were performed in superconducting magnets. These include the commercially available Quantum Design Magnetic Property Measurement System (MPMS) Superconducting Quantum Interference Device (SQUID) magnetometer for magnetic fields up to 5 T, and the superconducting magnet for magnetic fields up to 20 T at the NHMFL, Los Alamos.

4.1.3 Hybrid magnet

In a hybrid magnet system, resistive and superconducting magnet technologies are combined - taking advantage of the strengths of each. A hybrid magnet (schematic shown in Fig. 4.2) is composed of a superconducting magnet providing a limited magnetic field which takes the place of the outer portion of the resistive coil, with a powered resistive magnet operating as an insert at the centre of the coil, providing the balance of the field beyond the limit of the superconducting magnet. Reducing the requirement for field from the resistive magnet reduces the requirement for power and cooling. Since heat dissipation limits the magnetic field achiev-

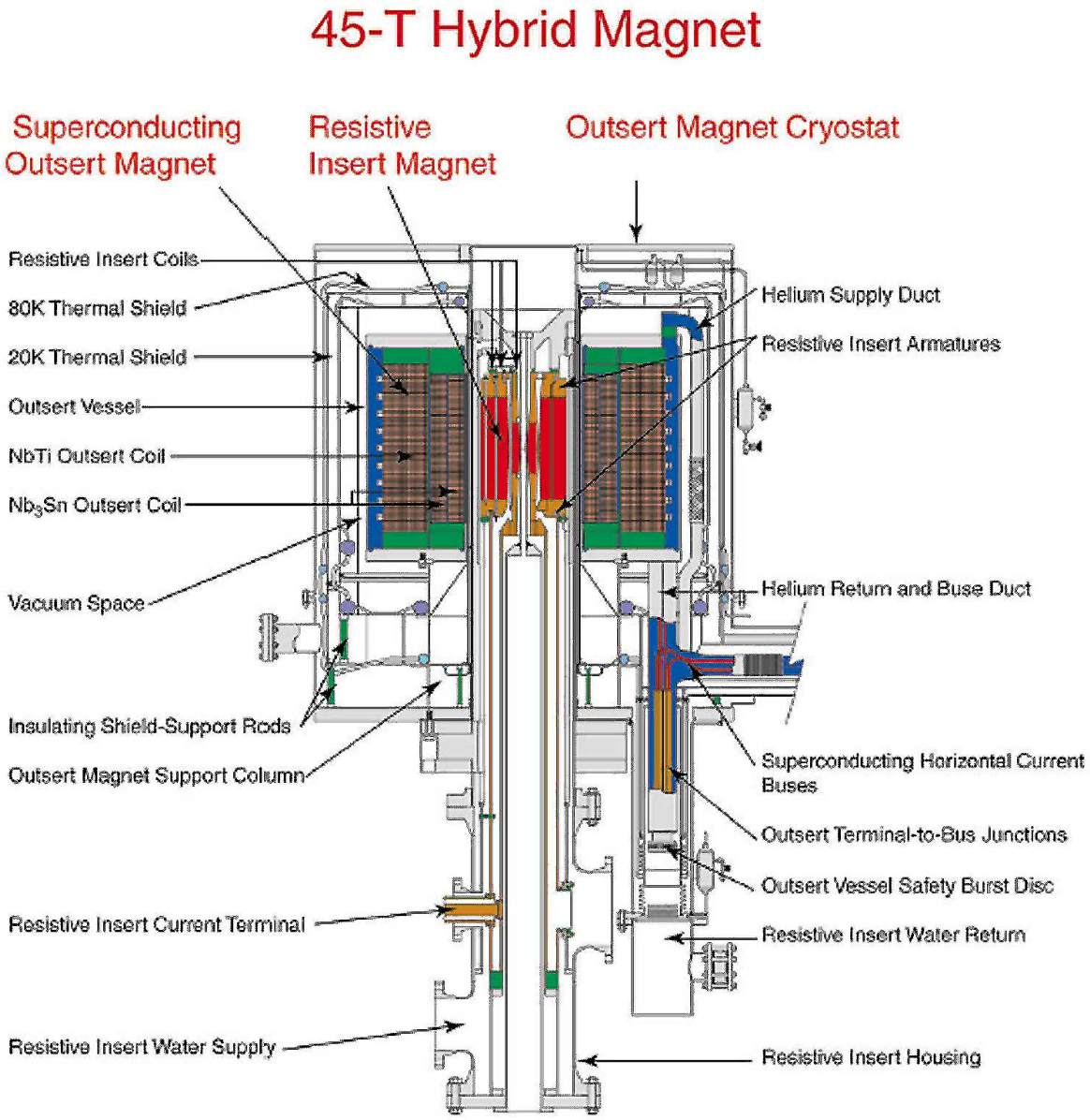

Figure 4.2. Sectional drawing showing the major components of the hybrid magnet at NHMFL, Tallahassee. Figure from Ref. [53].

able by solely resistive magnets, a hybrid magnet system is an effective way to achieve steady magnetic fields of above 33 T. Existing hybrid magnets have insert magnets consisting of more than one coil to allow for power distribution to more favourable places within the magnet to optimise for the stress levels and heat dissipation. The hybrid magnet at NHMFL, Tallahassee is capable of producing magnetic field up to 45 T. It consists of five concentric Florida-Bitter coils and disks from Cu, CeBe, CuAg and CuZr. Heat capacity and magnetocaloric effect measurements performed up to 36 T described in this dissertation were performed using the hybrid magnet at the NHMFL, Tallahassee.

4.1.4 Pulsed magnets

Short pulses (lasting about 30 ms - pulse shape shown in Fig. 4.3) of high magnetic fields up to 65 T are provided by capacitor bank driven resistive solenoid magnets at the NHMFL, Los Alamos. The capacitor bank consists of several capacitors; each capacitor (with capacity around 1.67 mF and the ability to store 83 kJ at a rated voltage of 10 kV) has a discharge resistor with a long time constant (10 min) directly connected to its terminals. The typical pulsed magnet's central component, its coil, is formed by wrapping conducting wire around a cylinder for 300 turns. A schematic of the cross section of the 65 T short pulse magnet at the NHMFL, Los Alamos is shown in Fig. 4.3. The high voltage capacitance bank (of around 1.2 MJ capacity) is rapidly discharged through the coil, inducing a magnetic field pulse. The electric energy supplied to the coil by the current pulse is not completely converted into magnetic energy but also partly dissipated in the coil as heat. Before every experiment ('shot') the high field coil has to be cooled by liquid nitrogen reducing its resistance and allowing to get 65 T. The magnetic field creates stresses of 1 - 3 GPa on the magnet in the process, and the wire in the coil needs to be able to handle this stress (for example Copper wire would not be strong enough.) The high-tech wires used instead are a combination of copper strengthened by

fine filaments of aluminum, silver or niobium. The material for the magnet itself needs to be carefully chosen because of the high stress and abnormal heating, which would destroy several metals. The 65 T magnet at the NHMFL, Los Alamos utilises a nested two-coil assembly, with the two coils connected in series, and a cooling gap between the coils. A poly layer assembly process is used, using Cu-Nb for the conducting coil, and customised new materials such as organic composites for reinforcement. The bore diameter possible with these magnets is significantly smaller than other types of magnets. Experiments described in this dissertation in magnetic fields up to 64 T were performed in the short pulsed magnet at the NHMFL, Los Alamos.

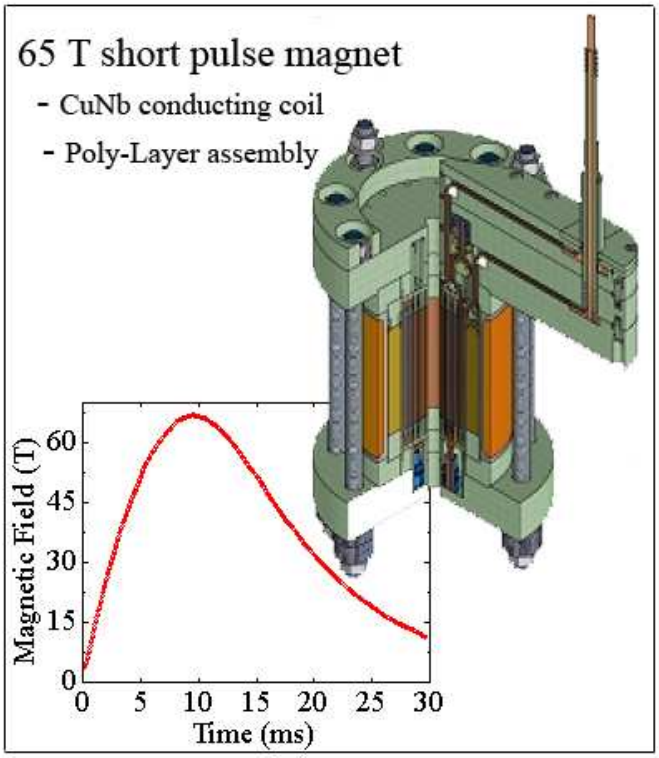

Figure 4.3. Sectional drawing showing the major components of the 65 T short pulse magnet at NHMFL, Tallahassee. The inset shows the shape and duration of a magnet pulse. Figure from NHMFL, Los Alamos.

4.2 Low field characterisation

4.2.1 Magnetisation, Specific Heat

Magnetisation measurements primarily to screen samples for impurity content (unpaired spins) were made in a Quantum Design Magnetic Property Measurement System (MPMS) Superconducting Quantum Interference Device (SQUID) magnetometer for temperatures between 1.8 and 350 K and applied magnetic fields up to 5 T. Samples of 1 mg up to 300 mg were mounted between two clear plastic drinking straws for measurements, with sample alignment performed by hand.

Specific heat measurements as part of sample characterisation were made using the heat capacity option of the Quantum Design Physical Property Measurement System (PPMS). This instrument uses a relaxation technique, in which the sample is briefly heated and then allowed to cool. The thermal response of the sample is then fit over the entire temperature response using a model that accounts for the thermal relaxation of both the sample and the sample platform. The samples were attached to the heat capacity platform with Apezion grease. The thermal response of the platform and grease was measured separately to allow for the subtraction of this component from the final measurement. To achieve maximum accuracy within reasonable time constraints, the system was typically allowed to cool for two time constants. Thermal contact with the environment was minimised by evacuating the sample chamber to approximately 0.01 mTorr. A sample with a flat face is important for these measurements in order to ensure good thermal contact between the platform and the sample.

4.3 Measurements in High Magnetic Fields

4.3.1 Specific Heat, Magnetocaloric effect in static fields

Specific heat in high magnetic fields was measured using standard thermal relaxation techniques by means of a custom-made quasi-adiabatic calorimeter, in collaboration with M. Jaime of NHMFL, Los Alamos. The calorimeter used to obtain experimental results reported in this dissertation consists of a Silicon platform suspended by nylon string (dental floss) on which the sample, thermometer and heater are mounted (shown in Fig. 4.4) such that the system is thermally well isolated. In the thermal relaxation method, the heat (Q) to the sample is supplied in the form of rectangular pulses with typical time period of the order of seconds. The calorimeter is thermally connected to a heat bath by an Au wire with thermal conductivity κ. After the heat is switched on (or off), the calorimeter relaxes to a new thermal equilibrium situation with a fixed temperature step, which typically amounts to ΔT = 5%. The heat capacity is obtained by fitting the time evolution of the temperature of the calorimeter to a single-exponent. After determining the characteristic relaxation time in the experiment (τ) and the thermal conductivity of the heat-link ($\kappa = Q/\Delta T$) for each temperature, the heat capacity is calculated according to: $C_p = \tau \cdot \kappa$, and contribution from the addenda subtracted to obtain the sample heat capacity. The relaxation time constant (τ) determined by the Au thermal link is necessarily much longer than the internal relaxation time (i.e. the time it takes for the thermometer to be in thermal equilibrium with the sample and addenda), typical relaxation constants lie in the range 1 - 10^2 s.

The same setup was used to measure the magnetocaloric effect (MCE). This is defined as the temperature change of a magnetic material due to the application of a magnetic field. The physical origin of the MCE is the coupling of the magnetic sublattice to the applied magnetic field, H, which changes the magnetic contribution to the entropy of the solid. When the

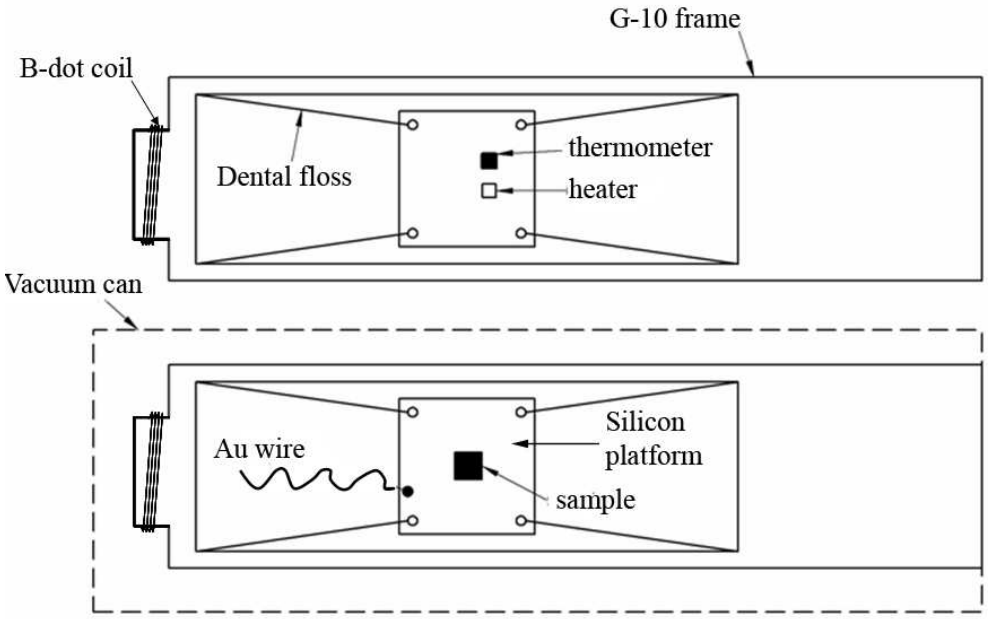

Figure 4.4. Quasi-adiabatic and thermal relaxation calorimetery. Power is supplied to the sample mounted on the Si platform via the heater, and is measured by the thermometer. Heat drains to the thermal bath through the Au wire. The magnetic field is measured by the 'B-dot' solenoid, in which a voltage proportional to dB/dT is induced. Figure courtesy of P. Sharma $\&$ M. Jaime.

magnetic field is applied adiabatically (i.e. the total entropy remains constant) in a reversible process such that the magnetic order increases (decreases), the magnetic entropy decreases (increases), but since the total entropy does not change, the temperature increases (decreases). The converse effect is seen with reversal in magnetic field. This adiabatic temperature rise (fall) is a measurement of the MCE in the material. The expression that characterises the magnetocaloric effect is given by:

$$\Delta T_{ad}(T, \Delta H) = -\int_{H_1}^{H_2} \left(\frac{T}{C(T,H)}\right)_H \left(\frac{\partial M(T,H)}{\partial T}\right)_H dH \tag{4.1}$$

A direct measure of MCE involves the measurement of the initial and final temperatures of the sample, when the external magnetic field is rapidly changed from an initial to a final value.

4.3.2 Magnetisation in pulsed fields

Magnetisation measurements in 65 T pulsed magnetic fields at NHMFL, Los Alamos were performed in collaboration with N. Harrison. Pulsed field magnetometers take advantage of the high dB/dt environment produced by a pulsed magnet by measuring the voltage $\propto\ dM/dt$ induced in a coil by the rapidly changing magnetic moment of the sample. In order to be successful, the signal produced by the sample must be carefully separated from the signal produced by the coil alone. This is achieved via a three-stage process. The coil into which the sample is placed is made up of two coils counter-wound in series, with a total of around 1500 turns. Fractions of turns are added or removed so as to balance the areas of the two coils with the aim of minimising the pick-up of the empty coil in the presence of a changing magnetic field. In addition, a single turn compensation coil is present on the magnetometer. The signals from the sample and compensation coils are subtracted electronically during the measurement in such a way that there is no induced voltage when a low field pulse is performed with the sample coil empty. A custom-built amplifier is used to perform the subtraction in addition to amplifying the induced voltage by gains of up to 50,000 times. Finally, the sample is mounted so that it can be inserted into and extracted from the coil without removing the magnetometer from the magnet. Two magnetic field pulses are then performed with identical control settings, one with the sample inserted and one with it extracted. The resulting datasets are subtracted from one another, yielding a highly accurate and consistent measurement of the sample's magnetic moment.

The coils need to be made large enough for the sample to be moved in and out of the coils (in-situ) between pulses. The inner diameter of the pick-up coil is approximately 1400 microns (1.5 mm long) in order to accommodate a capsule that contains the sample. For pulsed field experiments performed on the spin dimer compounds with a large spin gap, it was crucial to

maximise the volume of the sample that fit in the detector coil, in order for the magnetisation signal to exceed the noise floor. For this purpose, the sample holder was dispensed with, and samples were shaped into the size of the sample holder to precisely fit the detection coils.

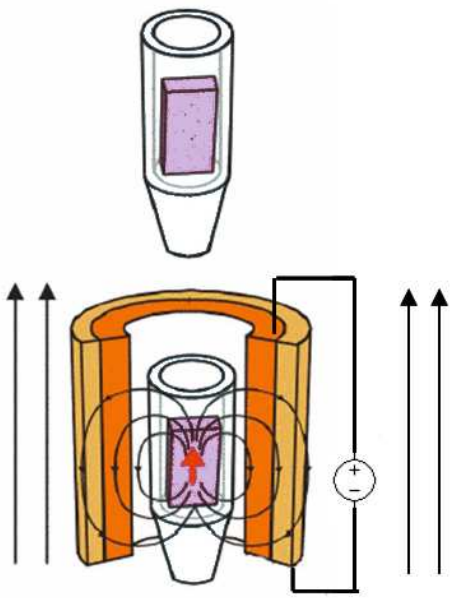

Figure 4.5. Schematic of sample holder in pick-up coil. Two magnet 'shots' are performed, one with the sample holder inserted and one with it extracted, and the induced emf in the pick-up coil recorded. Figure courtesy of N. Harrison.

The magnetic field at the sample position when the magnet is pulsed is recorded by means of a 'B-dot' solenoid placed near the sample on the end of the probe. When the magnet is pulsed, voltage proportional to rate of change in magnetic flux dB/dt is induced in the 'B-dot' coil. The multichannel digitizer records each of the voltage changes at a fixed rate of time (converting it from analog to digital). The waveform of dB/dt is recorded by the digitizer and then integrated by data acquisition software to obtain a time profile of the magnetic field. The resulting profile is a waveform showing the magnetic field at each moment in time. The magnetisation is obtained by integrating the signal dM/dt using the data acquisition software.

This is then calibrated with the magnetisation at low fields measured in a commercial system such as the Quantum Design MPMS SQUID to obtain the absolute magnetic moment at high magnetic fields. Also part of the set-up is a temperature controller to monitor the conditions surrounding the sample. This method yields an accurate and consistent measurement of the magnetisation in fields as high as 65 T and temperatures as low as 370 mK.

4.3.3 Torque magnetisation in static fields

Cantilever magnetometers are among the few measurement devices compact and yet sensitive enough to be of practical application within the confines of a ^{3}He/^{4}He dilution refrigerator cryostat in high magnetic fields. The general principle behind all cantilever magnetometry is that a magnetic sample mounted on a flexible beam will respond to the application of a quasi-static magnetic field by experiencing a force and a torque which deflects the flexible beam. For the purpose of experiments reported in this dissertation, a cantilever magnetometer was used to measure the torque induced by the anisotropic magnetic moment of the sample, and is referred to as a torque magnetometer.

Temperature control for the measurements described in this dissertation was obtained using an Oxford Instruments top loading ^{3}He/^{4}He dilution refrigerator in the bore of the resistive magnet. The base temperature for this instrument is 25 mK, with the possibility of raising the temperature to a maximum of around 1000 mK. The temperature can be monitored with a ruthenium oxide resistor, and adjusted by changing the cooling power of the system. Due to the high sensitivity to small changes in temperature of the dilution refrigerator, slow field sweeps are essential, and an extended equilibration time is required after changing the ambient temperature of the experiment. The magnetoresistive effect that affects the temperature reading of resistive thermometers in high magnetic fields must also be kept in mind, which renders it impossible to measure temperature in a changing magnetic field. The only reliable temperature

reading is at equilibrium at zero field. To record an accurate temperature reading during magnetic field sweeps, therefore, the temperature is initially set by adjusting the heater power at zero field, and allowed to stabilise for an extended period before the magnetic field is ramped. The magnetic field is then swept up to measure the magnetic field response of the sample, and swept back down at a slow sweep rate of 2 T/min. At zero field at the end of the magnetic field sweep, it is verified that the final temperature reading coincides with the initial temperature reading before the field sweep, an indication of temperature stability during the entire field sweep. Given that the data is acquired within the first 25% of the time window of the total up and down sweep, the experimental uncertainty in temperature is less than the difference in the temperature reading ($\sim 5\%$) in zero field between the beginning and end of the magnetic field sweep.

A schematic of the torque magnetometer used for experiments performed as part of my research, in collaboration with L. Balicas and N. Harrison at NHMFL, Tallahassee is shown in Fig. 4.6. Here it is seen that the sample is attached to the flexible beam of the magnetometer, which forms one plate of a parallel plate capacitor, while the other face lies stationary. The fixed plate is rotatable about an axis parallel to the axis of torque but perpendicular to the applied magnetic field (schematic of probe with sample rotator shown in Fig. 4.7). As the magnetic moment of the sample experiences a torque in the applied magnetic field, the cantilever beam is deflected, thereby changing the capacitance of the device. The entire arrangement is mounted on a cylindrical cryogenic fibreglass (G-10) holder, which can be inserted into the probe.

For the experiments described in this dissertation, the torque arises from an anisotropy in g-factor between the crystalline c- and a- axis (described in Appendix B), with the largest g-factor along the crystalline c-axis. Hence the sample is mounted with a small angle ($< 10^{\circ}$) between the applied field and the c-axis (normal to the sample plane), such that the applied field exerts a torque on the crystal due to the difference in g-factor between the a and c orientations.

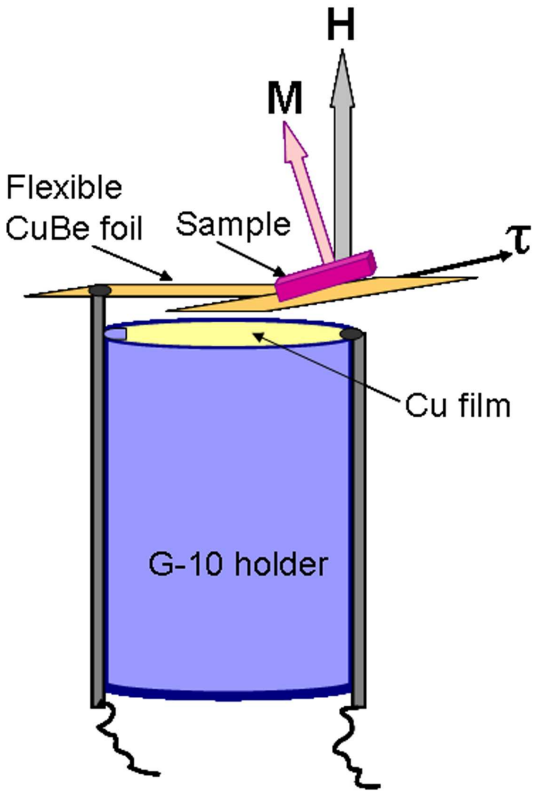

Figure 4.6. Schematic of torque magnetometer. The sample is attached to the thin flexible plate (material and thickness chosen depending on size of moment, 0.5 μm thick CuBe foil was used for the experiments described here) with GE varnish, and the metal fixed plate (Cu film for these experiments) is attached to the cylindrical holder.

On entering the magnetically ordered phase with increasing magnetic field, the anisotropy in magnetisation (due to the g-factor anisotropy) causes a sudden increase in torque, as the field attempts to align the c-axis more closely with the applied magnetic field. Due to the large sample weight ($\sim$ 2 mg) required for adequate signal ($\sim 10^{-2}$ emu), a stiff cantilever made out of $5\mu m$ thick CuBe film was used for these measurements.

For the cantilever geometry shown in Fig. 4.6, the voltage across the capacitor is directly proportional to the distance between the plates (at zero voltage, the plates are separated by $\sim$ 50 $-$ 200 μ m). For small deflections, the torque is directly related to the displacement,

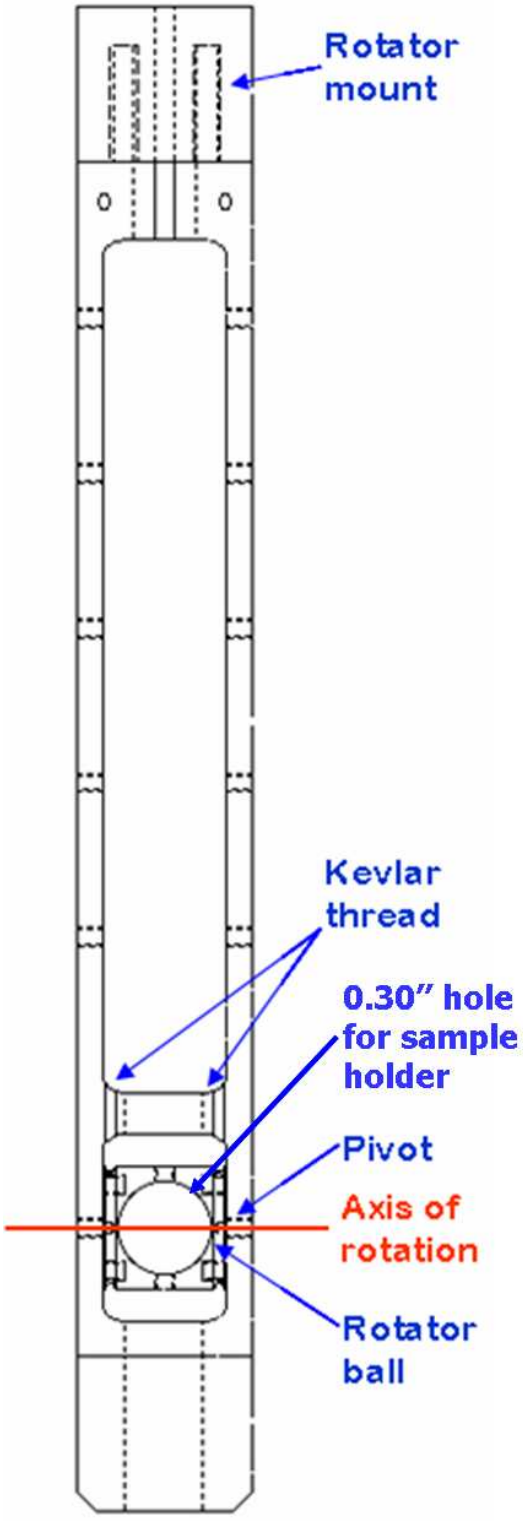

Figure 4.7. Schematic of rotator on which cantilever is mounted for insertion in the ^{3}He/^{4}He dilution refrigerator. Figure from NHMFL, Tallahassee.

which can be measured as a change in voltage across the parallel plates with the lock-in amplifier. The measured torque in turn gives a measure of the magnetisation, since $\tau = \mathbf{M} \times \mathbf{H}$. The finite value of torque arises from the anisotopy of the g-vector which causes **M** and **H** to be non-parallel. In order to measure the absolute magnetisation, values are calibrated with the absolute moment measured by another means (for example using a pulsed field magnetometer.) Hence, by measuring the change in potential across the parallel plate capacitor as a function of applied field, one can directly measure the magnetisation of a given sample.

The change in electrostatic potential can then be measured using an AC capacitance bridge in conjunction with a lock-in amplifier. An audio-oscillator drives the capacitance bridge with an excitation voltage (30 rms V at 5 kHz for the experiments described in this dissertation). One arm of the bridge is provided by the capacitance from the cantilever, and another arm by a variable capacitance. At zero field, the variable capacitance is adjusted (1.3 pF for our experiments) to null the voltage across the capacitance bridge. Hence, in an applied field, when the cantilever capacitance varies, there is a resulting voltage across the capacitance bridge which is output to the lock-in amplifier. The output measures the change in potential resulting from the differential capacitance ($\sim 10^{-5}$ pF), and is in the order of microvolts, providing an extremely sensitive measure of cantilever deviation as a function of applied field.

4.4 Inelastic Neutron Scattering

Inelastic neutron scattering is a useful method to probe the magnetic density fluctuations (spatial and temporal density) of a magnetic material. A neutron beam carries no charge, but has a magnetic moment which enables it to interact with the unpaired spins on a length scale of the order of the atomic size ($\sim$ 1 Å). The quantity measured in a scattering experiment is a cross section

$$\frac{d^2\sigma}{d\Omega dE} = \frac{n'}{Jd\Omega dE} \tag{4.2}$$

where n' is the number of neutrons scattered per second into dΩ in the direction (Θ , ϕ) with final energy between E and $E + dE$, and J is the incident neutron flux:

$$\frac{n'}{Jd\Omega dE} = \frac{k_f \quad \text{(scattered wave vector)}}{k_i \quad \text{(initial wave vector)}} S(\mathbf{Q}, \omega) \tag{4.3}$$

Here, $S(\mathbf{Q}, \omega)$ is the dynamic structure factor, which can be viewed as the correlation function between spins. In the case of a spherically symmetric powder sample (which is the case described as part of this dissertation), $S(\mathbf{Q}, \omega)$ is smeared out by spherical averaging, which transforms $S(\mathbf{Q}, \omega) \rightarrow S_{\text{powder}}(Q, \omega)$, and results in information loss. In order to extract as much information as possible from a powder sample, it is necessary to survey a large domain of $E - Q$ space. Experiments performed as part of this dissertation in collaboration with Ch. Ruëgg, H. Ronnow, and D. McMorrow were at the MARI direct geometry chopper spectrometer at the ISIS pulsed neutron facility at the Rutherford Appleton laboratory. This facility is ideal, due to its large area detector coverage. In this facility, a white neutron beam is monochromated by a Fermi chopper which rotates at frequencies of up to 60 Hz and is phase to the neutron pulse. The energy transferred to the sample is then calculated from the time of flight of the scattered neutron. MARI provides continuous detector coverage over an angular range of 3.4° to 134° with a sample to detector distance of 4m. This means that in the relation for the wavevector transfer $|\mathbf{Q}| = \mathbf{k_f} - \mathbf{k_i}$, or equivalently:

$$\frac{\hbar^2 \mathbf{Q}^2}{2m} = 2E_i - \hbar\omega - 2\cos\phi[E_i(E_i - \hbar\omega)]^{\frac{1}{2}} \tag{4.4}$$

an entire range of $\mathbf{Q}$ values can be measured for each value of energy transfer $\hbar\omega$ by varying the detection angle ϕ. Hence we obtain two-dimensional plots of intensity as a function of energy transfer and wavevector transfer.

Chapter 5

Inter-dimer exchange in $A_2Cu(BO_3)_2$ (A = Sr, Ba)

"No, no! The adventures first," said the Gryphon in an impatient tone: "explanations take such a dreadful time."

- Lewis Carroll, Alice's Adventures in Wonderland

The family of spin dimer compounds $A_2Cu(BO_3)_2$ (A = Sr, Ba) has a relatively large spin gap of the order of $J \sim 100$ K (8.6 meV) separating the singlet groundstate from the triplet excited state in zero magnetic field. Since the inter-dimer coupling is very weak, magnetic fields of the order of $\frac{J}{g\mu_B} \sim 69$ T are required in order to access the magnetically ordered state. While this means that experiments that directly probe ordered state properties are largely out of reach, pulsed magnetic fields up to 65 T at the NHMFL, Los Alamos make it possible to measure the critical magnetic field (which is reduced below 69 T due to weak inter-dimer coupling) and hence the spin gap via magnetisation experiments. These measurements gives us valuable information about the effect of the inter-dimer AF exchange couplings on the size of the spin gap. We are also able to tune the spin gap by changing inter-dimer coupling through chemical

pressure (i.e. substituting Ba^{2+} for Sr^{2+}). A more direct probe of the inter-dimer coupling is provided by measuring the triplon dispersion by powder INS experiments.

5.1 Low magnetic fields: an estimate of J

The strong intra-dimer exchange interaction (J) coupling the two Cu^{2+} $s = 1/2$ spins within a dimer can be estimated from low field measurements. From the exponential behavior of the susceptibility at low temperatures (Fig. 5.1), it is clear that the material is characterised by a substantial spin gap. Considering the predominant antiferromagnetic intra-dimer exchange interaction (J) alone, the simplified 'isolated'-dimer model is represented by the Hamiltonian

$$\mathcal{H} = \sum_{\langle,|\rangle} J\mathbf{s_i} \cdot \mathbf{s_j} \tag{5.1}$$

The groundstate is a product of singlets, and the excited state for this simplified model is a dispersionless triplet at energy J. This model can be used as a simple approximation to estimate the intra-dimer coupling J from fitting to the experimentally measured magnetic susceptibility. We obtain an expression for the isolated-dimer susceptibility by a simple estimate of the thermal population of singlet and excited triplet levels using the Boltzmann distribution:

$$\chi_0 = \frac{N(\mu_B g)^2}{k_B T(3 + \exp(\frac{J}{k_B T}))} + \frac{R}{T} + \chi_c \tag{5.2}$$

where N is Avogadro's number, R the Curie constant due to non-interacting impurities and χ_c a temperature-independent term. Any weak inter-dimer terms can be treated in a mean field manner (i.e.) their effect is equivalent to an average antiferromagnetic field acting on the triplets, which competes with the external magnetic field. The effect of these terms is to renormalise this expression as shown below, but otherwise leave the functional form unchanged.

$$\chi_{MF}(T) = \frac{\chi_0(T)}{1 + \chi_0(T)\, J'\, k_B/N(\mu_B g)^2} \tag{5.3}$$

The fit value of g using the isolated-dimer model therefore overestimates the actual value of g taking into account the inter-dimer coupling, and the extent of the deviation indicates an approximate measure of magnitude of inter-dimer coupling. For all three orientations, the magnetic susceptibility per mole of Cu spins as a function of temperature can be well fit by the isolated-dimer model. The value of J for all three orientations is found from these fits to be 8.6 $\pm$ 0.05 meV in agreement with previous polycrystalline data [18]. Values for g are found to be 2.0 $\pm$ 0.05 for H aligned along the *b* and *c*-axes, but 2.2 $\pm$ 0.05 for H aligned along the *a*-axis, consistent with the orientation of the CuO_4 units. R varies from 0.001 to 0.003 emuK/molOe, corresponding to 0.3% to 0.8% impurity concentration, assuming impurity spins with g = 2, $s = \frac{1}{2}$. The T-independent term χ_0 is small and positive, likely due to a very small concentration of ferromagnetic impurities. Values vary slightly between samples and with orientation, and for the data shown in Fig. 5.1 correspond to approximately 10^{-4} μ_B per formula unit.

Independent measurements of g give an estimate of the extent of renormalisation of the magnetic susceptibility due to inter-dimer coupling. The value of g in different orientations measured by ESR (performed by S. Zvyagin & J. Krzystek, NHMFL Tallahassee [35]) are shown in Fig. 5.2. Values obtained are g_a = 2.230, g_b = 2.060 and g_c = 2.130 $\pm$ 0.004 in good agreement with values obtained from susceptibility fits within the uncertainty of these measurements, indicating that any inter-dimer terms are not large enough to have a measurable effect at low fields.

An additional confirmation of the value of J in this system is obtained from heat capacity measurements. The Schottky anomaly from the large spin gap is too small to be easily resolved

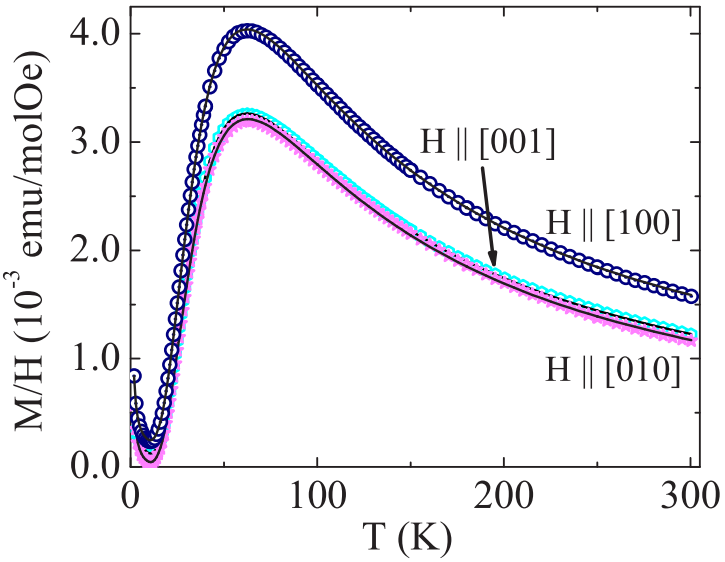

Figure 5.1. Temperature dependence of the magnetic susceptibility of a single crystal of $Sr_2Cu(BO_3)_2$ for a field of 5000 Oe aligned along the principal crystal axes. Solid lines show fit to isolated-dimer model, described in main text.

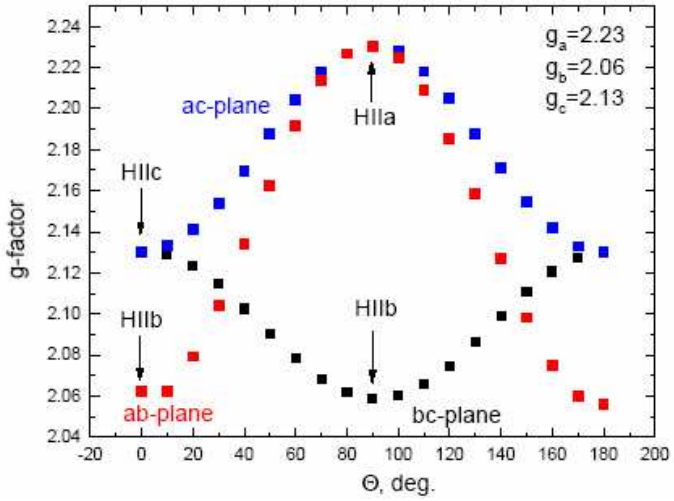

Figure 5.2. $Sr_2Cu(BO_3)_2$: Values of g obtained by S. Zvyagin & J. Krzystek by Electron Spin Resonance (ESR) using a Bruker Elexsys E680X spectrometer at X-band frequency 9.38 GHz at room temperature

against the large phonon contribution to the heat capacity. However, the shift in heat capacity due to Zeeman splitting of the triplet states in a magnetic field can be observed. Measurements were made in zero field and 18 T continuous magnetic field on a single crystal of $Sr_2Cu(BO_3)_2$ weighing 7.9 mg. The field was oriented at an arbitrary angle to the crystal. The difference between these two values, ΔC_p = C_p (18 T) - C_p (0 T) is due solely to changes in the magnetic contribution and can be calculated for an isolated-dimer model using measured values for J and g for this crystal. Fig. 5.3 shows calculated and measured values for ΔC_p as a function of temperature. The measured data has a broad maximum with a peak value of 0.38 ± 0.07 J/molK centered at 14 ± 1 K, compared to the model which has a peak value of 0.32 J/molK centered at 16 K. The difference between calculated and measured values at higher temperatures is likely from the decreased accuracy of the resistive thermometer due to the magnetoresistive effect in high magnetic fields. Within this experimental uncertainty, the data agree, confirming the estimate of J = 8.6 meV.

Additional features are evident in the heat capacity at high temperatures (inset to Fig. 5.3), which appear to be unrelated to the low temperature magnetic properties. Structural refinements performed on a single crystal (by Y. Mozharivskyj and G. Miller, Iowa State University [32]) indicate no change in symmetry or average atomic positions between the Low Temperature (LT) (T < 230 K), Room Temperature (RT) (230 K < T < 320 K), and High Temperature (HT) (T > 320 K) regions, but a marked change in the thermal parameters of the B atoms indicates a change in vibrational properties.

5.2 Pulsed high magnetic fields: an estimate of J', J''

In order to access the ordered magnetic state, a high external magnetic field is necessary, at which $g\mu_B H$ is of the order of J, since the inter-dimer coupling is very weak. The effects of

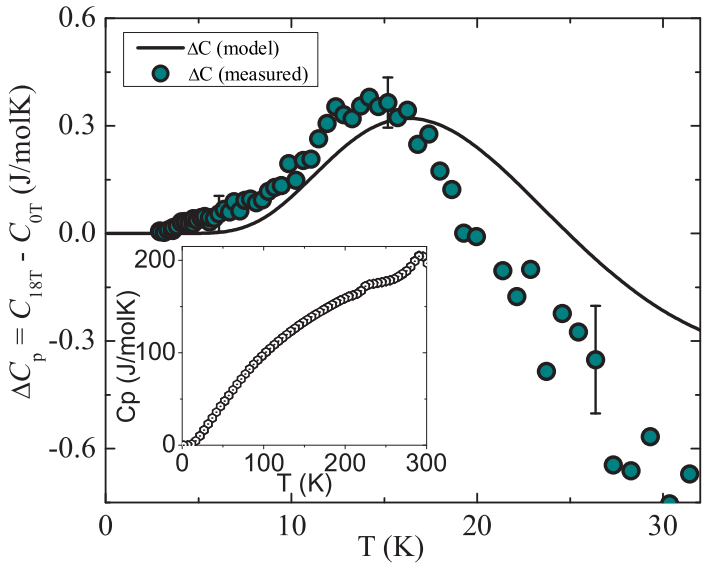

Figure 5.3. Difference in heat capacity ΔC_p = C_p (18 T) - C_p (0 T) for a single crystal of $Sr_2Cu(BO_3)_2$. Solid line shows calculated value for the isolated-dimer model with J = 8.6 meV and g = 2.14. Inset shows total heat capacity in zero field between 2 K and 300 K. Mol refers to the formula unit.

inter-dimer coupling become apparent at these high magnetic fields. In the following discussion, the experimentally measured magnetisation at high magnetic fields is presented, and the deviation from the isolated-dimer model related to the inter-dimer exchange coupling.

Results of high field magnetisation measurements are shown in Fig. 5.4 for single crystals in different orientations and for a composite of randomly oriented single crystal fragments. A feature of the isolated-dimer model is a sharp increase in magnetisation to 1 μ_B when the lowest Zeeman-split triplet state crosses the singlet state at T = 0 K. Fig. 5.4 shows the magnetisation of a single crystal of $Sr_2Cu(BO_3)_2$ as a function of magnetic field applied along each of the principal axes. Each single crystal used for these measurements was shaped into the form of a cylinder (so as to maximise the volume fraction in pulsed magnetic field measurements),

with the cylindrical axis coinciding with one of the principal crystalline axes. Measurements were performed with the magnetic field oriented along the axis of the cylinder shaped samples. The dotted line is a model magnetisation curve for isolated dimers at $T = 1.5$ K for $J = 8.6$ meV and measured values of g for each orientation. For the composite sample, g is taken to be 2.23, corresponding to a fragment oriented with magnetic field along the a-axis for which H_{c1} is lowest. The upturn in the model isolated-dimer magnetisation is at magnetic field $H = \frac{J}{g\mu_B}$ = 66 T (71 T) for g = 2.23 (2.06) corresponding to the magnetic field applied along the a (b) crystalline orientation, as indicated by the dotted lines in Fig. 5.4. The magnetic field at which the measured magnetisation begins to rise is clearly seen to be lower than the isolated-dimer value. This is due to weak inter-dimer coupling, which causes triplet dispersion, thereby broadening the triplet band, and lowering the actual field H_{c1} at which the triplet band crosses the singlet state. The size of the spin gap $\Delta = H_{c1} g\mu_B$ is estimated from the measured value of H_{c1}. From Fig. 5.4, it can be seen that since the magnetisation at the onset of the transition is very low, the signal to noise ratio is not large enough to reliably extract H_{c1} from the foot of the transition. Instead, H_{c1} is extracted from a linear extrapolation of the magnetisation at higher fields at which $M > 0.05\,\mu_B$ (and the signal to noise ratio sufficiently large), down to $M = 0$, from which $H = H_{c1}$ is obtained. The linear extrapolation used to obtain H_{c1} is shown in Fig. 5.4. The value of H_{c1} is determined to be 55, 62, 59 $\pm$ 2 T along the a, b, and c principal axes respectively, which on scaling by the value of g along each of those directions, yield a consistent estimate of the size of the spin gap in $Sr_2Cu(BO_3)_2$ within experimental uncertainty: $\Delta = H_{c1} g\mu_B$ = 7.2 $\pm$ 0.2 meV.

The amount by which the spin gap is reduced from the isolated-dimer case then has the value 1.4 $\pm$ 0.2 meV. The equivalent magnetic model for $Sr_2Cu(BO_3)_2$ resembles a square lattice of in-plane dimers linked by J' and J'' (as shown in Fig. 2.4 on page 12). This is equivalent to a single layer of the representative lattice shown in Fig. 2.9 where the interlayer

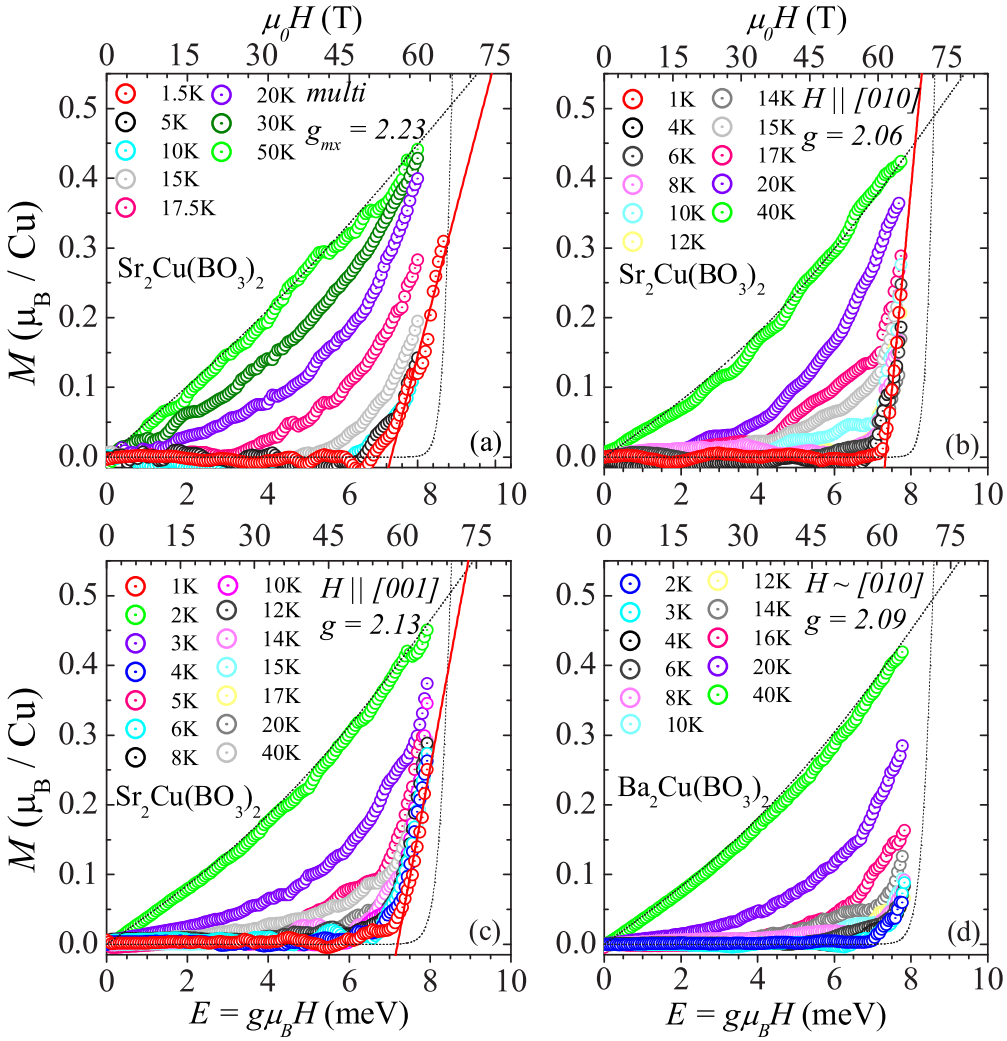

Figure 5.4. $Sr_2Cu(BO_3)_2$: Magnetisation as a function of applied magnetic field measured at different temperatures (a) on a collection of six randomly oriented fragments from a single crystal. g is taken to be the maximum value, since the lowest upturn in magnetisation occurs at this value of g. (b) on a single crystal with magnetic field applied close to the crystalline b-axis. (c) on a single crystal with magnetic field applied close to the crystalline c-axis. (d) $Ba_2Cu(BO_3)_2$: Magnetisation as a function of applied magnetic field on a single crystal oriented close to the c-axis with g-value = 2.09. Calculated values for isolated-dimer model with J = 8.6 meV and measured values of g at $T \sim 1$ K and 40 K are shown by dashed lines. The solid red lines in (a), (b) and (c) are a linear extrapolation of the magnetisation at 1 K above M = 0.05 μ_B down to 0 in order to determine H_{c1}. The $\mu_0 H$ axis varies from one orientation to the other because of the difference in g-factor, however $E = g\mu_B H$ (meV) is a normalised quantity which facilitates direct comparison between different orientations.

coupling $J_\perp$ is negligibly small, and $J_{||}$ is represented by the average $\frac{J' + J''}{2}$ in the absence of additional information on the relative values of J' and J'. The perturbative result obtained in Eqn. 2.11 gives a first estimate of $\frac{J' + J''}{2} = J - g\mu_B H_c \simeq 1.4 \pm 0.2$ meV.

5.2.1 Dzyaloshinkii-Moriya interactions

The effect of an anisotropic interaction such as a Dzyaloshinskii-Moriya (DM) interaction would be to mix singlet and triplet states, and therefore preclude a sharp transition at H_{c1}.

A DM interaction can arise from inequivalent dimer sites, leading to a lack of inversion symmetry of the spin dimer. This interaction can be represented as a term in the Hamiltonian:

$$\sum_{\langle i,j \rangle} (-1)^i \mathbf{D} \cdot (\mathbf{s_i} \times \mathbf{s_j}) \tag{5.4}$$

In the presence of a magnetic field, the DM interaction generates an effective staggered field. For computational simplicity, we consider the case where the DM term is in the z-direction, and the magnetic field H is applied in the x-direction. In this case, the staggered field in the y-direction generated by the DM term is given by:

$$h \sum_j (-1)^j s_j^y \,, \qquad \left(h \propto \frac{D}{J} \right) \tag{5.5}$$

For general directions of the DM term and magnetic field term, the direction of the effective staggered field is $H \times D$. Hence, unless $H \,||\, D$, there is a resulting staggered field which breaks the U(1) rotational symmetry. The staggered field is equivalent to a single spin raising / lowering operator (from Eqn. 5.5) which leads to triplet creation / annihilation, thus resulting in particle non-conservation (i.e. equivalent to U(1) symmetry breaking.) The creation / annihilation of a triplet state (i.e. the transition between a singlet and triplet state) can be detected by the technique of Electron Spin Resonance (esr).

The spin dimers in $Sr_2Cu(BO_3)_2$ comprise two Cu^{2+} ions in different environments. The $Cu(1)^{2+}$ ion in the pair is from an octahedral $Cu(1)O_6$ unit, and the $Cu(2)^{2+}$ ion in the pair is from a square planar $Cu(2)O_4$ unit. Hence the two sites are clearly inequivalent, and the spin dimer lacks a center of inversion symmetry, leading to the existence of DM terms. The direction of D is determined by the crystalline space group of the compound. $Sr_2Cu(BO_3)_2$ crystallises in the Pnma space group, which has mirror planes in the $a-c$ plane, as shown in Fig. 5.5. The Cu(2) = Cu(1) dimers lie along these mirror planes, which following the standard symmetry rules of DM exchange, results in a DM vector that is necessarily perpendicular to the mirror planes (i.e. $D \,||\, b$-axis) [49].

It is difficult to unambiguously determine the slope at the foot of the magnetic transition (H_{c1}) shown in Fig. 5.4, as discussed earlier. It can be seen, however, comparing the high-field magnetisation measured for $Sr_2Cu(BO_3)_2$ in different orientations of magnetic field (Fig. 5.4), that the slope at the onset of magnetisation differs between orientations. The magnetic field along the b-axis gives rise to the sharpest transition, consistent with the expectation that the DM term has minimal or no effect in this orientation, since $\mathbf{D} \,||\, b$-axis. ESR experiments are in progress to directly probe the effect of the DM terms.

5.3 Tuning the spin gap by chemical pressure

The shift in H_{c1} from J gives us an indirect measure of the weak inter-dimer coupling. Another way to probe the effect of these inter-dimer couplings is to tune the size of the coupling and observe the effect on the spin gap. In this section, the effect of replacing Sr^{2+} by Ba^{2+} in $A_2Cu(BO_3)_2$ is studied. The effect of this substitution is to form the spin dimer material $Ba_2Cu(BO_3)_2$, which is equivalent to applying negative pressure and thereby modify the exchange couplings.

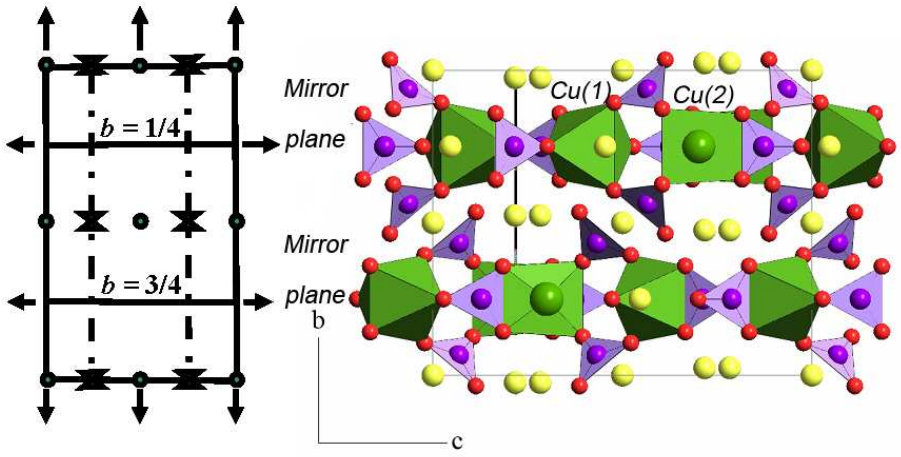

Figure 5.5. Mirror symmetry planes for the Pnma crystal space group compared with the $Sr_2Cu(BO_3)_2$ structure.

As described in Ch. 2, $Ba_2Cu(BO_3)_2$ is isostructural with β-$Sr_2Cu(BO_3)_2$ and crystallises in the same centric group Pnma [17; 34]. The crystal structure comprises $Cu_2B_4O_{12}$ planes separated by Sr (Ba) ions. The substitution of Ba^{2+} (ionic radius 1.35 Å) for Sr^{2+} (ionic radius 1.13 Å) therefore expands the crystal lattice as shown in Table 2.1. The effect of this chemical pressure, as explained later, is to modify the inter-dimer exchange coupling (J', J'') while the intra-dimer coupling (J) is not affected.

As before, low field magnetisation and heat capacity measurements were performed on single crystals of $Ba_2Cu(BO_3)_2$ to estimate the value of J. DC magnetic susceptibility (χ = M/H) in a magnetic field of 5000 Oe measured on the cylindrical crystals of $Ba_2Cu(BO_3)_2$ and $Sr_2Cu(BO_3)_2$ used for high magnetic field measurements are shown in Fig. 5.6 with the magnetic field applied close to the crystalline [010] direction.

Fitting the magnetic susceptibility to Eqn. (5.2), J for both $Ba_2Cu(BO_3)_2$ and $Sr_2Cu(BO_3)_2$ is found to have the value 8.6 $\pm$ 0.05 meV. An additional confirmation of the value of J of $Ba_2Cu(BO_3)_2$ is obtained by measuring the shift in the Schottky anomaly between specific heat in zero field and in an applied magnetic field due to the Zeeman splitting. Fig. 5.7 shows

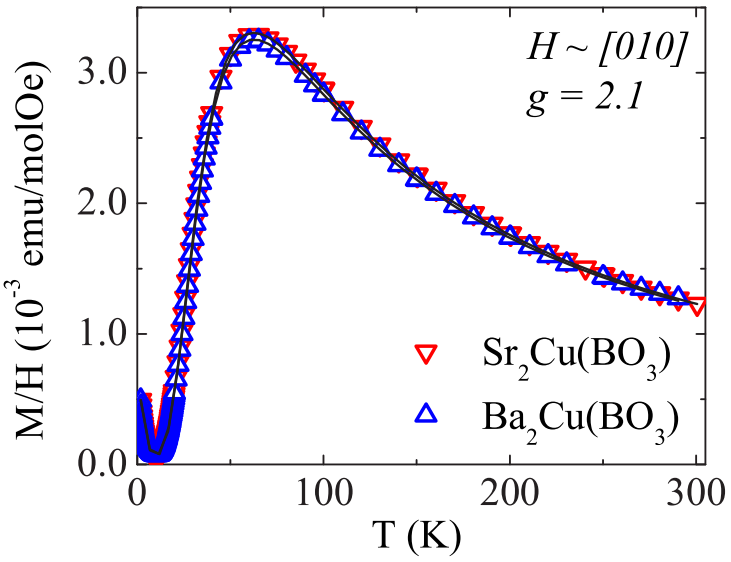

Figure 5.6. Temperature dependence of the magnetic susceptibility of a single crystal of $Ba_2Cu(BO_3)_2$ compared with that of $Sr_2Cu(BO_3)_2$ for an external magnetic field of 5000 Oe applied close to the crystalline b-axis. These single crystals were used for high field measurements detailed subsequently in Fig 5.4. The solid lines show the fit to the isolated-dimer model, described in the main text.

measured values of ΔC_p = C_p (18 T) - C_p (0 T) as a function of temperature compared with calculated values for an isolated-dimer model with J = 8.6 meV and g = 2.09 (measured for this crystal.) The data are in good agreement, confirming the estimate of $J \simeq$ 8.6 meV. It is clear that the strong intra-dimer coupling J remains unaffected with the substitution of Ba^{2+} for Sr^{2+}.

Fig. 5.4 shows the magnetisation as a function of magnetic field applied close to the the [010] direction for $Sr_2Cu(BO_3)_2$ and $Ba_2Cu(BO_3)_2$ respectively. From comparing Fig. 5.4(b) and (d), it is clear that the substitution of Ba^{2+} for Sr^{2+} shifts H_{c1} to a higher value. The region near H_{c1} where the magnetisation shows an upturn is more clearly seen in Fig. 5.8.

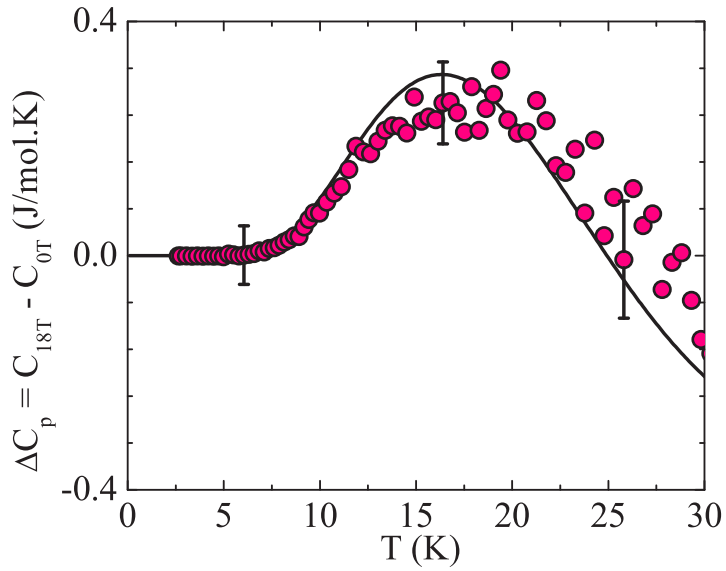

Figure 5.7. $Ba_2Cu(BO_3)_2$: Difference in heat capacity measured on a single crystal in an applied field (in an arbitrary direction) and in zero field ($\triangle C_p = C_p\,(18\,T) - C_p\,(0\,T)$) indicates the shift in Schottky anomaly. The solid line shows the calculated value for the isolated-dimer model with J = 8.6 meV and g = 2.1.

The experimental uncertainty in determining H_{c1} from the foot of the magnetic transition is pronounced in the case of $Ba_2Cu(BO_3)_2$, since the value of H_{c1} is very close to the experimental limit of H = 65 T produced by the pulsed field magnet, and the magnetisation rises to a very small value as compared to the background noise level. Since the magnetisation does not rise to values well above 0.05 μ_B, the same linear extrapolation criteria used to determine H_{c1} in $Sr_2Cu(BO_3)_2$ cannot be used in the case of $Ba_2Cu(BO_3)_2$. Instead, the shift in H_{c1} between $Sr_2Cu(BO_3)_2$ and $Ba_2Cu(BO_3)_2$ is measured by the difference in H corresponding to a small finite magnetisation (0.02 - 0.07 μ_B) between the two compounds. The measured shift of 0.5 $\pm$ 0.1 meV in H (shown in Fig. 5.8) is taken to correspond to the shift in H_{c1} between $Sr_2Cu(BO_3)_2$ and $Ba_2Cu(BO_3)_2$. The value of H_{c1} for $Ba_2Cu(BO_3)_2$ is thereby

inferred to be 7.20(2) + 0.5(1) meV = 7.7(1) meV. Since the value of intra-dimer coupling remains unchanged, as shown by low field measurements, this shift is a result of smaller inter-dimer coupling, leading to an increase in spin gap Δ from 7.2 $\pm$ 0.02 meV in $Sr_2Cu(BO_3)_2$ to 7.7 $\pm$ 0.1 meV in $Ba_2Cu(BO_3)_2$. The decrease in weak inter-dimer coupling in $Ba_2Cu(BO_3)_2$ is directly related to a change in bond lengths due to the substitution of Ba^{2+} for Sr^{2+}, as explained below.

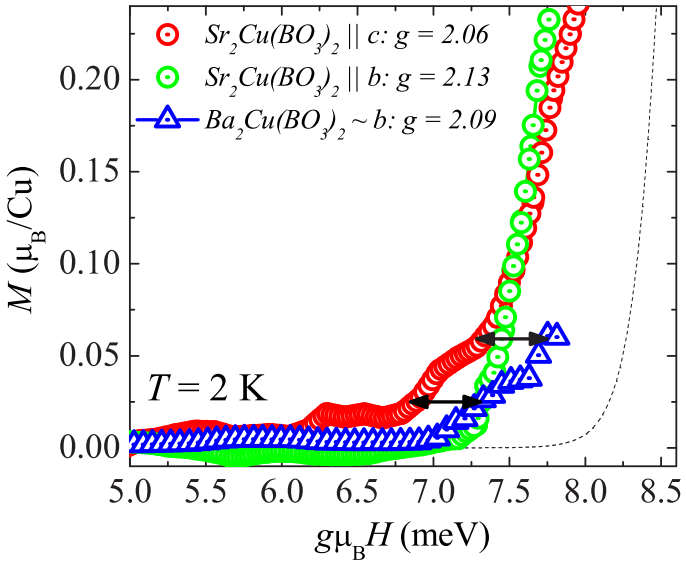

Figure 5.8. Shift in H_{c1} between $Sr_2Cu(BO_3)_2$ and $Ba_2Cu(BO_3)_2$ measured from the difference in applied magnetic field required to produce a magnetisation of 0.02 - 0.07 μ_B.

As discussed in Ch. 2, the $Cu_2B_4O_{12}$ planes of $Sr_2Cu(BO_3)_2$ can be understood in terms of a lattice of weakly coupled, in-plane, anisotropic dimers. Referring to Fig. 2.3, the pronounced difference between the strong inter-dimer coupling J and the weak intra-dimer couplings J' and J'' is due to the distortion of the Cu(1)-O_6 octahedron, with the apical Oxygens O(1) and O(2) situated further from the central Cu(1) ion than the equatorial Oxygens O(3) and O(7).

Within this analysis, strong intra-dimer coupling J is hence related to exchange pathways in the equatorial octahedral plane, whereas the weak inter-dimer couplings J' and J'' are related to exchange pathways in the apical octahedral planes, as represented by the equivalent magnetic lattice shown in Fig. 2.4. The Ba^{2+} substitution distorts the Cu(1)-O_6 octahedron even more than in $Sr_2Cu(BO_3)_2$, as shown in Table 2.1 which lists the relevant bond lengths and the incremental change between the two compounds calculated from structures given in [17; 34]. Within this perturbative analysis, the observed reduction in J' and J'' of Ba relative to Sr can therefore be related to the increased Cu(1)-O(1) and Cu(1)-O(2) bond lengths, and the unchanged intra-dimer coupling J related to the unaltered Cu(1)-O(3) and Cu(1)-O(7) bond lengths. Thus it is apparent from magnetisation measurements that the change in spin gap on substituting Ba^{2+} for Sr^{2+} can be related to a reduction in weak inter-dimer coupling, which in turn can be traced back to changes in specific superexchange pathways in the lattice. This gives us additional confidence in our interpretation of the equivalent magnetic lattice, and the origin of inter-dimer coupling.

5.4 Inelastic neutron scattering on $A_2Cu(BO_3)_2$ (A = Sr, Ba) powder

Direct evidence for the weak inter-dimer coupling, and its change as a result of chemical pressure is obtained by inelastic neutron scattering experiments on $Sr_2Cu(BO_3)_2$ and $Ba_2Cu(BO_3)_2$ that reveal triplon dispersion. Importantly, results of these experiments provide confirmation of the physical origin of the Cu^{2+} dimer in the quasi-two dimensional $A_2Cu(BO_3)_2$ crystal structure.

Fig. 5.9 shows the scattered intensity as a two-dimensional colour plot in momentum-energy transfer space mapped in the range $0 \leq |Q| \leq 6$ Å^{-1}, $4 \leq E \leq 14$ meV for $Sr_2Cu(BO_3)_2$ and $Ba_2Cu(BO_3)_2$ respectively. The maximum in energy intensity in this range reveals a very

narrow magnetic (triplon) excitation, found to be consistent with the antiferromagnetic dimer model. The energy around which the triplon band is centred is a measure of J, and the triplon bandwidth indicates the extent of triplon dispersion due to inter-dimer coupling.

A cut of the measured momentum-energy transfer space integrated over the momentum transfer band $0.5 \leq |Q| \leq 1.5$ Å^{-1} at different temperatures is shown in Fig. 5.10 for $Sr_2Cu(BO_3)_2$ and $Ba_2Cu(BO_3)_2$. The form of the scattering intensity as a function of the energy-transfer is a convolution of the material response, and the instrument resolution. Analysis is currently in progress to deconvolve the effect of the instrumental resolution. A simplified analysis is presented here, where the intensity as a function of the energy-transfer at the lowest measured temperature is fit to a Gaussian (Fig. 5.10). The maximum in intensity centred at 8.7 ± 0.1 meV for both materials reveals magnetic excitations at $J \sim 8.7$ meV as anticipated by the antiferromagnetic dimer model deduced from thermodynamic measurements.

The width of the peak in intensity reveals that the magnetic excitations are in fact dispersive, arising from weak inter-dimer coupling. The structure of the peak reflects the distribution of the density of states within the dispersive band (i.e.) the double-humped peak in intensity clearly seen in the case of $Sr_2Cu(BO_3)_2$ (Fig. 5.10) corresponds to two maxima in the density of states at the top and bottom of the cosine band. Since the peak in intensity in the case of $Ba_2Cu(BO_3)_2$ is narrower than in the case of $Sr_2Cu(BO_3)_2$, the structure of the peak cannot be identified as clearly in this material. The onset of the peak in intensity corresponds to the gap Δ to the dispersive triplet excitations. Additional single crystal INS measurements are currently in progress in order to determine a rigorous model to fit the peak in intensity and thereby extract the value of Δ. A rough estimate of Δ can be obtained by performing a Gaussian fit and considering the onset of the peak as defined as the value at which the intensity is 20 $\%$ of the maximum intensity corresponding to the Gaussian fit. This value is obtained from the Gaussian fit shown in (Fig. 5.10), and is found to be lower in the case of $Sr_2Cu(BO_3)_2$ (7.1 ± 0.2 meV)

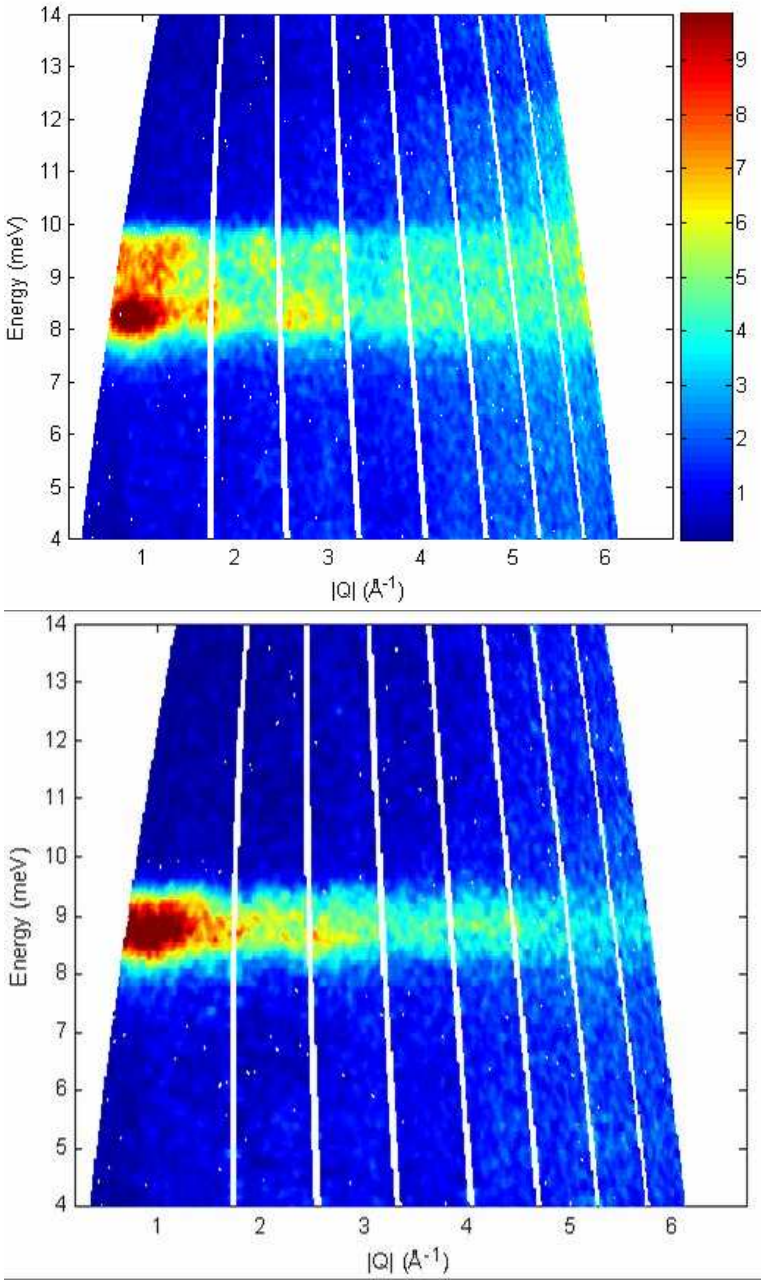

Figure 5.9. Two-dimensional plots showing triplon excitations in momentum-energy transfer space for (a) $Sr_2Cu(BO_3)_2$ and (b) $Ba_2Cu(BO_3)_2$.

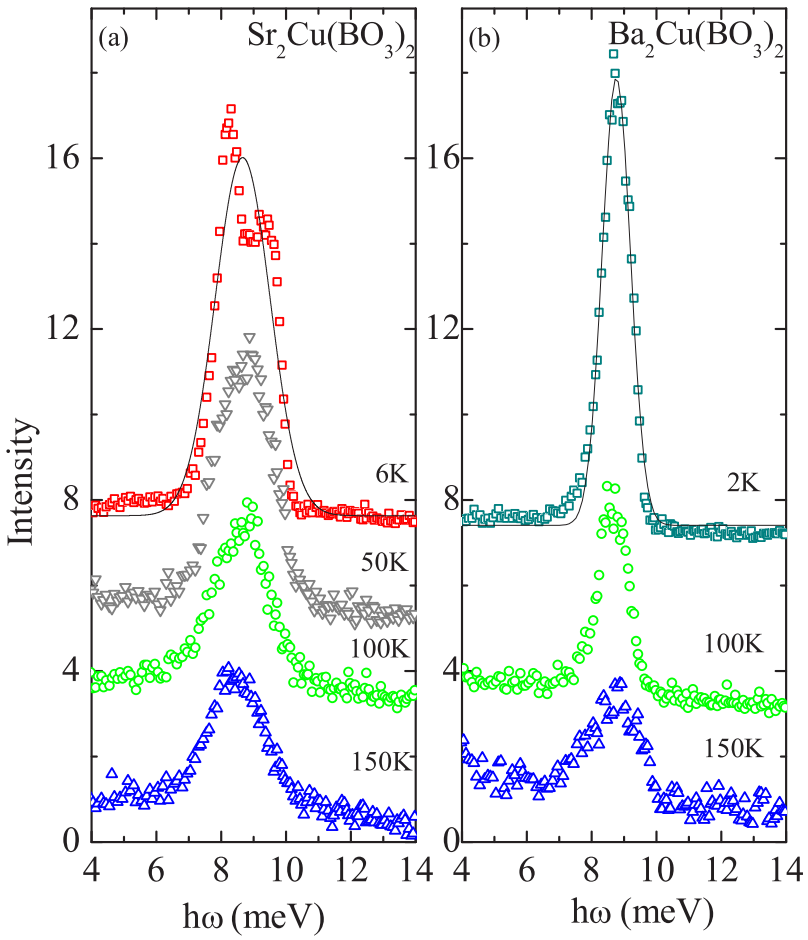

Figure 5.10. Cuts of momentum-energy transfer space in a band $0.5 \leq |Q| \leq 1.5\text{Å}^{-1}$ for (a) $Sr_2Cu(BO_3)_2$ and (b) $Ba_2Cu(BO_3)_2$ respectively. Intensity profiles at different temperatures are offset for clarity. The solid lines are fits to a Gaussian.

than in $Ba_2Cu(BO_3)_2$ (7.9 ± 0.2 meV); consistent within experimental uncertainty (taking into account that the experimental resolution has not yet been deconvolved) with the values previously obtained from measurements of H_{c1} from magnetisation measurements. This provides compelling evidence that the substitution of the larger ion Ba^{2+} for Sr^{2+} in $Sr_2Cu(BO_3)_2$ leads to an increase in spin gap due to a reduction in the triplon bandwidth. In terms of the perturbative expansion of the weakly coupled dimer model (discussed in Chapter 2), the sum of weak inter-dimer coupling J' + J'' corresponds to the bandwidth of triplet dispersion. This is obtained from the Gaussian peak width (defined here, as described above, at 20 $\%$ of the peak amplitude), and has the value 3.0 $\pm$ 0.2 meV for $Sr_2Cu(BO_3)_2$ and 1.6 $\pm$ 0.2 meV for $Ba_2Cu(BO_3)_2$, consistent within experimental uncertainty with results of magnetisation measurements.

Inelastic neutron scattering is an ideal technique to unambiguously determine which pair of Cu^{2+} ions constitute the spin dimers, since it enables a direct measure of the form factor. A cut in momentum-energy transfer space was made by integrating across the entire energy band for both $Sr_2Cu(BO_3)_2$ and $Ba_2Cu(BO_3)_2$ (Fig. 5.11). The powder average I(Q,E) over the neutron scattering structure factor S(**Q**,E) for an isolated-dimer structure is given by [37].

$$I(Q,E) \propto \mid F(Q) \mid^2 (1 - \frac{\sin QD}{QD})\delta(E - E_{gap}) \tag{5.6}$$

where D is the separation between the ions in the dimer. The momentum transfer dependence of the intensity in the excited energy band shown in Fig. 5.11 clearly reveals oscillatory behaviour, corresponding to scattering from a dimer (Eqn. 5.6). The solid line in the figure is a least squares fit to Eqn. 5.6, utilising the Freman-Watson form factor $\mid F(Q) \mid$ for Cu^{2+} [38; 39]. This fit yields a Cu^{2+} ion pair separation D of 4.23 $\pm$ 0.08 Å in $Sr_2Cu(BO_3)_2$ and 4.22 $\pm$ 0.08 Å in $Ba_2Cu(BO_3)_2$. This is consistent with the exchange path from Cu(1) to Cu(2)

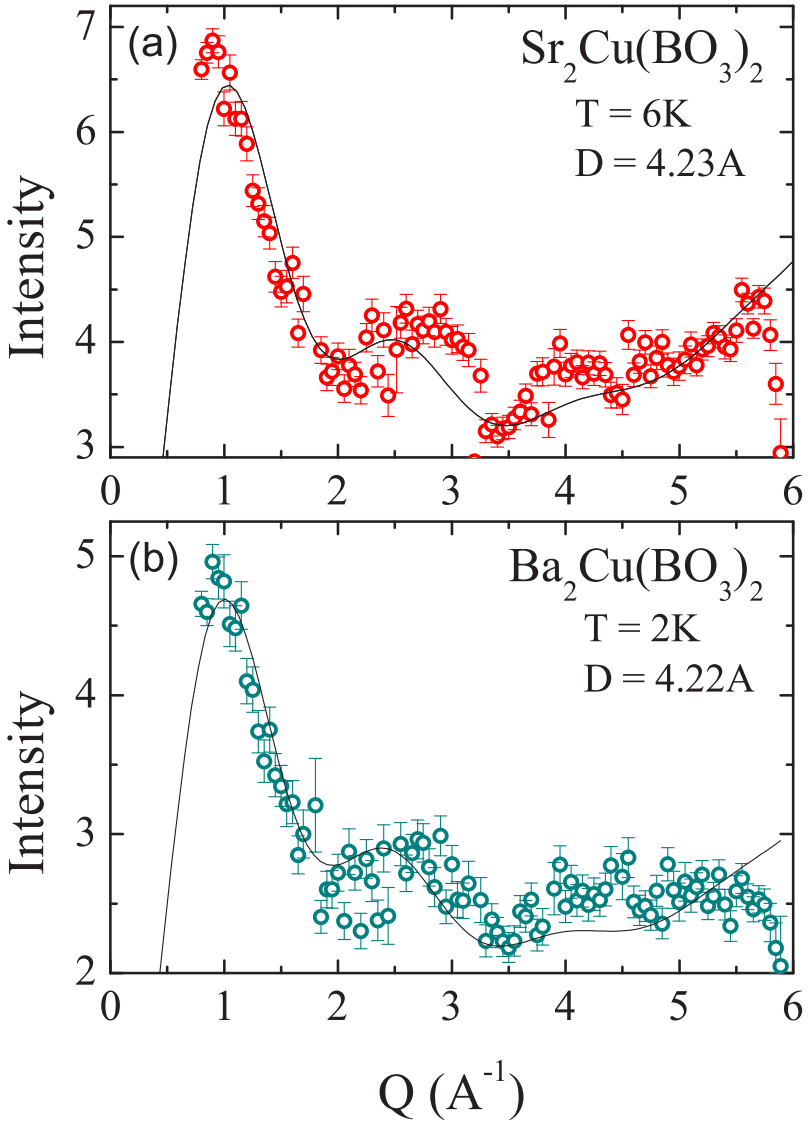

Figure 5.11. Integrated intensity over the entire energy band as a function of momentum transfer for (a)$Sr_2Cu(BO_3)_2$ and (b)$Ba_2Cu(BO_3)_2$. The solid line is a fit to the isolated antiferromagnetic dimer structure factor in Eqn. 5.6. The oscillatory features of the isolated-dimer model are reproduced by the measured data, and the inter-ion separation (D) within each dimer is extracted from the fit to the data. At lower values of momentum transfer below 1Å^{-1}, the data resolution is limited by the experimental setup, due to a limit on the minimum distance to the detector bank.

through the equatorial Oxygens O(6) and O(7) shown in Fig. 2.3 and Table 2.1, corresponding to Cu^{2+} ion separation 4.27 Å in $Sr_2Cu(BO_3)_2$ and 4.36 Å in $Ba_2Cu(BO_3)_2$. This value differs significantly from the exchange pathways through the apical Oxygens, of length 6.13 (6.35) Å and 5.28 (5.5) Å for A = Sr (Ba), corresponding to exchange couplings J' and J'' respectively. These results definitively indicate the physical origin of the Cu^{2+} dimer in the $A_2Cu(BO_3)_2$ crystal structure.

At $T \neq 0$, the energy-transfer cross section for a two-level system is scaled by the thermal population factor for the ground state [36]:

$$\frac{d^2\sigma}{d\Omega\, dE'}(T) \quad = \quad \frac{1}{1+ne^{-\Delta/k_BT}}\frac{d^2\sigma}{d\Omega\, dE'}(0) \tag{5.7}$$

where n is the degeneracy of the excited state (n = 3 for an AF dimer). From the energy-transfer cross sections shown at different temperatures in Fig. 5.10, the integrated intensity is seen to reduce with temperature, largely consistent with the temperature dependence expected for the antiferromagnetic dimer model in Eqn. 5.7. From Fig. 5.10, the triplon band is observed to narrow with an increase in temperature. This thermal renormalisation arises from the obstruction of inter-dimer triplet hopping by the exclusion condition when the concentration of thermally excited triplets becomes significant. A quantitative theoretical prediction of this thermal renormalisation can be found in Ref. [40], and has been empirically observed in the spin-dimer system $TlCuCl_3$ [41].

Results of inelastic neutron scattering experiments on powders of $A_2Cu(BO_3)_2$ provide conclusive evidence that the equivalent magnetic lattice comprises weakly-coupled antiferromagnetic dimers with strong intra-dimer exchange coupling J = 8.7 $\pm$ 0.05 meV. The physical origin of the Cu^{2+} dimers is unambiguously confirmed to be through the superexchange pathway between Cu(1) and Cu(2) through the equatorial Oxygens O(6) and O(7). The spin gap is

directly measured as 7.1 ± 0.2 meV in $Sr_2Cu(BO_3)_2$, and is found to increase to 7.9 ± 0.2 meV in $Ba_2Cu(BO_3)_2$ as a result of the substitution of Ba^{2+} for Sr^{2+}, thereby reducing the bandwidth of triplet dispersion from 3.0 $\pm$ 0.2 meV to 1.6 $\pm$ 0.2 meV.

5.5 Nature of the magnetically ordered state

In the preceding sections, magnetisation and INS measurements were discussed that confirm the description of $A_2Cu(BO_3)_2$ as a spin dimer system comprising a network of weakly connected dimers. The size of the spin gap has been measured, the magnitude of the inter-dimer exchange terms estimated, and the equivalent magnetic lattice description confirmed.

To conclude the discussion of $A_2Cu(BO_3)_2$, we turn to the nature of the magnetically ordered state above H_{c1}. Theoretical predictions [4; 5] indicate that the ordered state of a weakly interacting dimer system without frustration or significant symmetry breaking terms may be described as a Bose Einstein condensate of triplons (elementary triplet excitations), resulting in staggered, transverse magnetic order. The equivalent magnetic lattice (shown in Fig. 2.4) that describes the $Sr_2Cu(BO_3)_2$ system is exactly of this nature (in the case that Dzyaloshinkii Moriya terms are small enough to be neglected or the magnetic field is aligned along the direction of the DM-vector), suggesting that the ordered state of $Sr_2Cu(BO_3)_2$ at magnetic fields above the spin gap may be described by a BEC of triplons.

Fig. 5.12 shows the magnetisation measured on $A_2Cu(BO_3)_2$ as a function of temperature at a representative high magnetic field ($H > H_{c1}$) equivalent to an energy of 7.19 meV (i.e. 62 T in the [010] direction of $Sr_2Cu(BO_3)$, 64 T in the [001] direction of $Sr_2Cu(BO_3)$, and 63 T near the [010] direction of $Ba_2Cu(BO_3)$). The finite magnetisation of $Sr_2Cu(BO_3)_2$ at low temperatures in high magnetic fields is indicative of a field-induced magnetically ordered state, which may be interpreted as Bose Einstein condensation of triplons. In contrast, the inter-dimer coupling in $Ba_2Cu(BO_3)_2$ is too small for the system to order at an energy of

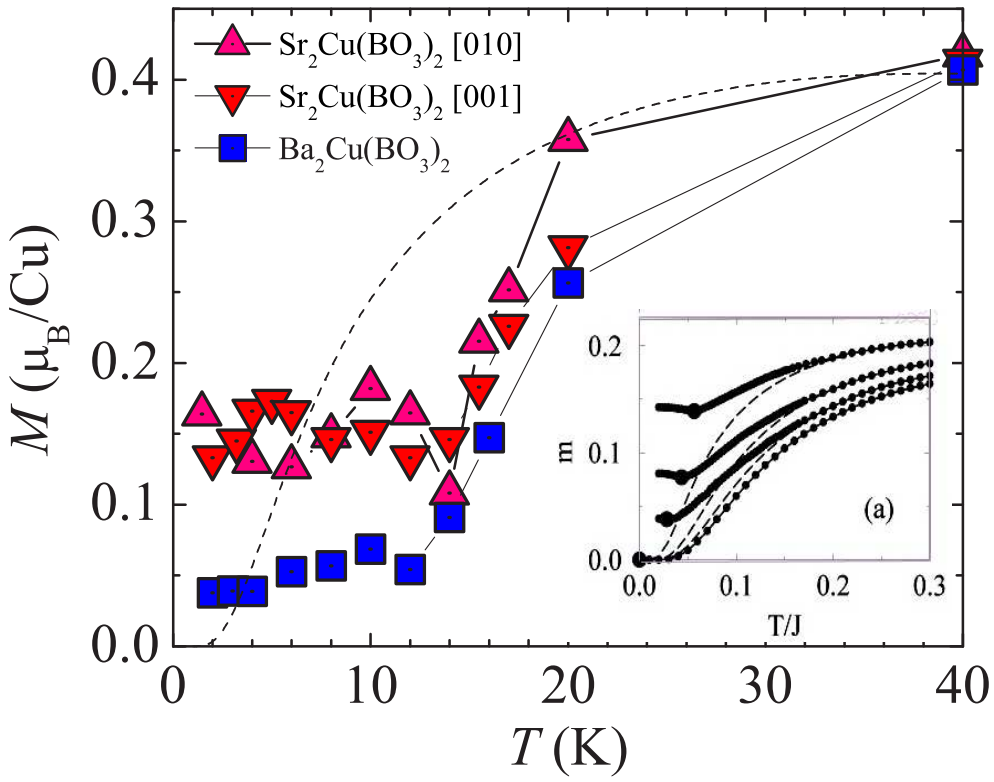

Figure 5.12. Magnetization of $A_2Cu(BO_3)_2$ (A = Sr, Ba) as a function of temperature for different directions of applied magnetic field equivalent to an energy of 7.19 meV. The magnetisation shown is for a magnetic field of 62 T applied in the [010] direction (g_b = 2.13) on $Sr_2Cu(BO_3)_2$, a magnetic field of 64 T (= 62 $\times$ $\frac{2.13}{2.06}$) applied in the [001] direction (g_c = 2.06) on $Sr_2Cu(BO_3)$, and a magnetic field of 63 T (= 62 $\times$ $\frac{2.13}{2.09}$) applied close to the [010] direction (g_c = 2.09) on $Ba_2Cu(BO_3)$. The dashed line represents the magnetisation calculated for an isolated-dimer model for J = 8.6 meV, g = 2.13. The inset (from ref. [42]) shows the temperature dependence of the uniform magnetisation in the representative lattice discussed in Chapter 2. The coupling anisotropy is $J_\perp/J_{||}$ = 1/15, and the magnetic fields are h/J = 0.80, 0.86, 0.90, 0.97. Extrema in $M(T)$ indicate the onset of $3d$ ordering, and are denoted by enlarged filled circles.

7.19 meV. The slight dip in magnetisation occurring at temperature $T_c \sim 14$ K for an energy of 7.19 meV (shown in Fig. 5.12) for $Sr_2Cu(BO_3)_2$ possibly indicates the onset of magnetic field induced ordering (following a similar temperature dependence of results from numerical studies of weakly coupled dimer systems [42] shown in the inset to Fig. 5.12). However, only a small portion of the phase diagram is accessible due to the large value of the spin gap, and it is therefore difficult to unambiguously identify the nature of the ground state in high magnetic fields for this material.

Chapter 6

Experimental study of a BEC QCP in $BaCuSi_2O_6$

"Life is uncertain. Eat dessert first." - Ernestine Ulmer

The spin dimer compound $BaCuSi_2O_6$ has certain advantages which make it a better model system to study than $A_2Cu(BO_3)_2$. The size of the intra-dimer coupling $J \simeq 4.5$ meV [12; 21; 43] is smaller than in $A_2Cu(BO_3)_2$, resulting in a more experimentally accessible spin gap. Further, the spins are arranged on a square bilayered lattice, such that exchange interactions are rotationally invariant around the crystalline c-axis, indicating that the spin Hamiltonian representing the equivalent magnetic lattice is U(1) symmetric. Further evidence for U(1) symmetry is seen from the experimental results. This is an important prerequisite for Bose-Einstein condensation, enabling us to draw a better analogy between the magnetically ordered state and a Bose-Einstein condensate of triplets.

In the case of $BaCuSi_2O_6$, published work [21; 43] has already established the equivalent magnetic lattice and estimated the size of the spin gap as well as the intra-dimer and inter-dimer exchange couplings. Hence in this chapter, experimental results of my research that measure the exchange couplings are only briefly discussed. Instead, extensive discussion focusses on the

more significant results of my research that probe the field-tuned QCP separating the ordered from the disordered state. The magnetic phase transition in $BaCuSi_2O_6$ was experimentally measured by a series of torque, heat capacity, magnetisation, and magnetocaloric effect experiments at low temperatures and high magnetic fields ($H > H_{c1}$) to map out the ordering phase boundary. Power laws were extracted from the low temperature region describing the approach toward the QCP and compared with theory, which as discussed in Chapter 2, predicts mean field critical exponents characteristic of the $3d$ BEC universality class.

6.1 Low magnetic fields: an estimate of J

The dominant intra-dimer exchange interaction (J) coupling the two Cu^{2+} $s = 1/2$ spins within a dimer is estimated from low field measurements just as in $A_2Cu(BO_3)_2$. From the exponential behaviour of the susceptibility at low temperatures, the material is identified as a spin dimer system. The value J is estimated by fitting to Eqn. (5.2), and found to be 4.40 $\pm$ 0.02 meV for both magnetic field applied in the [001] direction, and perpendicular to the [001] direction in agreement with published data [44]. The value for g is found to be 2.31 $\pm$ 0.05 for H aligned along the crystalline c-axis, and 2.01 $\pm$ 0.05 for H aligned perpendicular to the crystalline c-axis. $R \sim 0.001$ emuK/mol Oe, corresponding to $\sim 0.3\%$ impurity concentration, assuming impurity spins with g = 2, $s = \frac{1}{2}$.

An independent measure of the value of g in different orientations was obtained from ESR measurements carried out by R. McDonald, NHMFL, Los Alamos [45]. Values obtained are $g_c = 2.31$, $g_{ab} = 2.03$ in good agreement with values obtained from susceptibility fits within the uncertainty of these measurements, and with previous published data [21; 43].

Just as in the $A_2Cu(BO_3)_2$ system, an additional confirmation of the value of J for $BaCuSi_2O_6$ is obtained from heat capacity measurements. In this case, however, the Schottky anomaly from

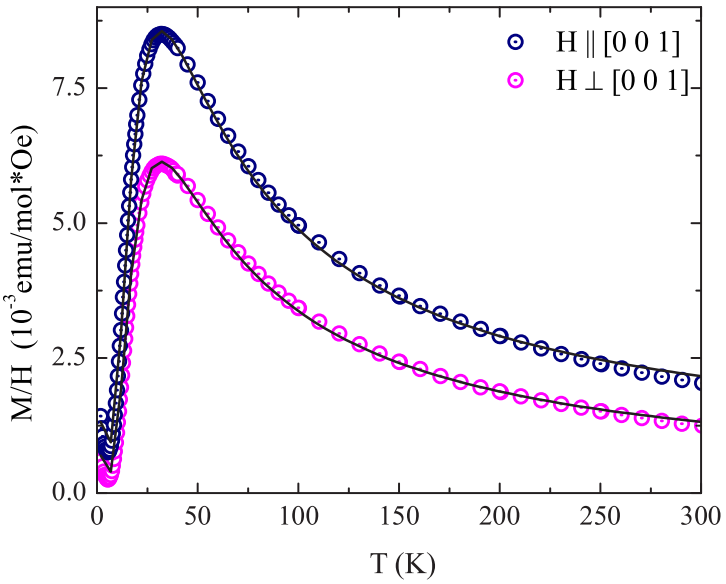

Figure 6.1. Temperature dependence of the magnetic susceptibility of a single crystal of $BaCuSi_2O_6$ for a field of 5000 Oe aligned along the principal crystal axes. Solid lines show fit to isolated-dimer model, described in main text.

the spin gap can be directly observed, since the feature is centred at moderately low temperatures, where the phonon background is not too large. The phonon contribution is obtained as a third order polynomial (inset to Fig. 6.2) added to the magnetic contribution using an isolated-dimer model with intra-dimer coupling J = 4.40 meV to fit the total specific heat. Since the phonon contribution is extrapolated from relatively high temperatures, it is not a particularly accurate estimate. Nevertheless, it is consistent with a magnetic contribution which clearly reveals a Schottky anomaly consistent with an isolated-dimer model with intra-dimer coupling J = 4.40 meV (Fig. 6.2). The solid line represents the calculated value for ΔC_p as a function of temperature using the isolated-dimer model with J = 4.40 meV. A polynomial contribution has been subtracted from the total heat capacity in zero magnetic field to obtain an estimate of the magnetic heat capacity. The decreased accuracy of the resistive thermometer due to the

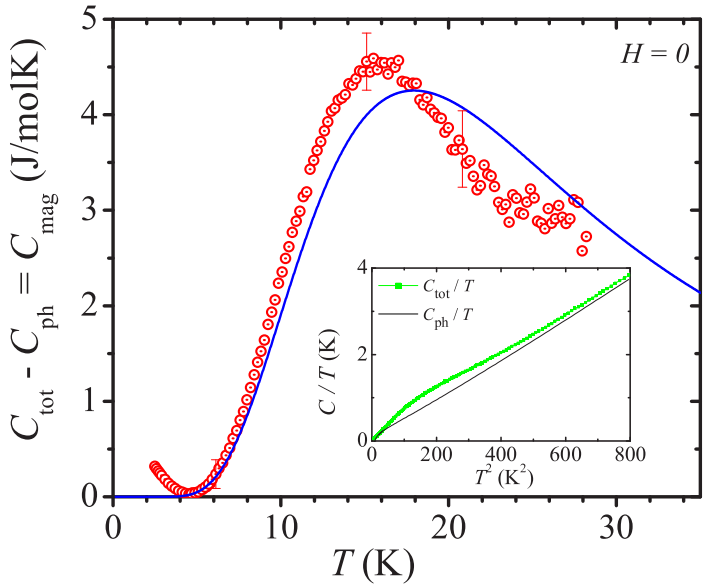

Figure 6.2. $BaCuSi_2O_6$: Schottky anomaly in magnetic heat capacity measured in zero magnetic field. The solid line shows the calculated value for the isolated-dimer model with J = 4.4 meV. The inset shows the measured total heat capacity, and the polynomial approximation made to the phonon heat capacity: $C_{ph} = 5.5 \times 10^{-3}\,T^3 - 3.7 \times 10^{-2}\,T^2 + 0.46\,T - 1.20$, which is subtracted to obtain the magnetic heat capacity.

magnetoresistive effect in high magnetic fields contributes to the difference between calculated and measured values at higher temperatures. Additional differences between the measured data and the simple isolated-dimer model arise due to inter-dimer coupling. Within this uncertainty, the data agree, confirming the estimate of J = 4.40 $\pm$ 0.02 meV from magnetic susceptibility.

6.2 Direct confirmation of U(1) symmetry

A prerequisite for BEC is that rotational U(1) symmetry is not explicitly broken. Thus, there is no preferred orientation in the XY plane - it is only when the system orders as a BEC that

a preferred orientation is selected, and U(1) symmetry spontaneously broken. The equivalent magnetic lattice used to represent $BaCuSi_2O_6$ comprises exchange interactions which are rotationally invariant around the crystalline c-axis, indicating that there are no anisotropic terms that explicitly break U(1) symmetry in the spin Hamiltonian. Empirical observations strengthen the evidence that such terms in the Hamiltonian are either non-existent or small enough to be negligible (i.e. measured values of the critical exponent ν are consistent with theoretically predicted BEC values, implying the absence of significant anisotropic terms.) However, it is important to obtain an independent measurement of the size of any symmetry-breaking terms that may be present in the Hamiltonian in order to verify our assumption.

6.2.1 Nature of anisotropic terms

Recent structural analysis of $BaCuSi_2O_6$ has revealed a weak orthorhombic structural transition at approximately 100 K (the observed feature in magnetisation is shown in Fig. 6.3), accompanied by an incommensurate lattice modulation [46]. The low temperature spin Hamiltonian is therefore likely to be more complex than the representation in Eqn. 2.10. The orthorhombic distortion implies that the x and y components of the in-plane coupling J' are no longer equal. Further, the incommensurate structural modulation indicates a potential inequivalence of Cu^{2+} sites, resulting in more than one value of intra-dimer coupling J [47]. The increased complexity of the magnetic lattice is significant, since anisotropic exchange interaction terms in the spin Hamiltonian are no longer forbidden by symmetry arguments. In the more general spin Hamiltonian, the bilinear spin term $\mathbf{s}_i \cdot \mathbf{s}_j \equiv \mathbf{s}_i \boldsymbol{I} \mathbf{s}_j$ in Eqn. 2.10 is replaced by the general exchange interaction $\sum_{i,j=1}^{3} \mathbf{s}_i \cdot \overleftrightarrow{T}_{i,j} \mathbf{s}_j$, where $\overleftrightarrow{T}_{i,j}$ can be separated into a scalar T_s, an antisymmetric tensor $\overleftrightarrow{T}_{as} = \sum \frac{1}{2}(T_{ij} - T_{ji})(\mathbf{e_i} \times \mathbf{e_j})$, and a traceless symmetric tensor $\overleftrightarrow{T}_{sm} = \frac{1}{2}(T_{ij} + T_{ji})_{i \neq j}$. Terms $\overleftrightarrow{T}_{as}$ and $\overleftrightarrow{T}_{sm}$ mix spin components, leading to spin non-conserving (anisotropic) terms. These anisotropic interactions have been calculated by

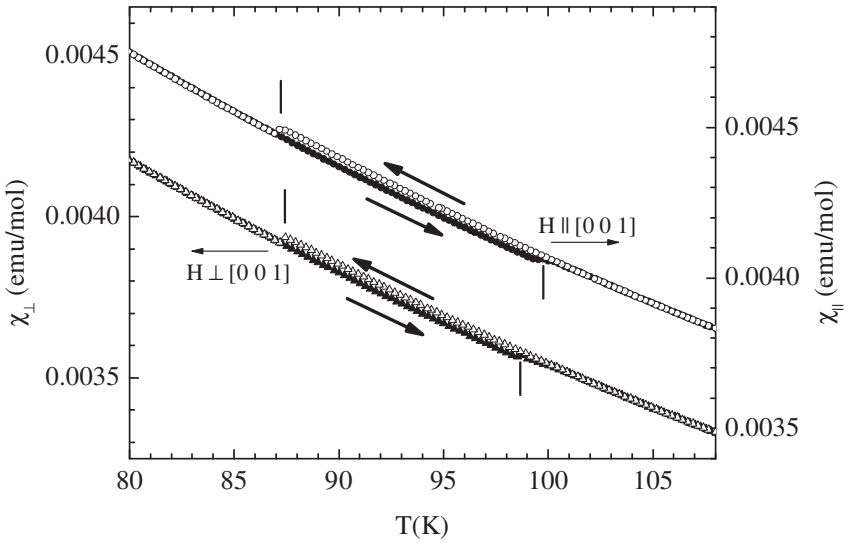

Figure 6.3. Temperature dependence of the susceptibility of $BaCuSi_2O_6$ between 80 and 110 K, for an applied field of 5000 Oe oriented parallel and perpendicular to the crystalline c axis (circles and triangles respectively). Data are shown for warming (solid symbols) and cooling cycles (open symbols), indicated by arrows. Jumps in susceptibility associated with the first order phase transition are indicated by vertical lines. Differences in the cooling rate result in the difference in the lower temperature jump for the two data sets.

Dyaloshinkii and Moriya [48] by perturbatively including the effect of the Hubbard interaction V and spin-orbit coupling $(\hbar/2m^2c^2)[\nabla\ V\ \times\ \nabla]\cdot\mathbf{s}$ in the superexchange interaction. The resulting anisotropic components have the form $\overleftrightarrow{T}_{as} = \mathbf{D}\cdot[\mathbf{s}_i\times\mathbf{s}_j]$ and $\overleftrightarrow{T}_{sm} = \mathbf{s}_i\ \overleftrightarrow{\Gamma}\ \mathbf{s}_j$. $\mathbf{D}$ is linear in the spin-orbit coupling constant, and $\overleftrightarrow{\Gamma}$ is quadratic in the spin-orbit coupling constant [48].

From standard symmetry rules [49], the room temperature I41/acd orthorhombic crystalline space group restricts the direction of $\mathbf{D}$ to the axis of four-fold symmetry (c-axis), and requires that $\overleftrightarrow{\Gamma}$ is zero. The weak orthorhombic distortion at low temperatures, however, lifts both of these restrictions. It is therefore crucial to experimentally determine the origin, size and nature

of any such anisotropic terms in order to determine the energy scale of any U(1) symmetry breaking that may arise.

6.2.2 High frequency electron spin resonance (ESR)

Electron Spin Resonance (ESR) involves optical absorption that corresponds to transitions between spin states in a magnetic field. High microwave frequencies in the presence of an applied magnetic field are used to drive inter-(intra-)multiplet transitions, which are probed by ESR. For an $s = \frac{1}{2}$ system, the energy levels corresponding to the isotropic Hamiltonian are a groundstate singlet, and three degenerate triplet excited states, separated from the groundstate by an energy gap of Δ ($\equiv g\mu_B H_{c1}$). A magnetic field results in Zeeman splitting of the triplet energy levels in linear fashion. The resulting intra-triplet transitions in a finite magnetic field can be directly probed by ESR. The presence of anisotropic terms in the spin Hamiltonian would result in the mixing of spin components, thereby lifting the triplet degeneracy in zero magnetic field due to a shift in individual triplet levels. Experimentally measurable signatures of these anisotropic terms would be intra-triplet transitions in zero magnetic field and non-unique dependence of the intra-triplet transition frequency on the magnetic field. The schematic in Fig. 6.4 shows examples of possible ESR transitions in the presence of anisotropic terms.

6.2.3 Experimentally observed anisotropic terms

Results from ESR measurements performed by S. Hill *et al.* at the University of Florida [50] are shown in Figs. 6.5 & 6.6. Experiments were performed for a range of frequencies between 26 GHz and 52 GHz in low magnetic fields. While at high temperatures a single narrow peak in intensity is observed corresponding to the transition between the $s_z = 0$ and $s_z = \pm 1$ triplet levels in the absence of anisotropic terms, distinct shoulders are seen to split from the

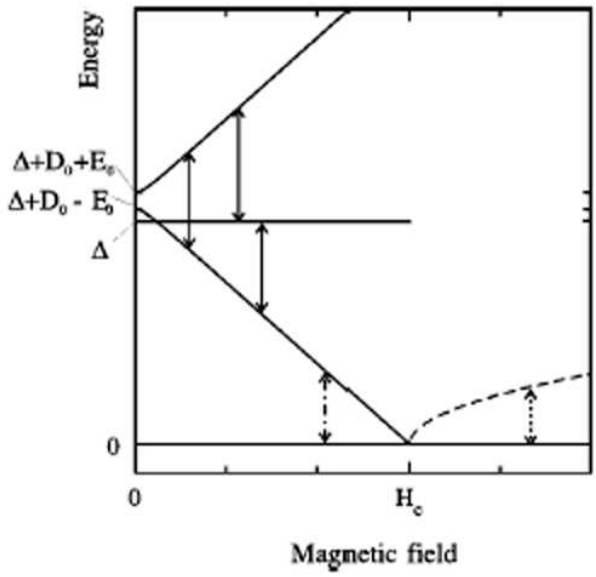

Figure 6.4. Scheme of the energy levels of a spin-dimer system in a magnetic field $H \parallel z$ in the presence of the orthorhombic anisotropy. Arrows show possible ESR transitions for k = 0: intra-triplet (solid), singlet-triplet (dash-dotted), transition above H_c (dotted). It is to be noted that the singlet-triplet transitions are only allowed in the presence of anisotropic interactions. Figure from Ref. [76]

central peak at low temperatures (Fig. 6.5). In addition, hyperfine splitting is observed at low temperatures, presumably associated with unpaired Cu^{2+} impurity spins. Identical shoulders on either side of the central peak have been observed in Ref. [51]. In Ref. [51], Zvyagin *et al.* fit the angular dependence of the shoulders to obtain an anisotropic parameter of size 0.1 K. A more direct measure of the anisotropic parameter is an experimental determination of the zero-field splitting of triplet levels by extrapolating the frequency dependence as a function of magnetic field. The experimentally determined frequency dependence as a function of magnetic field is shown in Fig. 6.6. By extrapolating to zero magnetic field, the magnitude of the shoulder splitting on either side of the central peak is obtained to be 1.8(3) GHz (0.09 K) and 2.1(1) GHz (0.1 K), in agreement with the value of anisotropic parameter obtained in Ref. [51].

The value $\sim$ 0.1 K of the anisotropic parameter is consistent with an intra-dimer dipole-

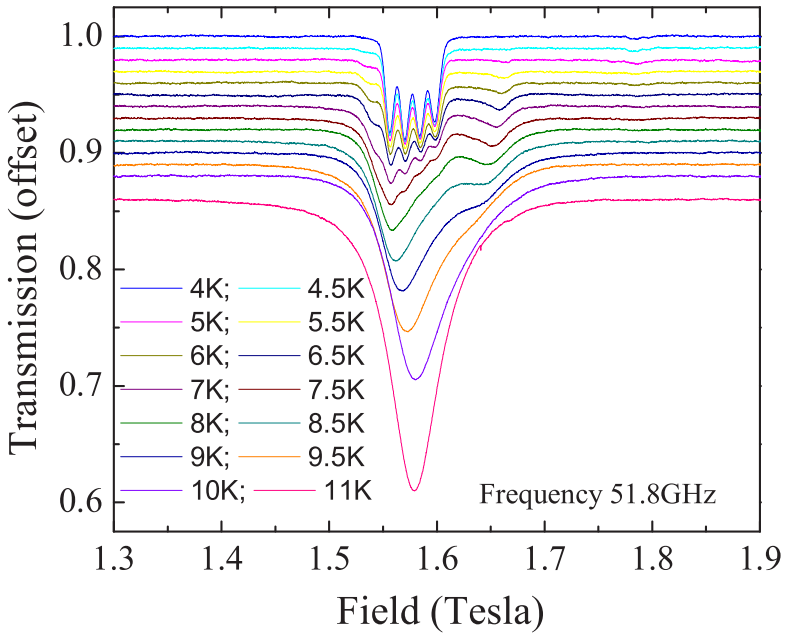

Figure 6.5. $BaCuSi_2O_6$: Splitting of shoulders from the central ESR peak traced with reduction in temperature. Hyperfine splitting corresponding to unpaired Cu^{2+} spins is observed at low temperatures. Experiments were performed by S. Hill *et al.* [50].

dipole interaction with a spin separation distance of 2.7 Å. In addition, we can explain the increased splitting of the shoulders with reduced temperature due to decreased exchange between the triplets, resulting in a decreased spin-flip averaging (i.e. dipolar field fluctuation), the effect of which is to average out the shoulder splitting. Further evidence that the peak splitting observed in ESR experiments has its origin in dipole-sipole interactions is obtained from the absence of a singlet-triplet transition at high magnetic fields, indicating the absence of an asymmetric anisotropy (i.e. a finite term $\mathbf{D}$ linear in spin-orbit coupling in the Hamiltonian). The dipole-dipole interaction is a form of symmetric anisotropy (i.e. a finite term $\overleftrightarrow{\Gamma}$ appears in the Hamiltonian), and does not break U(1) symmetry when it points along the intra-dimer (i.e.

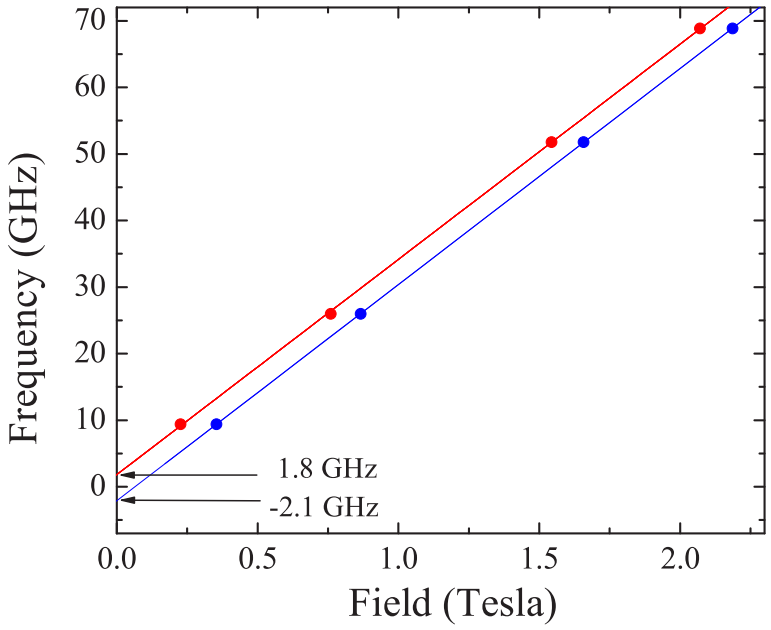

Figure 6.6. $BaCuSi_2O_6$: Zero field splitting of triplet energy levels. The field dependence of the frequencies at which shoulders occur in the ESR spectrum is extrapolated down to zero field to determine the size of the anisotropic term in the Hamiltonian. Experiments were performed by S. Hill *et al.* [50] at the University of Florida, and R. McDonald at NHMFL, Los Alamos [45].

c-axis) direction. Any U(1) symmetry breaking will arise from the inter-dimer dipole-dipole interaction directed in the ab-plane, and is expected to be extremely small ($\sim$ 5 mK) due to the large inter-dimer distance of 7 Å. Hence ESR measurements indicate that the U(1) symmetry of the effective Hamiltonian is preserved down to an energy scale of the order of $\sim$5 mK, as corroborated by the experimentally measured BEC critical scaling exponents down to 30 mK described in the following sections.

6.3 Magnetic ordering at high magnetic fields

6.3.1 Uniform magnetisation: an estimate of H_{c1}, J'

High field magnetisation data (shown in Fig. 6.7) show the upturn in magnetisation expected at H_{c1} (when the lowest Zeeman-split triplet state intersects the singlet state) followed by a linear increase in magnetisation (due to finite triplet population.) Since H_{c1} is given by $\frac{\Delta}{g\mu_B}$, the value of H_{c1} scales with the value of g in each orientation. Linear extrapolation of the magnetisation measured with magnetic field applied along the crystalline c-axis and perpendicular to the c-axis gives a consistent value of spin gap $\Delta = g\mu_B H_{c1}$ = 3.14 $\pm$ 0.05 meV.

The equivalent magnetic model for $BaCuSi_2O_6$ comprises layers of vertical dimers arranged on a square lattice linked by J' and J'' (as shown in Fig.2.7 on page 15). This is equivalent to the representative lattice shown in Fig. 2.9 on page 20 where the inter-layer coupling $J_\perp$ is J'' in this case, and $J_{||}$ is given by $2J'$. Since each CuO_4 square planar unit on a layer is coupled to the neighbouring unit by two superexchange pathways (Fig. 2.5), each vertical dimer is also coupled by two J' exchange pathways to the neighbouring vertical dimer in $BaCuSi_2O_6$. Neglecting J'', the perturbative result obtained in Eqn. 2.11 gives a first estimate of $2J' = J - g\mu_B H_c \simeq 1.26 \pm 0.05$ meV. $BaCuSi_2O_6$ is thus a model spin dimer system to study, since in addition to an experimentally accessible value of spin gap, the ratio of inter-dimer to intra-dimer coupling has a very small value $\sim 10\%$, placing the system unambiguously in the weakly coupled dimer limit. Thus, the model described in Chapter 2 is an accurate description of $BaCuSi_2O_6$, and indeed the particle-hole symmetry described by the Hamiltonian in Eqns. 2.3 - 2.5 is observed in the experimentally determined phase diagram of $BaCuSi_2O_6$, which will be described in the next section.

A better estimate of J' and the inter-layer coupling J'' is obtained by applying Monte Carlo simulation techniques to reproduce the experimentally obtained phase boundary mapping the

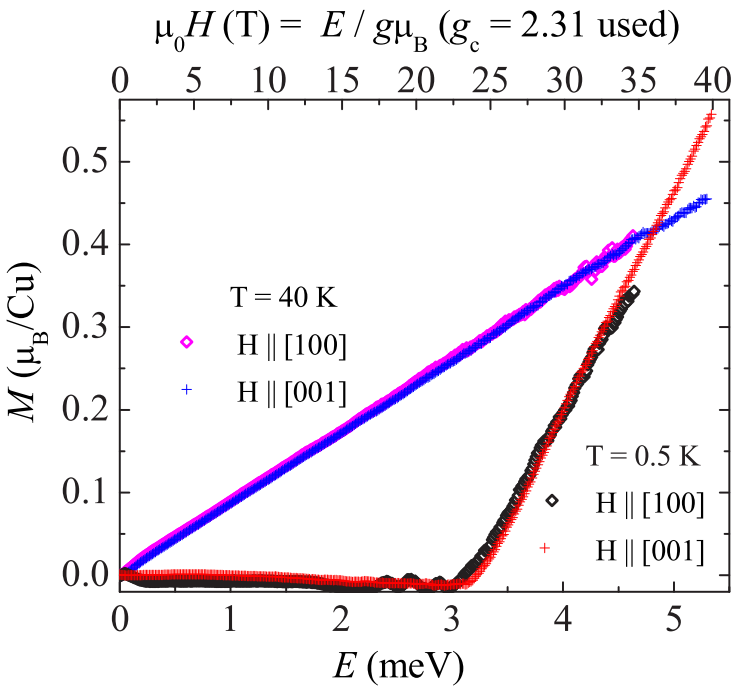

Figure 6.7. $BaCuSi_2O_6$: Magnetisation as a function of magnetic field up to 40 T applied along the crystalline c-axis and a-axis. The applied magnetic field along the crystalline a- and c-axis (g_a = 2.05, g_c = 2.31) is represented as an equivalent energy $E = g\mu_B H$ meV on the lower x-axis, such that measurements in both orientations share the same axis. The upper x-axis specifically shows the applied magnetic field H along the c-axis.

ordering temperature as a function of the proximity to the QCP.

6.3.2 Ordering phase boundary

Magnetic torque, magnetocaloric effect and specific heat experiments (described in Chapter 3) were performed at different values of temperature and magnetic field, to obtain points on the phase boundary separating the ordered from the disordered state. Features in these thermodynamic quantities characterise the classical $3d$ XY phase transition into the ordered state at finite temperatures.

6.3.2.1 Specific Heat

Specific heat was measured as a function of temperature in a magnetic field of 36 T. Fig. 6.8 shows the characteristic lambda anomaly observed in specific heat, indicating a second order phase transition into the ordered state. The shape is identical to previously published data (on image-furnace grown crystals of $BaCuSi_2O_6$) in [43], which has been fit using directed-loop Monte Carlo simulations and found to correspond with the dilute Bose gas model (shown in the inset to Fig. 6.8). The ordering temperature at 36 T is identified as the peak of the lambda anomaly, and plotted on the phase diagram in Fig. 6.12.

6.3.2.2 Torque magnetisation

Torque was measured as a function of magnetic field up to 33 T in two sets of experiments: measurements between 30 mK and 1 K were performed in a ^{3}He/^{4}He dilution fridge, and measurements between 0.6 K and 3.3 K were performed in a ^{3}He fridge. Measurements were performed with H inclined at a small ($<10^\circ$) angle to the crystalline c-axis in order to obtain a finite torque, from which the uniform magnetisation (M) and hence the particle density (ρ) is extracted. Sample torque curves from measurements in a ^{3}He fridge and dilution fridge are shown in Fig. 6.9a and in Fig. 6.9b respectively. The absolute value of magnetisation was obtained by comparison with magnetisation data taken in pulsed fields (Fig. 6.7) and calibrated against a MPMS magnetometer (Fig. 6.1). The width of the field-range over which the transition occurs is influenced by experimental factors such as the stiffness of the cantilever convolved with the material response. However, the field at which the phase transition occurs can be accurately obtained from the position of a sharp feature in the second derivative of the torque (an example is shown in Fig. 6.9c). The feature in the second derivative sharpens as the temperature is reduced, approaching a divergence as $T \rightarrow 0$ (shown in Fig. 6.10). This method of extracting the ordering transition is significantly more accurate and reliable than

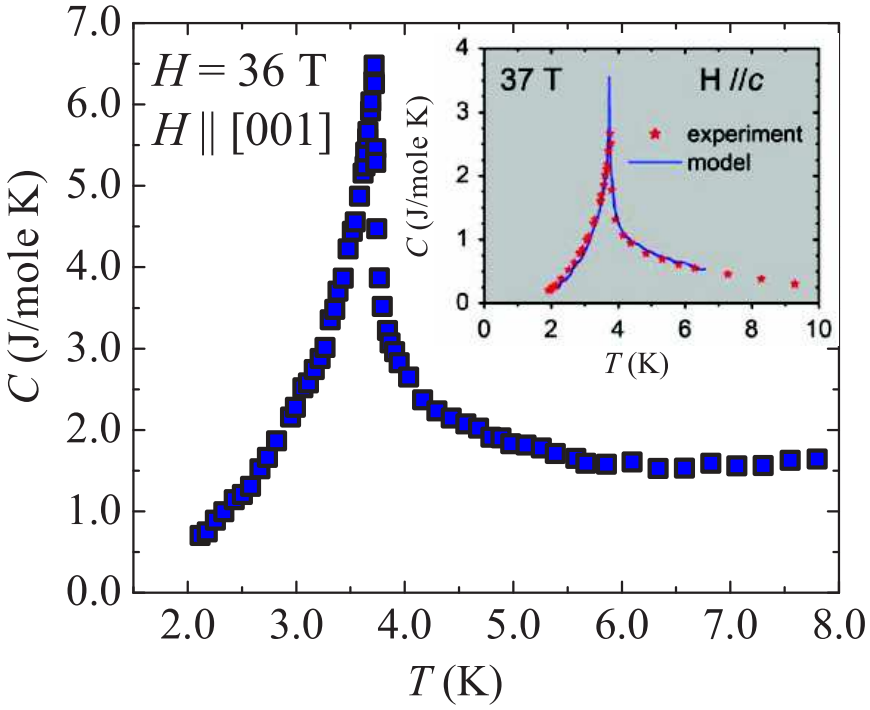

Figure 6.8. $BaCuSi_2O_6$: Specific heat measured at a magnetic field of 36 T, showing a lambda anomaly. The inset shows data from Ref. [43] where a similar lambda anomaly has been fit by a Monte Carlo simulation. Experiments reported as part of this dissertation were performed on cleaner flux-grown crystals with better experimental resolution, and hence show a sharper lambda anomaly.

methods used in similar work on other related compounds [5; 44; 55; 56; 57] as we see from the following thermodynamic argument.

The non-analytic behaviour of the free energy $F(T, H)$ is dominated by a single relevant exponent. Hence, the singular behaviour of $F(T, H)$ when T and H are close to a critical point on the line $T_c(H)$ does not depend on the direction $u(H - H_c\ ,\ T - T_c)$ of approach to the critical point, as long as it is not tangent to the critical line. In particular, we have

$$\partial^2 F/\partial^2 u \;=\; C \;\propto\; u^{-\alpha} \qquad \text{for} \quad u \;=\; T \;-\; T_{\mathrm{c}} \tag{6.1}$$

Choosing $u \;=\; H - H_{\mathrm{c}}$, we obtain

$$\partial^2 F/\partial^2 H \;=\; \partial M/\partial H \;\propto\; (H \;-\; H_{\mathrm{c}})^{-\alpha} \tag{6.2}$$

Since $\alpha \;\sim$ -0.015 for a 3D XY-like transition [58], the second derivative of the magnetisation is divergent at the critical point:

$$\partial^2 M/\partial^2 H \;\propto\; (H \;-\; H_{\mathrm{c}})^{-1\,-\,\alpha} \tag{6.3}$$

We thus obtain the ordering transitions (indicated by red circles in the phase diagram plotted in Fig. 6.12) from the feature in the second derivative of the magnetisation. At finite low temperatures, the quantum phase transition is characterised by a sharp feature, which reduces in amplitude due to thermal smearing with an increase in temperature. At higher temperatures, the feature becomes weaker still, as the quantum phase transition crosses over to a thermal phase transition. The ordering transition can be extracted reliably up to $T = 3.3$ K.

6.3.2.3 Magnetocaloric effect

The magnetocaloric effect was measured as a function of magnetic field between 20 T - 45 T at initial temperatures of 2.5 K to 4 K (representative curves shown in Fig. 6.11. The position of the ordering transition from magnetocaloric effect for $H \;<\; H_{\mathrm{max}}$ is obtained from the onset of the peak (as defined by the maximum in the first derivative, shown in the inset to Fig. 6.11) in a rising field and for $H \;>\; H_{\mathrm{max}}$ from the onset of the dip in a falling field (as explained in Ch. 3). The ordering transition thus obtained for a representative field sweep is shown in the inset to Fig. 6.11. Points on the phase diagram obtained from magnetocaloric effect measurements are shown by green circles in the phase diagram plotted in Fig. 6.12.

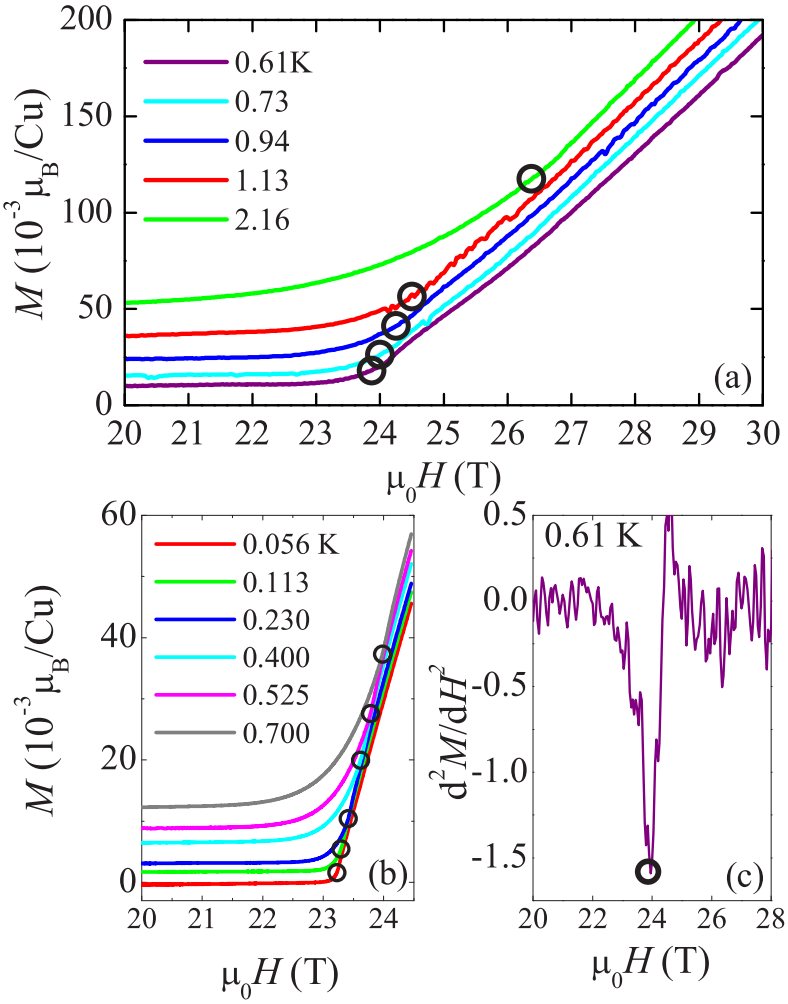

Figure 6.9. $BaCuSi_2O_6$: Torque measured as a function of rising magnetic field at representative temperatures (a) in a ^{3}He fridge (b) in a dilution fridge. The ordering transitions determined from a sharp feature in the second derivative (shown in (c)) are indicated on each of the torque curves.

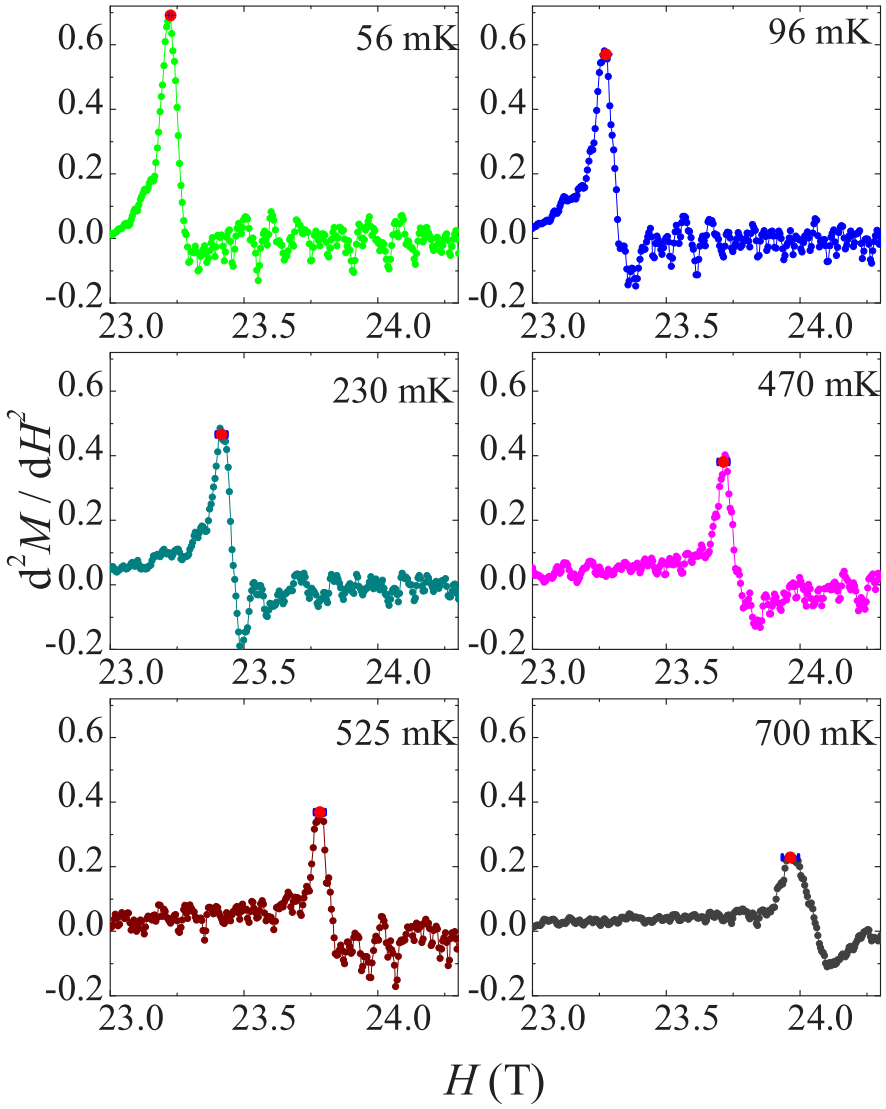

Figure 6.10. $BaCuSi_2O_6$: The second derivative of the uniform magnetisation (extracted from torque measured in a dilution fridge) at various temperatures. The ordering transition is determined from the sharp feature, which is seen to grow with decreasing temperature, approaching divergence at $T = 0$. The peak maximum defines the ordering transition, and the error is defined as the width of the tip of the peak (i.e. 4 - 5 datapoints at a spacing of 0.005 T on either side of the peak maximum.)

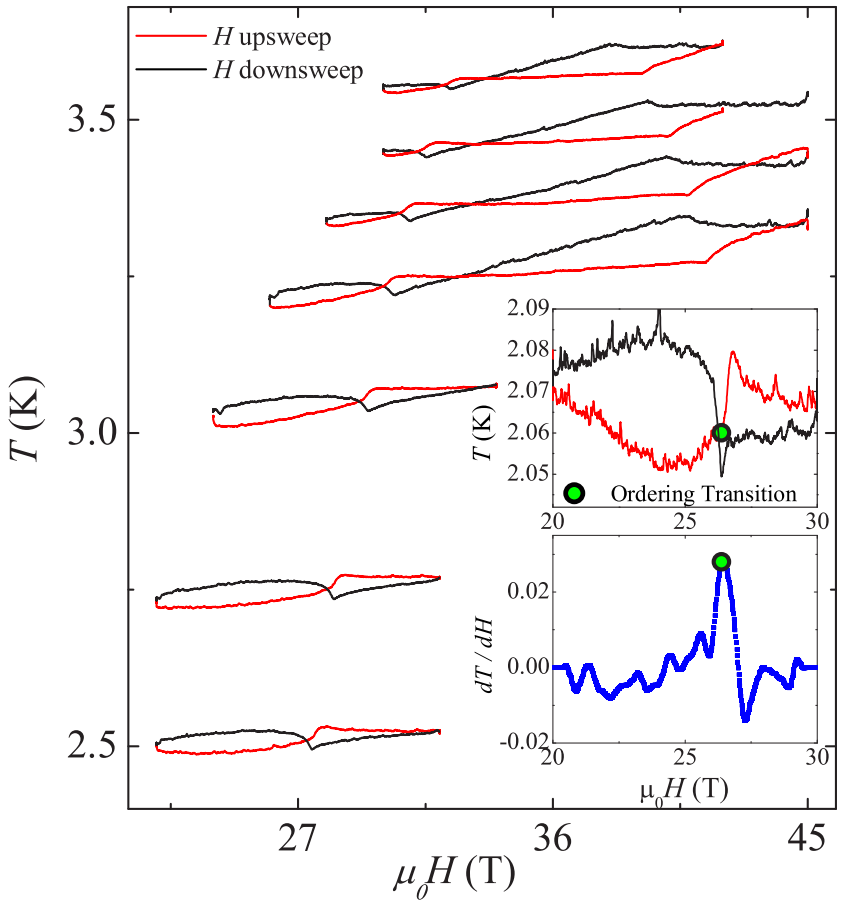

Figure 6.11. $BaCuSi_2O_6$: Representative curves indicating the magnetocaloric effect during up and down magnetic field sweeps. The upper inset shows the ordering transition, defined by the onset of the peak in MCE during the upward magnetic field sweep for an initial set temperature of 2.07 K. The lower inset shows the first derivative dT / dH during the upward magnetic field sweep. The ordering transition is defined as the maximum of the peak, and the error defined as the width at half the maximum height of the peak.

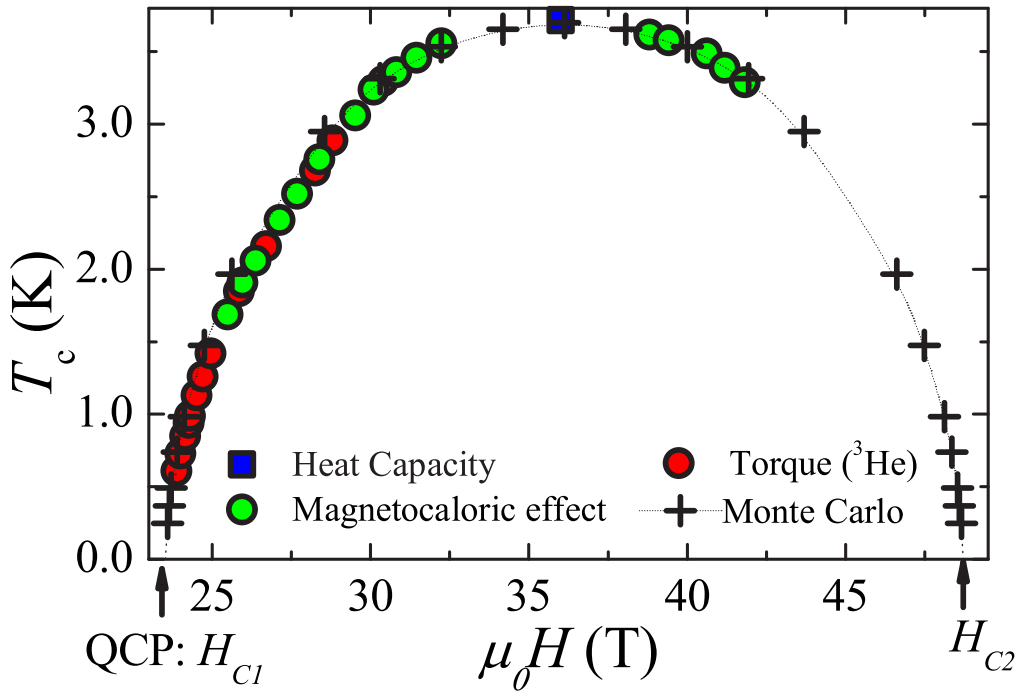

Figure 6.12. $BaCuSi_2O_6$: Experimentally determined phase boundary down to 0.6 K. Points on the phase boundary are determined from magnetic torque (red circles), magnetocaloric effect (green circles), specific heat (blue square) measurements and Monte Carlo simulation (+ symbols, dotted line is a guide to the eye).

6.3.3 $3d$ Bose gas description

From the experimental measurements detailed above, we arrive at a phase boundary of ordering transitions separating the ordered magnetic phase from the disordered phase at finite temperatures (shown in Fig. 6.12). A Monte Carlo simulation of the equivalent magnetic lattice shown in Fig. 2.7 was performed by N. Kawashima, Tokyo University using the directed loop algorithm [59]. Since this lattice can be mapped on to the representative magnetic lattice shown in Fig. 2.9 on page 20, the effective low energy Hamiltonian is given by Eqn. 2.10 on page 22. Fitting the phase boundary down to 0.6 K (the lower temperature phase boundary

will be analysed separately in a later discussion) to the Monte Carlo simulation, the data is fit well by values of J' = 0.51 meV, J'' = 0.168 meV. From the discussion in Chapter 2, it is clear that this Hamiltonian describes a $3d$ gas of hard core bosons with nearest-neighbor hopping and repulsive interactions. The mirror symmetry of the phase diagram in Fig. 6.12 around the maximal point reflects the particle-hole symmetry implicit in the Hamiltonian in Eqns. 2.3 - 2.5. As we describe below, the phase boundary can be interpreted as the ordering transition of a $3d$ interacting Bose gas into an ordered state, which is a Bose Einstein condensate. In other words, the system magnetically orders as an XY antiferromagnet, which may equivalently be interpreted as a BEC of triplets.

6.4 Critical behaviour describing BEC QCP

The $BaCuSi_2O_6$ spin dimer system enables unique field-tuned experimental access to the BEC QCP separating a quantum paramagnet from a BEC of triplets. The magnetic field acts as a chemical potential, which provides a convenient means of changing the particle number, thereby tuning the BEC to criticality at the QCP. In the following section, an analysis is presented in which characteristic power laws are extracted from the experimentally measured phase boundary in the low temperature region near the QCP. As described in Chapter 2, critical exponents for the $d \geq 2$ BEC universality class are mean field, and the power laws are given by

$$T_{\rm c} \propto (H - H_{\rm c1})^{2/d}, \quad \rho(T = 0) \equiv M(T = 0) \propto (H - H_{\rm c1}), \quad M(H_{\rm c1}) \propto T^{d/2}. \tag{6.4}$$

The subsequent discussion is divided into two sections. The first section discusses the subset of experimental results taken in a ^3He refrigerator down to temperatures of 0.6 K. While

this region is at low enough temperatures to be in the universal regime, it presents difficulties in fitting to Eqn. 6.4, because it is not close enough to the QCP to reliably perform a two parameter fit that estimates H_{c1}(0 K) in addition to ν. This is a common experimental limitation in the study of critical power law behaviour. In this section, a new analysis technique is described to reliably extract a critical exponent from a universal region of the phase boundary which is a small distance away from the QCP. H_{c1} is first determined from extrapolating experimental results down to absolute zero temperature, and then a one parameter fit is performed with H_{c1} fixed, to extract ν. The second section discusses the complete dataset of experimental results down to 30 mK. Here, we perform a standard two parameter fit and obtain estimates of ν and H_{c1} in close proximity to the QCP. Values of critical exponents down to 0.6 K extracted in the previous section are confirmed, verifying the validity of the previous analysis technique, and in addition, critical behaviour is studied very close to the QCP, down to 30 mK.

6.4.1 $3d$ BEC quantum critical behaviour for T $\geq$ 0.6 K

The power law from Eqn. 6.4: $T_c \propto (H - H_{c1})^{\nu}$ (where $\nu = 2/d$), can be expressed in reduced form

$$t = f(h) \times (1 - h)^{\nu} \tag{6.5}$$

where $t = \frac{T_c}{T_{max}}$, $h = \frac{H_{max} - H}{H_{max} - H_{c1}}$ (H_{max} and T_{max} represent the point on the phase boundary halfway between H_{c1} and H_{c2}) and $f(h)_{h=1}$ is a finite non-universal quantity determined by the lattice specifics and exchange couplings of the system.

The particle hole symmetry of the phase boundary enables us to extend the region near the QCP in which the power law can be fit. Eqn. 6.5 describes scaling near H_{c1} while $t \propto (1 + h)^{\nu}$ describes scaling near H_{c2}. In other words, the particle-hole symmetry of the system implies

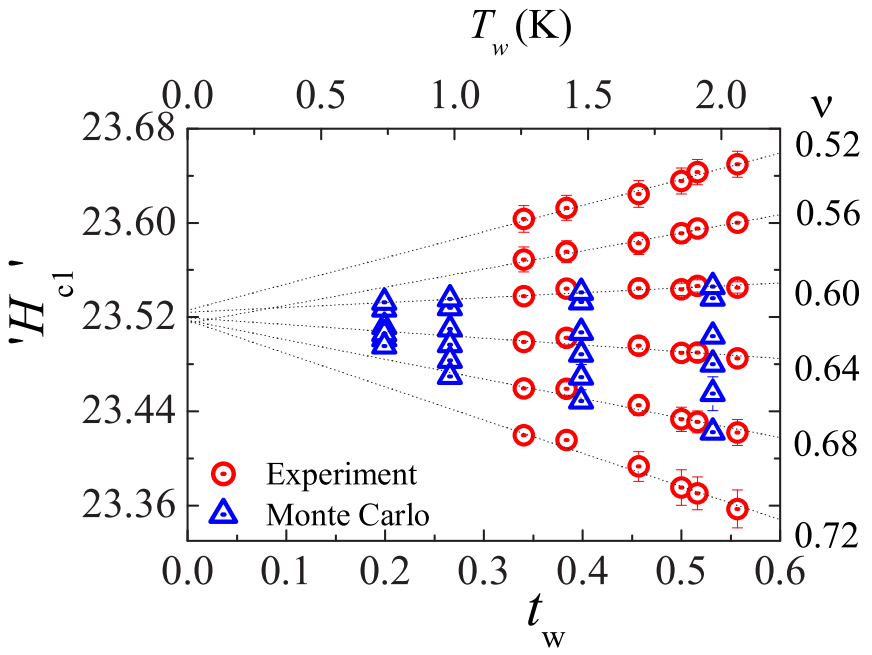

Figure 6.13. $BaCuSi_2O_6$: Estimate of H_{c1} from convergence. The circles represent estimates of 'H_{c1}' obtained from fitting the lowest few (eight or more) experimental points on the phase boundary in Fig. 6.12 in a window of increasing size t_w, to Eqn. 6.6 for different fixed values of ν. The x axis t_w labels the highest reduced temperature (absolute temperature T_w (K)) of the fit window. The dotted lines show the linear convergence of 'H_{c1}' values at $t_w = 0$. The triangles represent estimates of 'H_{c1}' similarly obtained from Monte Carlo simulation data for corresponding fixed values of ν, and similar convergence is observed.

that t is a function of h^2:

$$t = g(h^2) \times [(1 - h)(1 + h)]^{\nu} \equiv g(h^2) \times (1 - h^2)^{\nu} \tag{6.6}$$

where $g(h^2)$ varies more slowly than $f(h)$ in the vicinity of the QCP.

The power law dependence in the quantum critical region is extremely sensitive to both the fit temperature range, and to the estimate of H_{c1} [60]. An empirical convergence approach is used to determine the best estimate of H_{c1}. Fig. 6.13 shows the trend in the estimate of H_{c1}

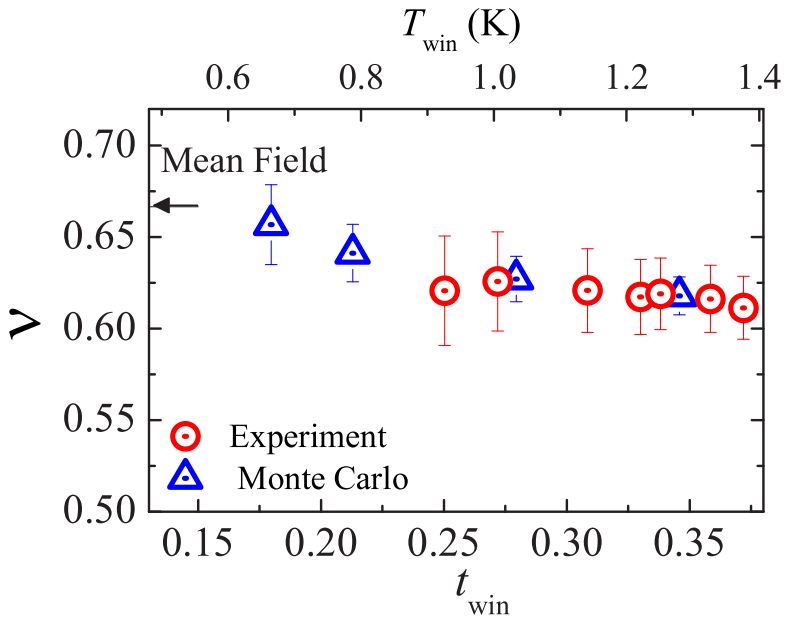

Figure 6.14. $BaCuSi_2O_6$: Estimate of ν in an increasing temperature window. The circles represent estimates of ν from fitting the lowest few (eight or more) experimental points on the phase boundary in Fig. 6.12 in a window of increasing size (the midpoint of the window is labelled by reduced (absolute) temperature $t_{\rm win}(T_{\rm win}\ (K))$, to Eqn. 6.6 with $H_{\rm c1} = 23.52\ T$ determined from Fig. 6.13. The error bars are due to experimental uncertainty in the fit value of $H_{\rm c1}$. The triangles represent estimates of ν from a similar fit to Monte Carlo simulation data.

(denoted as '$H_{\rm c1}$') obtained by fitting the lowest few experimental points on the phase boundary in Fig. 6.12 in a window of increasing size $t_{\rm w}$ to Eqn. 6.6 (where $g(h^2)$ is assumed to be constant to a first approximation) for different fixed values of ν. Near the QCP, it is found from performing a linear extrapolation to $t_{\rm w}$ = 0 that estimates of '$H_{\rm c1}$' become less dependent on ν, and converge to a single value irrespective of the value of ν (Fig. 6.13). Similar convergence to $H_{\rm c1}$ is observed for the Monte Carlo simulation results (Fig. 6.13). The convergence is due to the fact that the QCP is at $H_{\rm c1}$, independent of the path along which it is approached (characterized by ν). From '$H_{\rm c1}$' convergence, we obtain an estimate of $H_{\rm c1} \simeq 23.52$ T.

The uncertainty in this value of H_{c1} is estimated to be 0.03 T, arising from the experimental uncertainty in measuring H_c. The value of H_{c1} = 23.52 $\pm$ 0.03 T thus obtained is then used to estimate the critical exponent ν.

The critical exponent ν is estimated from fitting Eqn. 6.6 (with $g(h^2) \approx$ const.) to the narrowest temperature range near the QCP with a statistically significant number of experimental datapoints. Fig. 6.14 shows the variation in ν with the midpoint of the temperature window that is fit to Eqn. 6.6 (points on the phase boundary are fit from the lowest value of t = 0.16 in increasing window sizes centred at t_{win}.) In the lowest experimentally accessible temperature window down to 0.61 K, the fit value of ν = 0.63 $\pm$ 0.03. Performing a similar analysis for data points from the Monte Carlo simulation reveals the expected increase in ν to the theoretical mean field value as the temperature window is further reduced (Fig. 6.14). The experimental estimate of ν = 0.63 $\pm$0.03 based on measurements down to temperature t = 0.16 (T = 0.61 K) is consistent with the theoretical mean field prediction of ν = 2/3 to within experimental error, as seen on a logarithmic plot in Fig. 6.15 for H_{c1} = 23.52 T. Fig. 6.15 also provides an estimate of the universal region ($T \leq$ 1 K), as indicated by the temperature range in which the Monte Carlo simulation coincides with the value ν = 2/3.

6.4.2 $2d$ BEC quantum critical behaviour for 0.03 K $\leq$ T $\leq$ 0.65 K

Fig. 6.16 shows the entire phase boundary with additional measurements of magnetic torque in a dilution refrigerator down to 30 mK.

Since data are available in close proximity to the QCP, a two-parameter fit is performed with ν, H_{c1} varying. A power law is fit to data in sliding windows of different width (as indicated) centred at T_{win}. Fig. 6.17 shows the evolution in fitted ν and H_{c1} values as the QCP is approached. The universal region is indicated by bright yellow shading. As the temperature is lowered, the system enters the region of universal behaviour (bright yellow shading). The

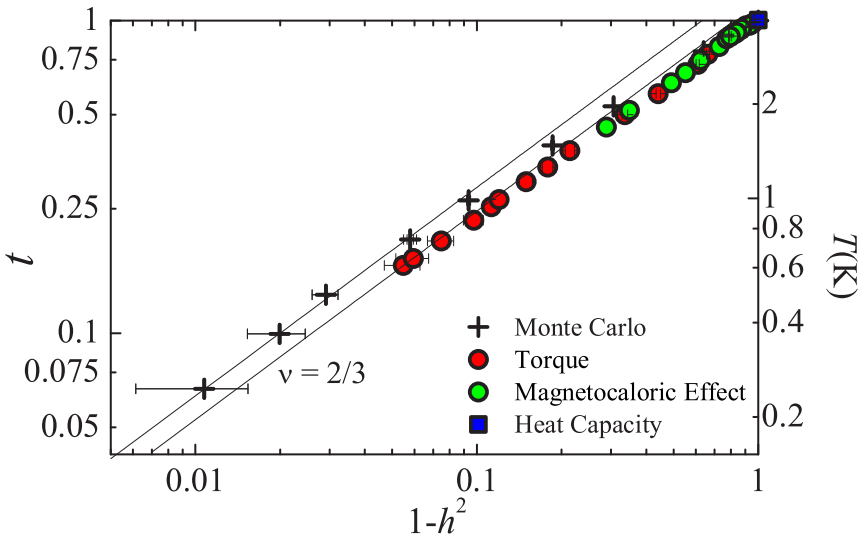

Figure 6.15. $BaCuSi_2O_6$: Experimentally determined phase boundary down to 0.6 K compared with $3d$ BEC mean field estimate on a logarithmic scale. Points on the phase boundary determined from magnetic torque (red circles), magnetocaloric effect (green circles) and heat capacity (square) measurements for $H_{c1} = 23.52$ T, $H_{max} = 36.12$ T, $T_{max} = 3.70$ K and from Monte Carlo simulation (crosses). The lines represent Eqn. 6.6 with $\nu = 2/3$.

value of ν tends to 2/3 in this region as T tends to 0.5 K from above ($T_{win} \sim 0.9$ K), consistent with results in the previous section, characteristic of the $3d$-BEC universality class. However, below these temperatures there is a clear crossover to a value of $\nu = 1$ for the fit range $T < 1$ K ($T_{win} < 0.65$ K). From Eqns. 6.4, it is clear that the value of ν is characteristic of the $3d$-BEC universality class. The origin of this dimensional reduction from $3d$ to $2d$ BEC universality is discussed in the following sections.

In order to unambiguously verify the universality class in the low temperature regime, experimental results are compared with all three measurable power laws in Eqn. 6.4. The uniform magnetisation as a function of temperature and magnetic field (shown in Fig. 6.19) also follows linear power law behaviour, as predicted by Eqn. 6.4 for $d = 2$. The experimental results there-

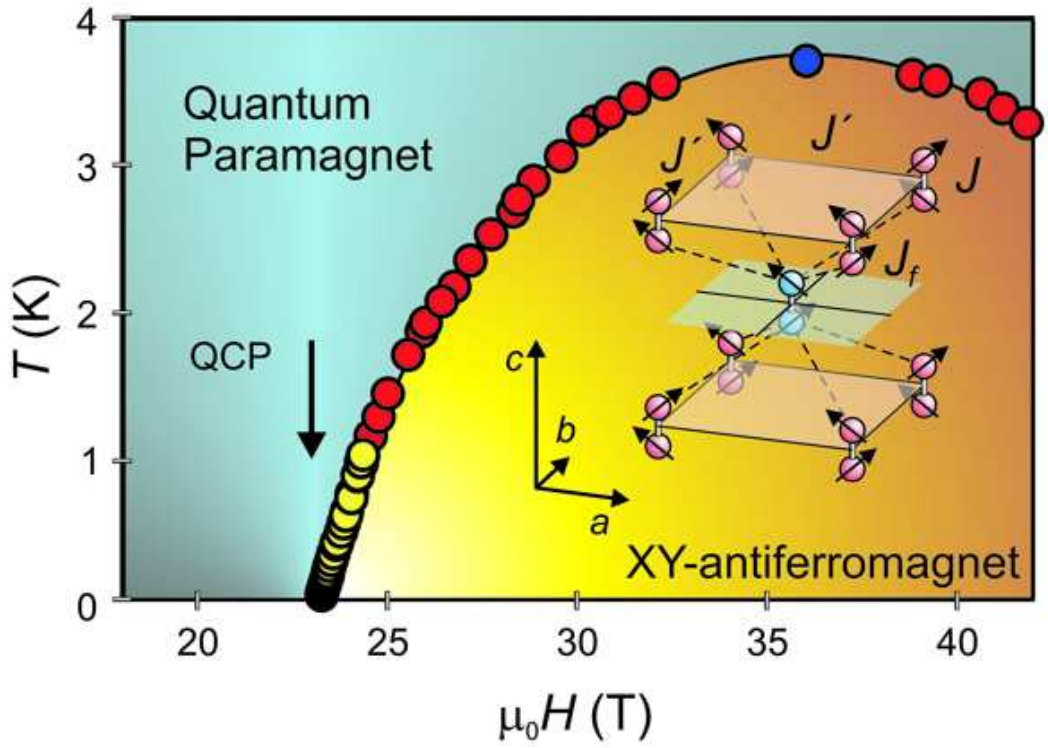

Figure 6.16. $BaCuSi_2O_6$: Experimentally obtained phase boundary in the entire temperature range (error bars are smaller than the symbol size), the shading varies radially from dark to light reflecting the reduction in dimensionality near the QCP. The inset shows a schematic diagram representing the body-centred tetragonal $BaCuSi_2O_6$ crystal lattice. Dimers formed from Cu^{2+} $s = \frac{1}{2}$ spins are shown as dumbbells. It is apparent that this lattice structure leads to geometrical frustration. J is the intra-dimer antiferromagnetic interaction, J' the antiferromagnetic interaction between in-plane dimers and J_f the inter-layer antiferromagnetic interaction which leads to geometric frustration.

fore clearly demonstrate that the measured critical behaviour of the system in the temperature range 30 mK to 1 K is consistent with the $2d$-BEC universality class. Ising-like order due to U(1) symmetry breaking terms can be ruled out, since this would lead to a critical exponent of 0.5 [10]. The effect of disorder would be either a critical exponent $\nu > 4/3$ satisfying the Harris criterion [11; 61; 62] , or a smeared phase transition. Neither the experimentally measured exponent ($\nu = 1$), nor the sharp non-hysteretic transition in the magnetisation characterised by

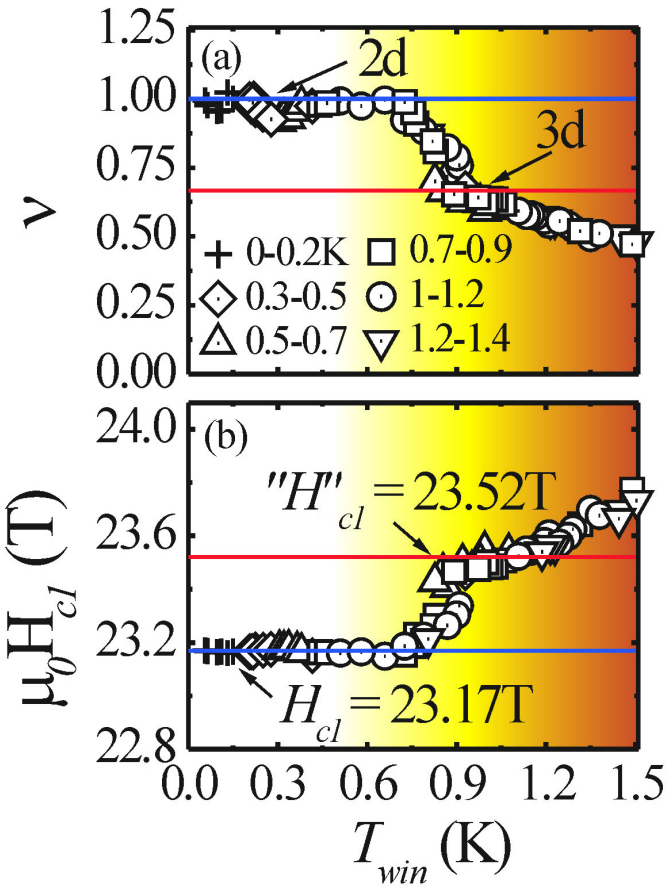

Figure 6.17. $BaCuSi_2O_6$: Experimental measurements of ν and H_{c1} down to 30 mK, showing a crossover from $3d$ to $2d$ behaviour. (a) Values of the critical exponent ν obtained from fitting experimental points on the phase boundary in a sliding windown centred at $T_{\rm win}$ (K). A two-parameter fit with ν and H_{c1} varying is used to fit the data. The window-size varies from 0.05 to 1.4 K, as indicated by different symbols. Solid horizontal lines show the theoretical values of $\nu = 2/3$ and 1 for $2d$- and $3d$-BEC respectively. The data approach $\nu = 2/3$ in the intermediate regime, and there is a distinct crossover toward $\nu = 1$ before the QCP is reached. The shading indicates the transition from the high temperature non-universal regime through the intermediate regime toward the QCP (b) Estimates of H_{c1} obtained along with ν during the fit. H_{c1} approaches 23.52 T in the intermediate regime, and crosses over to 23.17 T before the QCP in approached.

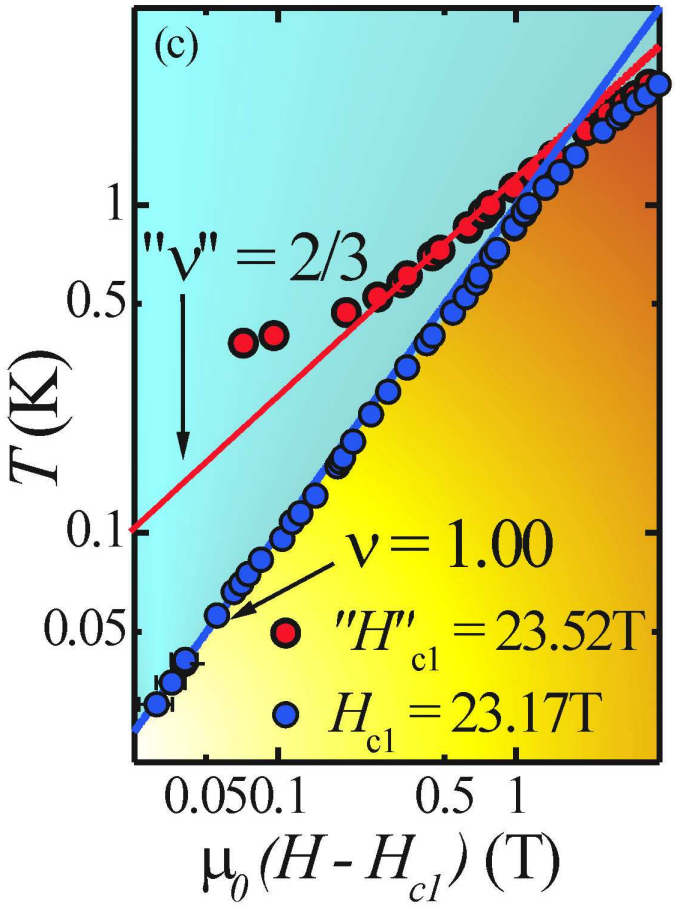

Figure 6.18. $BaCuSi_2O_6$: Best fits to the phase boundary in the intermediate and low temperature regimes represented on a logarithmic scale. The solid lines show that the data in the intermediate temperature range are consistent with the values of $H_{c1} = 23.52$ T and $\nu = 2/3$, which does not fit the lower temperature points; whereas data in the lower temperature range are consistent with $H_{c1} = 23.17$ T and $\nu = 1.00$ which do not fit the higher temperature points. The shading indicates the transition from the high field non-universal regime through the intermediate regime toward the QCP. We observe a crossover from one regime to the other in the temperature range 0.65 K - 0.9 K.

the narrow peak in $\partial^2 M/\partial H^2$ which sharpens at low temperatures (shown in Fig. 6.10), are consistent with a disordered system.

6.5 Dimensional reduction at the QCP due to geometrical frustration

In the following discussion, we show that the mechanism of geometrical frustration leads to the first experimental observation of dimensionally reduced $2d$-quantum criticality in the $3d$ spin system $BaCuSi_2O_6$.

6.5.1 Microscopic spin Hamiltonian

The representative lattice of Fig. 2.9 does not capture the geometrical frustration of the $BaCuSi_2O_6$ lattice (shown in the left inset to Fig. 6.16). The CuO_4 square planes in $BaCuSi_2O_6$ are staggered in the vertical direction, such that a dimer in a single layer is at the centre of the square configuration of dimers in the next layer, but vertically offset. Thus a situation arises where the spins on each dimer cannot simultaneously align in antiparallel fashion with all nearest neighbouring spins on the next vertical layer (i.e. the system configuration is geometrically frustrated.) The microscopic spin Hamiltonian that describes the frustrated lattice is the following:

$$\begin{aligned}\mathcal{H} &= t\sum_{\mathbf{i},\alpha}(b^{\dagger}_{\mathbf{i}+\hat{e}_\alpha}b_{\mathbf{i}} + b^{\dagger}_{\mathbf{i}}b_{\mathbf{i}+\hat{e}_\alpha}) + t'\sum_{\mathbf{i}\beta}(b^{\dagger}_{\mathbf{i}+\hat{e}_\beta}b_{\mathbf{i}} + b^{\dagger}_{\mathbf{i}}b_{\mathbf{i}+\hat{e}_\beta}) \\ &+ V\sum_{\mathbf{i},\alpha} n_{\mathbf{i}}n_{\mathbf{i}+\hat{e}_\alpha} + V'\sum_{\mathbf{i}\beta} n_{\mathbf{i}}n_{\mathbf{i}+\hat{e}_\beta} + \mu\sum_{\mathbf{i}} n_{\mathbf{i}} \qquad (6.7)\end{aligned}$$

where $t = V = J'/2$, $t' = V' = J_f/4$ describe the interacting gas of hardcore bosons populated above a critical potential (where μ is given by $J - g\mu_B H$) moving on a body-centred tetragonal lattice, described by $\hat{e}_\alpha = \{\hat{x}, \hat{y}\}$, $\hat{e}_\beta = \{\hat{z} \pm \hat{x}/2 \pm \hat{y}/2\}$.

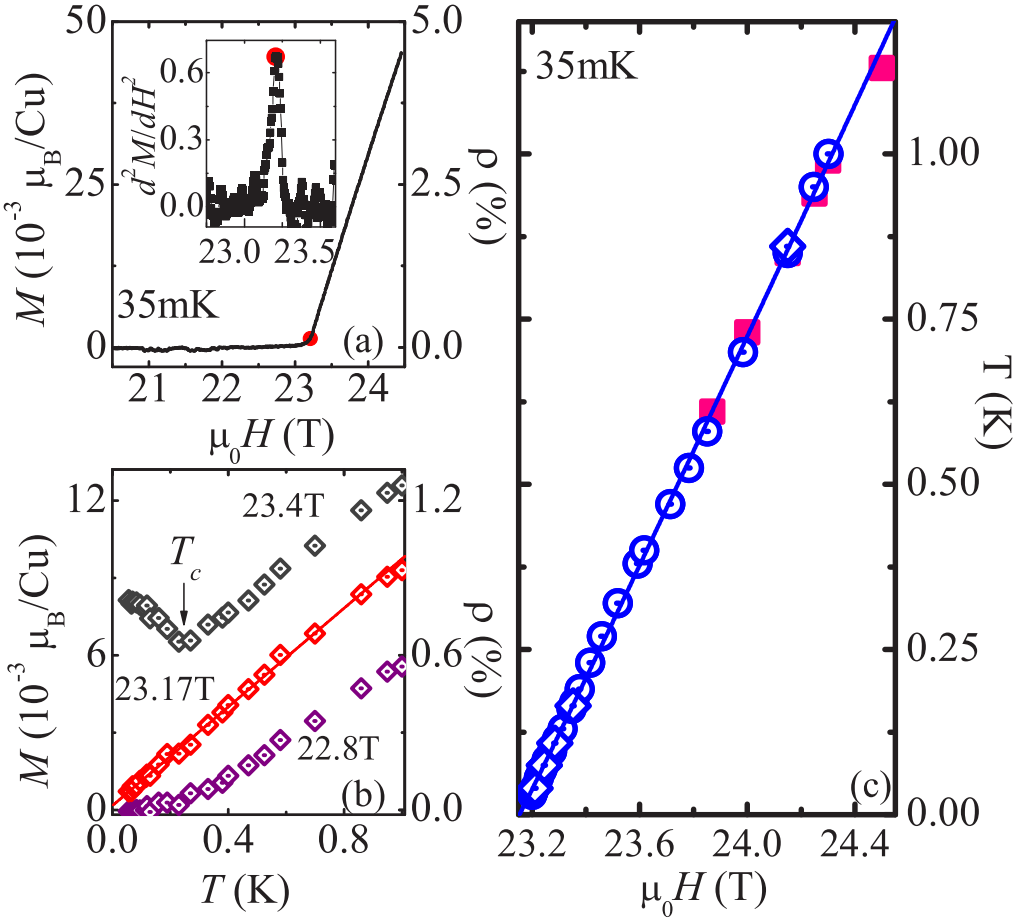

Figure 6.19. Power laws extracted from uniform magnetisation obtained from torque measurements on $BaCuSi_2O_6$ in an external magnetic field applied almost parallel ($\sim$ 10°) to the c-axis. (a) Uniform magnetisation M $\equiv$ particle density (ρ) obtained from torque measured as a function of rising magnetic field at 35 mK. The inset represents the ordering transition, which is indicated on the magnetisation curve (b) M $\equiv$ ρ as a function of temperature extracted from the magnetisation curves in (a) at various temperatures. Representative curves are shown at magnetic fields above, below and at H_{c1} = 23.17 T. T_c = 0 K at H_{c1}, and corresponds to the dip in M at fields above H_{c1}. The solid line shows a linear fit to M at H_{c1}. (c) Phase boundary comprising ordering transitions obtained from magnetisation curves in (a). The solid squares and open symbols represent data taken in a ^{3}He fridge and dilution fridge respectively. The open circles and diamonds represent data taken with the sample in slightly different orientations (the angle was changed by $\sim$ 10° and the field accordingly rescaled by a 0.5% change in g-factor) to verify that the results are independent of orientation. The solid line shows a linear fit below 1 K.

6.5.2 Non-interacting bosons

An effective low energy theory described by the action in Eqn. 2.14 was used to arrive at critical scaling relations in Eqns. 2.15. However, this effective theory is in the continuum limit (i.e. lattice parameter $\rightarrow 0$), and hence does not capture the effect of geometric frustration in the $BaCuSi_2O_6$ lattice. Instead, we approach the problem of geometrical frustration from the single particle limit.

The single particle dispersion relation is given by (Appendix C):

$$\epsilon(\mathbf{k}) \;=\; J \;+\; J'[\cos k_x \;+\; \cos k_y] \;+\; 2J_f[\cos\frac{k_x}{2}\cos\frac{k_y}{2}\cos k_z] \tag{6.8}$$

on substituting $V \;=\; J'/2$ and $V' \;=\; J_f/4$ for the $BaCuSi_2O_6$ lattice in Eqn.C.4. The intra-layer and inter-layer components of the dispersion are shown in Fig. 6.20. $\epsilon(\mathbf{k})$ is minimised by $\mathbf{q} \;=\; (\pi, \pi, k_z)$ and boson condensation occurs with momenta around this minimum.

We expect the same behaviour to be observed at the other QCP H_{c2}. Since the particle operators in the Hamiltonian of Eqn. 2.9 are bosonic, they obey commutation rather than anti-commutation (fermionic) relations. The Kinetic Energy term therefore does not reverse sign on particle-hole reversal (i.e. interchanging b and $b^\dagger$) and hole condensation occurs at the minimum of the hole band $\mathbf{q} \;=\; (\pi, \pi, k_z)$.

Expanding in deviations from the minimum in momentum $\mathbf{k} \;=\; (\pi + \delta k_x, \pi + \delta k_y, k_z)$, the energy takes the form:

$$\epsilon(\mathbf{q} \;+\; \delta\mathbf{k}) \;=\; J \;-\; J'[\cos\delta k_x \;+\; \cos\delta k_x] \;+\; 2J_f[\sin\frac{\delta k_x}{2}\sin\frac{\delta k_y}{2}\cos k_z]. \tag{6.9}$$

Thus the dispersion can be written as:

$$\epsilon(\mathbf{q} \;+\; \delta\mathbf{k}) \;= J \;-\; 2J' \;+\; \frac{J'}{2}(\delta k_x^2 + \delta k_y^2) + \frac{J_f}{2}\delta k_x \delta k_y (1 + \frac{k_z^2}{2}) \tag{6.10}$$

so that there is no k_z dispersion to leading order. This implies that a boson in the condensate that occupies any given layer does not hop to another layer. The vanishing leading order contribution of k_z to the dispersion is a direct consequence of the frustrated form of the inter-layer exchange.

Equivalently, the phase of a single boson (with wavevector $k_x = k_y = \pi$) alternates cyclically on a plaquette of neighbouring lattice sites (shown in Fig. 6.20b), resulting in phase cancellation at each site of the adjacent layer. Hence the effect of geometrical frustration is to decouple adjacent layers, leading to a highly degenerate ground state, which can be described as an array of 2d-BEC layers.

6.5.3 Effect of interactions

A competing effect arises from zero-point phase fluctuations, which generate an effective inter-layer coupling (K) and restore phase-coherence along the c-axis. These zero-point fluctuations can equivalently be represented as interactions between bosons, which generate an effective inter-layer tunneling analogous to the Josephson effect in superconductivity (as shown in the upper right inset to Fig. 6.16) and restore phase-coherence along the c-axis. This effect is due to pairs of bosons with $\mathbf{q} = (\pi, \pi)$ interacting to form bosons with $\mathbf{k} \neq (\pi, \pi)$ which can tunnel between layers. However, since the effective inter-layer coupling K is interaction-induced and is biquadratic in the order parameter, its strength decreases as ρ^2 for low densities of bosons. This result was recently obtained by Maltseva and Coleman [71], using a spin-wave approach on the same spin lattice to derive an unfrustrated effective coupling K between adjacent layers. K is biquadratic in the local order parameter, implying a quadratic density dependence, since the local order parameter $b_i^\dagger$ is proportional to $\rho^{1/2}$ for small values of ρ.

A measure of the '$3d$-ness' of the system is given by the size of the effective coupling K relative to the temperature scale $k_B T_c$. Since T_c is proportional to ρ in the proximity of the

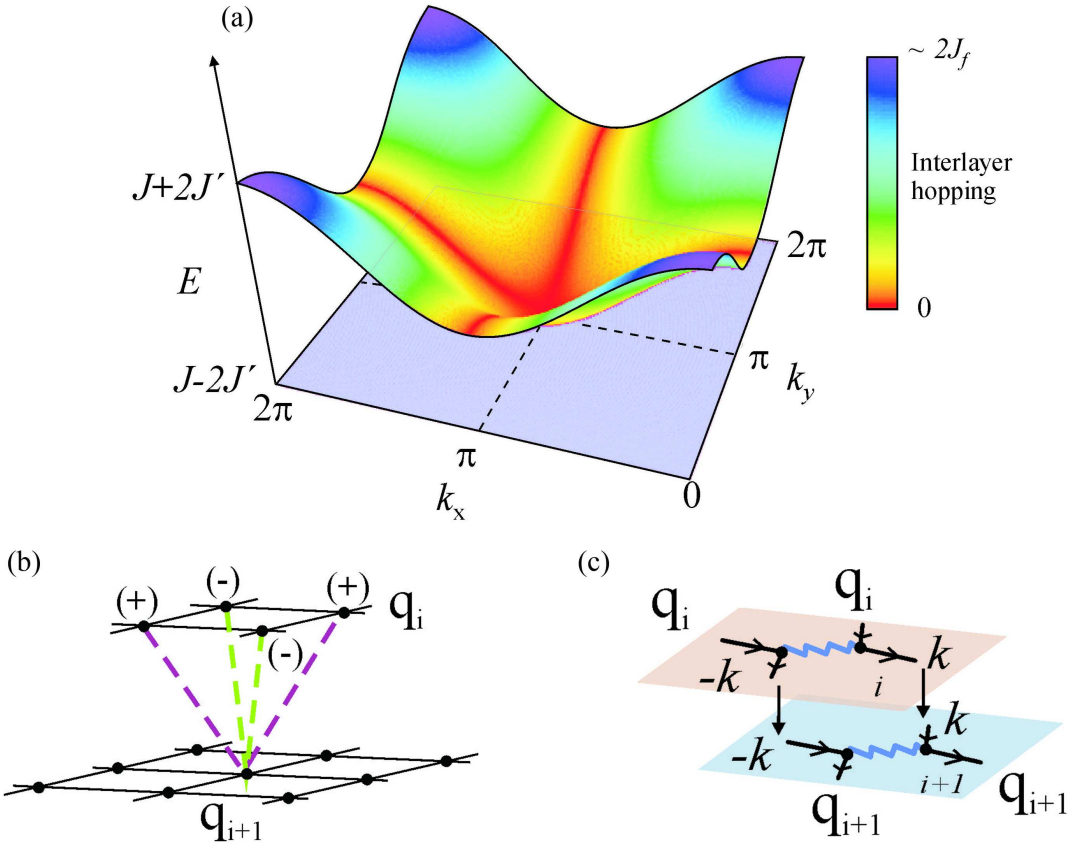

Figure 6.20. (a) Dispersing s_z = 1 triplon band in an applied magnetic field of H_{c1}, with inter-layer exchange shown on a colour scale. The shape of the dispersion is the same in any magnetic field $H \leq H_{c1}$, but the gap to the singlet state decreases with increasing H. At $H = H_{c1}$, the gap to the singlet state is closed at wavevector $k_x = k_y = \pi$, resulting in Bose Einstein condensation. The colour shading represents the inter-layer hopping. At the wavevector where BEC occurs, there is no inter-layer hopping, which leads to a $2d$ BEC QCP. (b) A schematic of the phase alternation of a single boson state with $\mathbf{q} = (\pi, \pi)$, resulting in phase cancellation on the next layer (i.e. no interaction between the two layers.) (c) A schematic of the repulsive interactions between bosons in the condensate, which results in inter-layer pair tunnelling proportional to ρ^2 at low boson densities.

QCP (from Eqns.(1) for d = 2), the ratio $K/\mathrm{k}_B T_\mathrm{c}$ (which is $\propto \rho$) is arbitrarily small close enough to the QCP, and inter-layer tunnelling is too small for the system to be observably $3d$. By field-tuning toward H_{c1}, we experimentally access this region, and hence observe critical power law behaviour consistent with the $2d$-BEC universality class. The energy scale of this 2d-critical behaviour is well separated from the very low temperatures at which weak longer range inter-layer interactions are anticipated to restore $3d$- behaviour; and hence $2d$- behaviour is observed over a significant range of temperature.

To obtain a quantitative measure of whether the system is in fact close to two-dimensional near the QCP at measured temperatures, we compare the theoretical estimate of the critical temperature T_c with the experimentally measured value. A two-dimensional interacting dilute Bose gas undergoes a superfluid transition at critical temperature T_c^{2d}, the magnitude of which has been estimated in [70] to be:

$$T_c^{2d} \;=\; \frac{4\pi\hbar^2 n}{2m^*}\cdot\frac{1}{\ln(\ln(\frac{1}{na^2}))} \;=\; \frac{2\pi\hbar^2\rho}{m^* a^2}\cdot\frac{1}{\ln(\ln(\frac{1}{\rho}))} \tag{6.11}$$

where n is the particle density per unit volume, a is the range of the potential, and m^* is the effective mass.

The effective mass of the experimental system $BaCuSi_2O_6$ is determined from the dispersion relation. Since

$$\omega \;=\; \frac{\hbar^2 k^2}{2m^* a} \tag{6.12}$$

the mass is obtained from the coefficient of k^2 in Eqn. 6.8. From the term

$$J'\left(\cos k_x \;+\; \cos k_y\right) \;\sim\; J'\left(1 \;-\; \frac{k_x^2}{2} \;-\; \frac{k_x^2}{2}\right) \tag{6.13}$$

in the dispersion relation Eqn. 6.8, we obtain

$$\frac{\hbar^2}{2m^* a} \;=\; \frac{J'}{2} \tag{6.14}$$

The particle density can be expressed as a linear function of the distance from the critical magnetic field H_{c1}, and the proportionality constant is determined from the measured data shown in Fig. 6.19a:

$$\rho \ = \ 0.035(H \ - \ H_{\rm c1}) \tag{6.15}$$

Hence the expression for T_c^{2d} reduces to:

$$T_c^{2d} \ = \ \frac{0.035 \ \times 2\pi J'(H \ - \ H_{\rm c1})}{\ln(\ln(\frac{1}{\rho}))} \tag{6.16}$$

On substituting the value of inter-dimer coupling J':

$$J' \ = \ 0.51 \text{ meV} \ = \ 6.8 \text{ T} \tag{6.17}$$

we obtain

$$T_c^{2d} \ = \ \frac{1.5(H \ - \ H_{\rm c1})}{\ln(\ln(\frac{1}{\rho}))} \tag{6.18}$$

such that at the lowest experimentally measured particle concentration (ρ) of ~ 0.3 %,

$$T_c^{2d} \ = \ 0.86(H \ - \ H_{\rm c1}) \tag{6.19}$$

In the case of the experimental $BaCuSi_2O_6$ system, the existence of a small but finite inter-layer coupling away from the QCP leads to a $3d$ phase transition at T_c^{3d}. Since the extent of inter-layer coupling is extremely small, this ordering transition can be compared with the theoretical prediction for a two-dimensional superfluid transition at T_c^{2d}. The measured expression for T_c^{3d} is obtained from the linear fit to experimental data shown in Fig. 6.19c, and is given by:

$$T_c^{3d} \ = \ 0.87(H \ - \ H_{\rm c1}) \tag{6.20}$$

From the excellent correspondence (shown in Fig. 6.21) between the value of T_c^{2d} for a two-dimensional interacting dilute Bose gas in Eqn. 6.19 and the experimentally measured value

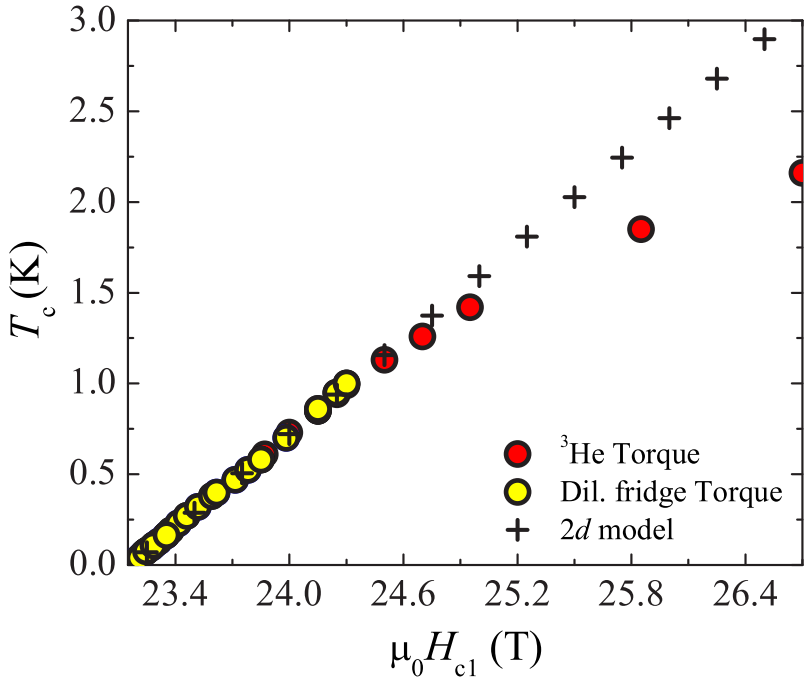

Figure 6.21. $BaCuSi_2O_6$: Comparison between the low temperature experimental phase boundary and theoretical prediction for a $2d$ interacting dilute Bose gas. The circles represent the experimentally measured phase boundary of $BaCuSi_2O_6$ from torque measurements in a ^{3}He and dilution fridge. The crosses represent the theoretical prediction for the phase boundary of a $2d$ interacting dilute Bose gas from Ref. [70]

of T_c^{3d} in Eqn. 6.20, we confirm that experimentally, we are indeed in the limit very close to a two-dimensional system near the QCP.

Away from the QCP, the interaction induced inter-layer tunnelling increases rapidly with particle density, leading to distinctly $3d$-behaviour when $K(\rho)$ becomes comparable to T_c. The system may then be described by an effective unfrustrated model for the subsets of odd and even layers, that assumes a constant effective inter-layer coupling J'' [43]. The change in inter-layer coupling as the QCP is approached is the origin of the change in the fit value of H_{c1} along with ν as proximity to the QCP is tuned. Tuning the system by means of the applied magnetic field

from the unfrustrated region, toward the QCP where geometrical frustration becomes effective, therefore results in a marked crossover from $3d$- to $2d$- BEC power law behaviour.

6.5.4 Two-dimensional quantum fluctuations

These results provide the first experimental example of a bulk $3d$-quantum system in which a $2d$-QCP has been observed, leading to purely $2d$-quantum fluctuations in the order parameter. New phases of matter have been predicted, and explanations proposed for unsolved problems including non-Fermi liquid behaviour and high temperature superconductivity using two-dimensional theories [15; 16; 72; 73; 74; 75]. Real materials, however are usually rendered three-dimensional by quantum effects leading to finite inter-layer tunnelling, known as 'order from disorder'; a $2d$ QCP has not been experimentally observed in any bulk 3d system, and mechanisms for dimensional reduction [16; 63; 64; 65; 66; 67; 68; 69] have thus far remained theoretical conjecture. $BaCuSi_2O_6$ provides a clear example of a system in which geometrical frustration causes the effective dimensionality to become reduced at the QCP, leading to two-dimensional collective excitations despite the three-dimensional nature of the system. While inter-layer decoupling due to geometrical frustration features as a possible explanation for the puzzling experimental observation of non Fermi liquid behaviour at the QCP in body-centred tetragonal heavy fermion intermetallics, theoretical reasoning [71] has been used to assert that it is impossible to realise reduced dimensionality in any system by the mechanism of geometrical frustration. The experimentally observed dimensional reduction in $BaCuSi_2O_6$ provides a counter-example and constitutes a proof of principle that dimensionality can become an emergent property of a QCP.

Chapter 7

Conclusions

"It would be possible to describe everything scientifically, but it would make no sense; it would be without meaning, as if you described a Beethoven symphony as a variation of wave pressure."

- Albert Einstein

My PhD research studied experimental signatures as evidence of the correspondence between magnetic spin dimer systems and BECs. Experimental results reveal a singlet groundstate with a spin gap to dispersive triplet excitation bands. The gap to the excited state is reduced in an external magnetic field, resulting in a magnetically ordered groundstate at a critical field. The applied magnetic field serves as a chemical potential, facilitating experimental approach to the QCP separating the magnetically ordered state from the paramagnetic state. $A_2Cu(BO_3)_2$ (A = Sr, Ba), with a very small ratio of inter-dimer to intra-dimer coupling is closely related to the exactly solvable isolated dimer system and enables a perturbative analysis of the effect of inter-dimer coupling on the spin gap to the excitation spectrum. Certain advantages of the spin dimer compound $BaCuSi_2O_6$ including a more experimentally accessible spin gap and rotationally invariant exchange interactions about the c-axis, make it a better model system

to experimentally measure the phase boundary and hence determine the universality class of the field-tuned QCP. Critical scaling analysis of the experimentally obtained phase boundary in $BaCuSi_2O_6$ establishes that this spin-dimer system is analogous to $3d$ interacting Bose gas systems, with the XY antiferromagnetically ordered state corresponding to a BEC of triplets. While the critical exponents down to $T \sim 0.6$ K are consistent with the $3d$ BEC universality class, the unexpected change in critical exponent closer to the QCP, in the temperature range $0.03 \text{ K} \leq T \leq 0.6$ K is a signature of dimensional reduction, with a $2d$ BEC QCP emerging in the $3d$ $BaCuSi_2O_6$ spin system.

7.1 Spin-dimer physics

Preliminary research focussed mainly on spin dimer physics, and the role of the inter-dimer exchange interactions in determining the critical magnetic field H_{c1}. Dominant antiferromagnetic exchange coupling J between pairs of Cu^{2+} ($s = 1/2$) ions creates spin dimers. It is natural to discuss the physics of these systems in terms of spin dimer units, which have a single ground state and a triplet excited state. The bosonic analogy is drawn by treating each dimer as a hardcore boson, which is considered to be 'present' in the triplet state, and 'absent' in the singlet state. In the presence of an external magnetic field, population of the Bose gas occurs above a critical magnetic field H_{c1} at which the lowest triplet state is Zeeman split sufficiently, to become degenerate with the singlet state. An analogy is drawn between the ordered state above H_{c1} which is an XY canted antiferromanget, and a BEC of triplets.

7.1.1 Inter-dimer exchange in $A_2Cu(BO_3)_2$ (A = Sr, Ba)

The system $Sr_2Cu(BO_3)_2$ has an extremely large spin gap (Δ = 7.2 $\pm$ 0.2 meV), determined from high field magnetisation measurements and powder inelastic neutron scattering (INS)),

such that the critical magnetic field $H_{c1} = \frac{\Delta}{g\mu_B}$ has the value 57 T (62 T) $\pm$ 2T for the orientation in which g = 2.23 (2.06). Powder INS confirms the dimerisation of Cu^{2+} ($s = 1/2$) pairs in this system. In the absence of any inter-dimer interaction, the spin gap would have a value equal to the intra-dimer exchange coupling J (which is measured as 8.6 $\pm$ 0.1 meV from low field susceptibility and powder INS.) Experimental results relate the reduction in H_{c1} from J, to the value of the inter-dimer exchange interactions. The role of these is to cause triplet delocalisation, resulting in a broadened triplet dispersion band, as was observed in powder INS. Another direct probe is to modify the value of inter-dimer exchange interaction while keeping the intra-dimer exchange J constant by substituting A = Ba^{2+} for A = Sr^{2+}, resulting in an experimental observation of the change in spin gap from 7.2 $\pm$ 0.2meV to 7.6 $\pm$ 0.2 meV. Clear evidence was obtained for an ordered ground state above H_{c1}, but the large value of the spin gap made it experimentally unfeasible to unambiguously determine the exact nature of the ordered state.

7.2 BEC quantum critical point

Precise tuning of the particle density of the interacting Bose gas (i.e. the triplet concentration) is possible by controlling the external magnetic field in spin dimer systems. This makes these compounds model experimental systems to study the power laws characterising the approach to the QCP at applied magnetic field H_{c1}. $BaCuSi_2O_6$ is an ideal system to study, since $H_{c1} \sim$ 23.5 T is experimentally accessibly in continuous magnetic fields, and the 4-fold lattice symmetry suggests that exchange interactions are U(1) symmetric. Scaling analysis predicts mean-field exponents for $d \geq 2$. In particular, the exponent for the power law relating the ordering temperature to the proximity to the critical magnetic field: $T_c \propto (H - H_{c1})^{\nu}$ is given by $\nu = 2/d$ in this BEC universality class. Experimental results presented in this thesis

measure the critical exponent ν in $BaCuSi_2O_6$.

7.2.1 Dimensional reduction at the QCP in $BaCuSi_2O_6$

Experimental results from magnetocaloric effect, specific heat, and magnetic torque measurements were used to map out the phase boundary separating the magnetically ordered state from the paramagnetic state in the $BaCuSi_2O_6$ system, which is found to match the ordering phase boundary of a $3d$ dilute Bose gas simulated using Monte Carlo techniques. Critical exponents are extracted from the region of the phase boundary down to T = 0.03 K, such that the region very close to the QCP is accessed. Down to $T \sim 0.6$ K, the critical exponent ν is measured to have the value 0.63 ± 0.03, which is consistent with the exponent $\nu = 2/3$ characteristic of the $3d$ BEC universality class. Surprisingly, in the region closer to the QCP, as $T \rightarrow 0.03$ K, we find a clear crossover to ν = 1 power law behaviour. We interpret this surprising result as characteristic of a $2d$ BEC QCP, in the vicinity of which the value of the critical exponent $\nu = 2/d = 1$. Closer inspection of the microscopic spin Hamiltonian describing $BaCuSi_2O_6$ reveals that the geometrically frustrated interlayer antiferrromagnetic interactions (arising from the body-centred tetragonal structure) result in decoupling of layers of dimers at low particle concentrations. This leads to a truly unique manifestation of a $2d$ BEC QCP characterised by purely $2d$ quantum fluctuations. The experimental tuneability of the triplet concentration in spin-dimer systems uncovers the effect of geometrical frustration near the QCP (where triplet concentrations are very low), resulting in the first experimental observation of a $2d$ QCP in a bulk $3d$ material. This system is a unique example where the notion of 'dimensionality' itself takes on an emergent character at the QCP: individual particles move on a $3d$ lattice, but collective motion occurs in $2d$ planes.

Chapter 8

Implications for future work

"We dance round in a ring and suppose,

But the Secret sits in the middle and knows."

- Robert Frost

This chapter contains a discussion of ideas for future work in a few different areas. Some of these experiments are already in progress, or are planned for the near future. Others involve challenging experimental ideas which may prove extremely rewarding, but require careful study and detailed development in the short term, leading to their practical implementation in the longer term.

8.1 Quasi-two dimensional thermodynamic signatures

Experiments reported as part of this dissertation measure critical exponents as evidence of a two dimensional QCP. The phase transition in the vicinity of this QCP is quasi-two dimensional, with a small three dimensional component. Additional evidence for the $2d$ QCP can be obtained by a measure of a thermodynamic quantity such as specific heat, which is expected to show a quasi-two dimensional phase transition. An experimental measurement of specific heat as a

function of temperature near the QCP is expected to reveal a $2d$ KT-crossover to which a very small component of the $3d$ lambda anomaly is added.

8.2 Change in universality class due to symmetry-breaking terms

A prerequisite for BEC is that rotational U(1) symmetry is not explicitly broken. The equivalent magnetic lattice used to represent $BaCuSi_2O_6$ comprises exchange interactions which are rotationally invariant around the crystalline c-axis, indicating that there are no anisotropic terms that explicitly break U(1) symmetry in the spin Hamiltonian.

A interesting possibility is to introduce a finite symmetry-breaking term, and measure the change in critical exponent due to the change in universality class. Possible ways of introducing symmetry-breaking terms include the introduction of magnetic-zeros (such as Zn) in the place of a few Cu^{2+} spins in the lattice, and uniaxial strain to break the XY symmetry.

8.3 Pressure-induced quantum phase transition

A large part of the research presented in this thesis focussed on studying the magnetic-field induced ordering transition in spin dimer compounds. In this case, the degeneracy of the excited triplon state is lifted by the external magnetic field. The energy of the lowest $s_z = 1$ dispersive triplet band becomes degenerate with the singlet ground state at an applied magnetic field $H_{c1} = \frac{\Delta}{g\mu_B} \sim 23.2$ T, where the system orders as a Bose Einstein condensate of triplets.

Another way of tuning the system to an ordered state is by applying external pressure to the system. Applied pressure (P) is expected to lead to a reduction in the spin gap due to an increase in the ratio of inter-dimer to intra-dimer coupling, and ultimately result in its collapse. Unlike the case of field-tuning, however, pressure-tuning leads to a lowering in energy of all three triplet states (s = 1 ; s_z = +1, 0 and -1). In this case, the degenerate triplon bands with

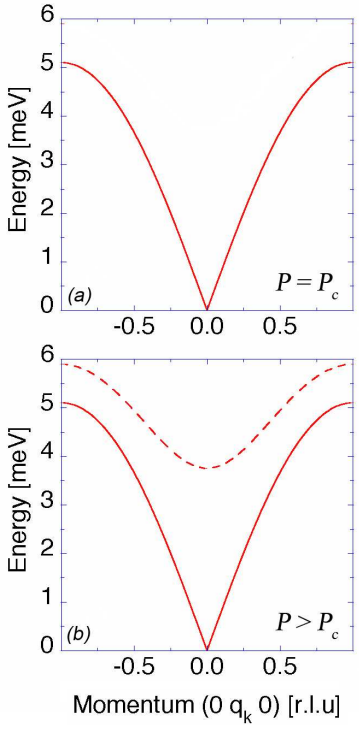

Figure 8.1. (a) Spin dynamics at the pressure-induced QCP, measurements made on $TlCuCl_3$ [77]. All three triplet modes are degenerate and linear at P_{c1}. (b) Spin dynamics in the pressure-induced ordered phase. The two degenerate transverse Goldstone modes are represented by a solid line and the longitudinal amplitude mode by a dashed line.

a gapped quadratic dispersion in zero field are theoretically predicted to continuously evolve to a gapless and linear dispersion at $P = P_c$ [9]. The nature of the ordered state induced by applied pressure is qualitatively different from that induced by applied magnetic field. In the pressure-induced ordered state, the three gapless linear modes at the QCP evolve into a gapped longitudinal spin wave branch and two gapless transverse spin wave branches (shown in Fig. 8.1) with strongly pressure dependent gap and stiffness respectively. These modes have been observed in measurements on the spin dimer compound $TlCuCl_3$ [77]. The spin wave modes are characteristic of a 'classical' ordered antiferromagnet. The effective field theory

describing the pressure-induced QPT to this ordered state has a dynamical critical exponent z = 1 (reflecting the linear dispersion of all the three triplet states when the gap is closed at $P = P_c$.) The universality class of the pressure-induced QCP is O(3) symmetry breaking (since there is no anisotropy arising from an applied magnetic field), and two Goldstone modes specify the rotations of the staggered moment. Since z = 1, the characteristic exponent ν = 1/2.

This is in contrast to the field-induced QCP, which is described by an effective field theory with dynamical critical exponent z = 2 (reflecting the quadratic dispersion of the lowest triplet state when the gap is closed at $H = H_{c1}$.) This QCP is O(2) symmetry breaking, with the plane of the staggered moment dictated by the applied magnetic field. Rotation of the moment corresponds to the single Goldstone mode. As described earlier, the critical exponent characterising a $3d$-BEC QCP is ν = 2/3, and a $2d$-BEC QCP is characterised by ν = 1.

Magnetic field and pressure in conjunction can also be used to drive the system into an ordered state. Experiments are currently in progress in collaboration with S. Tozer at the NHMFL, Tallahassee to map out the ordering transition as the QCP is approached as a function of pressure and applied magnetic field. These results will provide a useful complement to the phase boundary determined in an applied magnetic field. We can thus arrive at a map of phase space as the QCP is approached along two tuning directions: H and P.

8.4 Spin currents

The description of a magnetically ordered spin dimer compound as a triplet BEC leads to the next question: since an interacting BEC is a superfluid, can one observe a spin analogue of superfluidity in these compounds? The equivalent of superfluid flow without viscosity would be a ‘spin current’ flow without dissipation in a BEC of triplets. A spin current flows without a net particle flow, as opposed to a superfluid of atoms.

In an ideal scenario, spin can be treated as a conserved variable, and the components of a spin density s_i obey the continuity equation

$$\frac{\partial s_k}{\partial t} + \frac{\partial j_{ki}}{\partial x_i} = 0 \tag{8.1}$$

The order parameter characterising the 'superfluid' phase is a complex scalar

$$\psi = |\psi| e^{i\phi} \ , \tag{8.2}$$

and the symmetry in the phase ϕ is broken at the BEC ordering transition. Since the phase of the BEC is analogous to the in-plane orientation of the XY-ordered spins, a gradient in phase can be created by a spiral arrangement of arrays of spins [24]. This gives rise to a macroscopic spin current with velocity

$$v_\nabla = \frac{\hbar}{2m} \nabla \phi \tag{8.3}$$

In addition, a localised density ρ of spins with finite magnetisation must be created in order to be transported by the spin current. Once the necessary ingredients for a phase gradient of spins and a local wavepacket of magnetisation have been created, the 'gradient' energy is given by:

$$F_\nabla = \frac{1}{2} \rho v_\nabla^2 \tag{8.4}$$

and a spin current is generated, which is expressed as

$$j = \frac{\partial F_{\nabla}}{\partial v_{\nabla}} \tag{8.5}$$

In reality, however, the continuity equation is not strictly obeyed for spins: the spin density is not conserved, since triplets can be created from singlets as a result of various additional interaction terms in the Hamiltonian. Hence, unlike superfluids, we do not expect spin currents in spin dimer systems to flow forever. In order to measure a spin current, an ultrafast experiment is required, where a measurement is made before the system has time to create magnetisation that counterbalances the spin (magnetisation) gradient.

Although experimentally challenging, it is certainly worthwhile to pursue the creation and observation of spin currents in spin dimer systems. Spin current, unlike charge currents are associated with a flow of angular momentum, which is a vector quantity. This makes is possible for quantum information to be transported, which may have significant implications for the future of quantum computation.

8.5 Locally critical quantum phase transitions

The first experimental observation of a purely $2d$ QCP in $BaCuSi_2O_6$ makes it a particularly promising model system to test theoretical predictions involving $2d$ quantum fluctuations. One such theory that has been a topic of much recent debate is that of 'locally critical quantum phase transitions', which is discussed in detail in ref. [15].

This theory has been proposed to explain the anomalous quantum critical behaviour observed near the magnetic QCP separating an antiferromagnet from a paramagnet in the heavy fermion system $CeCu_{6-x}Au_x$ (where x $\sim$ 0.1 at criticality.) However, it is hypothesised that locally critical physics is ubiquitous in strongly correlated metals, with direct implications for the role of quantum criticality in high temperature superconductors. For example, the theory

might explain the apparent quantum-critical behavior observed over essentially the entire Fermi surface in optimally doped $Bi_2Sr_2CaCu_2O_{8+\delta}$ [14].

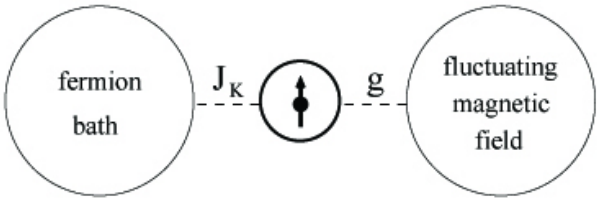

Figure 8.2. Effective impurity Kondo model. The local moment is coupled to two dissipative baths, one fermionic and the other bosonic. The bosonic bath describes a fluctuating magnetic field. The couplings to the two baths are J_k and g, respectively. Figure from ref. [15].

As described in ref. [15], a locally critical quantum phase transition is one where local critical degrees of freedom coexist with spatially extended ones. At a quantum phase transition, quantum fluctuations couple local degrees of freedom to dissipative baths, resulting in their becoming critical. The microscopic descriptions of this model is a Kondo lattice; at each lattice site, a local moment interacts via an exchange coupling with the spin of any conduction electron at the site. This is equivalently described by a local moment simultaneously coupled to two dissipative baths - a fermionic bath that accounts for temporal fluctuations arising from hopping of electrons between the local site and the rest of the lattice, and a bosonic bath that represents the fluctuating magnetic field generated by the local moments at all other sites (shown in Fig. 8.2).

If the spin fluctuations are three dimensional, the lattice system orders before the effective local problem has a chance to become critical. However, if the spin fluctuations are two dimensional, the lattice system reaches its ordering transition precisely at the point where the local problem also becomes critical (shown in Fig. 8.3). Thus two kinds of critical degrees of freedom coexist: long-wavelength fluctuations of the order parameter, and local fluctuations

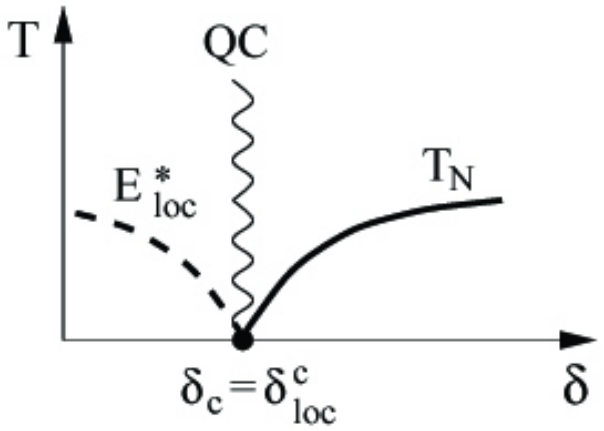

Figure 8.3. Locally critical quantum phase transition in Kondo lattices in the case of $2d$ spin fluctuations. The tuning parameter δ in this case is the ratio of the RKKY interaction to the Kondo energy scale T_k. $E^*_{\rm loc}$ is the local energy scale, and T_N is the antiferromagnetic transition temperature. The wavy line denotes the quantum critical region. Here, $\delta_c = \delta^c_{\rm loc}$, that is, $E^*_{\rm loc}$ vanishes at the QCP. Local and spatially-extended critical degrees of freedom coexist in the quantum critical regime. Figure from ref. [15].

originating from the local moments, resulting in a locally critical phase transition.

Current experimental evidence for this theory is suggestive, but not conclusive, since the effects of the effective bosonic field and the local moments cannot be experimentally decoupled. $BaCuSi_2O_6$ is therefore a model system to experimentally test this theory. This material is a Mott insulator with a $2d$ QCP, if conduction electrons could be doped into the system, this might provide the perfect environment for a locally critical quantum phase transition.

A series of early experiments I attempted involving chemically various Mott insulating oxides seem to indicate that these materials prove extremely robust to charge doping, with chemical dopants resulting in the formation of impurity phases. Nevertheless, other experimental methods such as high pressures to close the insulating band gap, or optical excitations may prove more effective at doping charge carriers without modifying the spin structure of the

system.

Regardless of whether this specific theory is proven to be valid or not, the experimental observations at the QCP of $BaCuSi_2O_6$ doped with conduction electrons will provide valuable information on quantum criticality induced novel phenomenon such as high temperature superconductivity in strongly correlated electron systems.

"Polonius: What do you read, my lord?

Hamlet: Words, words, words."

- Hamlet, II, ii, Shakespeare

Appendix A

Canted XY antiferromagnetic order

The ordered state can be interpreted in terms of the constituent $s = \frac{1}{2}$ spins. In this description, the nature of the long range magnetic order is canted XY antiferromagnetism. The net uniform and staggered magnetisation, as well as the relative orientation of the $s = \frac{1}{2}$ spins in the ordered state are calculated in this section.

The ordered state is represented by a wavefunction representing a coherent superposition of a singlet and the lowest $s = 1$ triplet: $|\psi\rangle = u \cdot e^{i\phi}|\tilde{\uparrow}\rangle + v \cdot |\tilde{\downarrow}\rangle$, where the angle ϕ represents the orientation of the entire XY-plane of spins, which is free to rotate uniformly about the Z-axis.

The expectation value of each of the spin operators is given by:

$$\begin{aligned}
\langle\psi|s_1^z|\psi\rangle &= \langle\psi|s_2^z|\psi\rangle \\
&= \frac{1}{4}\langle\psi|I|\psi\rangle + \frac{1}{2}\langle\psi|\sigma^z|\psi\rangle \\
&= \frac{u^2}{4}\langle\tilde{\uparrow}|I|\tilde{\uparrow}\rangle + \frac{v^2}{4}\langle\tilde{\downarrow}|I|\tilde{\downarrow}\rangle + \frac{u^2}{2}\langle\tilde{\uparrow}|\sigma^z|\tilde{\uparrow}\rangle + \frac{v^2}{2}\langle\tilde{\downarrow}|\sigma^z|\tilde{\downarrow}\rangle \\
&= \frac{u^2+v^2}{4} + \frac{u^2-v^2}{4} \\
&= \frac{u^2}{2}
\end{aligned} \tag{A.1}$$

$$\begin{aligned}
\langle\psi|s_1^x|\psi\rangle &= \frac{1}{2}\langle\psi|s_1^+ + s_1^-|\psi\rangle \\
&= -\frac{1}{2\sqrt{2}}\langle\psi|\sigma^+ + \sigma^-|\psi\rangle \\
&= -\frac{1}{2\sqrt{2}}u\cdot v\cdot\cos\phi\left(\langle\tilde{\uparrow}|\sigma^+|\tilde{\downarrow}\rangle + \langle\tilde{\downarrow}|\sigma_1^-|\tilde{\uparrow}\rangle\right) \\
&= -\frac{u\cdot v\cdot\cos\phi}{\sqrt{2}} \qquad \text{(A.2)}
\end{aligned}$$

$$\begin{aligned}
\langle\psi|s_2^x|\psi\rangle &= \frac{1}{2}\langle\psi|s_2^+ + s_2^-|\psi\rangle \\
&= \frac{1}{2\sqrt{2}}\langle\psi|\sigma^+ + \sigma^-|\psi\rangle \\
&= \frac{1}{2\sqrt{2}}u\cdot v\cdot\cos\phi\left(\langle\tilde{\uparrow}|\sigma^+|\tilde{\downarrow}\rangle + \langle\tilde{\downarrow}|\sigma_1^-|\tilde{\uparrow}\rangle\right) \\
&= \frac{u\cdot v\cdot\cos\phi}{\sqrt{2}} \qquad \text{(A.3)} \\
&= -\langle\psi|s_1^x|\psi\rangle
\end{aligned}$$

From Eqns. A.1, A.2, A.3, the relative in-plane orientation of the two $s = \frac{1}{2}$ spins in each dimer, and the canting angle of the spins out of the plane can be computed.

The relative in-plane orientation of the two spins in each dimer is given by

$$\theta_{1,2} = \arccos\left(\frac{\langle s_1^x\rangle\cdot\langle s_2^x\rangle}{|\langle s_1^x\rangle|\cdot|\langle s_2^x\rangle|}\right) = 180^\circ \qquad \text{(A.4)}$$

The canting angle of each dimer out of the plane (in the direction of the applied magnetic field) is given by

$$\begin{aligned}
\Phi = \arctan\left(\frac{\langle s_1^z\rangle}{\langle s_1^x\rangle}\right) &= \arctan\left(\frac{u^2\sqrt{2}}{2u\cdot v\cdot\cos\phi}\right) \qquad \text{(A.5)} \\
&= \arctan\left(\frac{u}{\sqrt{2}v}\right) \qquad \text{for} \quad \phi = 0 \qquad \text{(A.6)}
\end{aligned}$$

Appendix B

Crystalline Anisotropy

Crystalline anisotropy results in an anisotropic value of the g-factor along each of the principal crystalline axes. The anisotropy in g-factor scales the magnetic susceptibility, resulting in a net torque on the crystal in an applied magnetic field. The dependence of the g-factor and the torque on crystalline anisotropy are calculated for a general case in this section.

B.1 Anisotropic-g tensor

The most general form of the Zeeman splitting term in the Hamiltonian is written as

$$\Delta\mathcal{H} = \mu_b \cdot \mathbf{B} \cdot \overleftrightarrow{g} \cdot \mathbf{J} \tag{B.1}$$

where

$$\overleftrightarrow{g} = \begin{pmatrix} g_{11} & g_{12} & g_{13} \\ g_{21} & g_{22} & g_{23} \\ g_{31} & g_{32} & g_{33} \end{pmatrix} \tag{B.2}$$

Since the direction of the azimuthal (ζ) axis can be selected arbitrarily, we select it to be the direction of $\mathbf{B} \cdot \overleftrightarrow{g}$

Hence the entire magnitude of the vector $\mathbf{B}\cdot\overleftrightarrow{g}$ is projected along the ζ-axis, and the Zeeman term in the Hamiltonian can be written as:

$$\Delta\mathcal{H} = \mu_b|\mathbf{B}\cdot\overleftrightarrow{g}|J_\zeta \tag{B.3}$$

and the energy eigenvalue is given by

$$\Delta E = \mu_b|\mathbf{B}\cdot\overleftrightarrow{g}|m_J \tag{B.4}$$

where m_J is the total angular momentum quantum number, which is equal to m_s in the absence of orbital angular momentum.

The leftrightarrow $\overleftrightarrow{g}$ can be diagonalised by judicious choice of reference frame, the diagonal components of $\overleftrightarrow{g}$ are known as the principal values of $\overleftrightarrow{g}$, lying along the principal axes. The principal axes of g are determined by the symmetry of the crystalline system.

$$\overleftrightarrow{g} = \begin{pmatrix} g_a & 0 & 0 \\ 0 & g_b & 0 \\ 0 & 0 & g_c \end{pmatrix} \tag{B.5}$$

Along this set of principal axes of $\overleftrightarrow{g}$, the components of $\mathbf{B}$ can be written as

$$\mathbf{B} = (l, m, n)B \tag{B.6}$$

where l, m and n are directional cosines of $\mathbf{B}$ with respect to the three principal axes of $\overleftrightarrow{g}$.

The energy eigenvalues from B.4 are given by

$$\Delta E = \mu_b |\mathbf{B} \cdot \overleftrightarrow{g}| m_J \tag{B.7}$$

$$= \mu_b |(g_a l, g_b m, g_c n)| B m_J \tag{B.8}$$

$$= \mu_b |\sqrt{(g_a l)^2 + (g_b m)^2 + (g_c n)^2}| B m_J \tag{B.9}$$

such that the general value of g-factor in any direction is given by:

$$g_\theta = \sqrt{(g_a l)^2 + (g_b m)^2 + (g_c n)^2} \tag{B.10}$$

In the case of tetragonal crystal symmetry, one of the principal axes (we shall consider the $\hat{c}$ axis) is the crystalline axis with four-fold symmetry perpendicular to the plane of the sample, and the other two principal axes ($\hat{a}$ and $\hat{b}$) are the equivalent in-plane crystal axes. Hence two of the principal values of g are identical (i.e. g_a = g_b), and only one directional cosine is required to resolve B into components: $\cos\theta$, where θ is the angle between the field and the crystalline axis of symmetry. The g-factor simplifies to the form

$$g_\theta = \sqrt{(g_a \sin\theta)^2 + (g_c \cos\theta)^2} \tag{B.11}$$

B.2 Torque due to magnetic anisotropy

The geometry of the sample mounted on a cantilever for magnetisation measurements is represented in Fig. B.1.

The torque for this geometry can be computed from the expression

$$\tau = -\mu_0 V \mathbf{M} \times \mathbf{H} \tag{B.12}$$

where V is the volume of the sample. Since the applied magnetic field $\mathbf{H}$ is applied along the spatial z-axis, the expression for torque can be written in terms of its components as

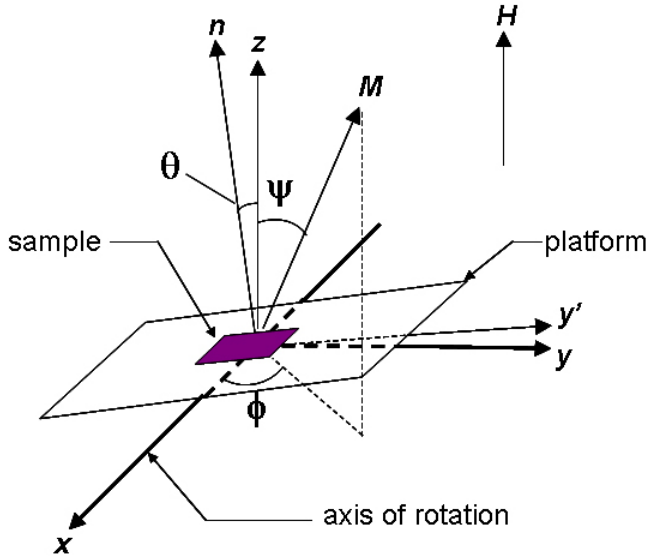

Figure B.1. Geometry for magnetisation measurements using a torque cantilever. The sample is mounted on a platform which rotates about the $\hat{x}$-axis. The magnetic field H points along $\hat{z}$. The sample normal points along $\hat{n}$, which is in the zy plane at an angle θ relative to the $\hat{z}$-axis. The direction of the magnetisation M is specified by the polar angle ψ and the azimuthal angle ϕ.

$$\begin{aligned} \frac{\tau}{V} &= \mu_0 \left(M_y H_z, -M_x H_z, 0\right) \\ \frac{\tau_x}{V} &= \mu_0 M_y H_z \end{aligned} \tag{B.13}$$

In order to compute the anisotropic magnetisation, we consider the most general expression for anisotropic susceptibility in spherical co-ordinates, where $\chi_\perp$ is the susceptibility along the sample normal $\hat{n}$ and $\chi_{||}$ is the susceptibility in the plane perpendicular to $\hat{n}$:

$$\overleftrightarrow{\chi} = -\begin{pmatrix} \chi_\perp \cos^2\phi \sin^2\theta + \chi_{||} \sin^2\phi + \chi_{||} \cos^2\phi \cos^2\theta & (\chi_\perp - \chi_{||}) \sin\phi \cos\phi \sin^2\theta & (\chi_\perp - \chi_{||}) \cos\phi \sin\theta \cos\theta \\ (\chi_\perp - \chi_{||}) \sin\phi \cos\phi \sin^2\theta & \chi_\perp \sin^2\phi \sin^2\theta + \chi_{||} \cos^2\phi + \chi_{||} \sin^2\phi \cos^2\theta & (\chi_\perp - \chi_{||}) \sin\phi \sin\theta \cos\theta \\ (\chi_\perp - \chi_{||}) \cos\phi \sin\theta \cos\theta & (\chi_\perp - \chi_{||}) \sin\phi \sin\theta \cos\theta & \chi_\perp \cos^2\theta + \chi_{||} \sin^2\theta \end{pmatrix}$$

The magnetisation is given by

$$\mathbf{M} = \overleftrightarrow{\chi} \cdot \mathbf{H} \tag{B.14}$$

If the in-plane axes perpendicular to $\hat{n}$ are identical (e.g. for tetragonal symmetry), the in-plane angle ϕ can be taken to be 90° without loss of generality. Since the applied magnetic field $\mathbf{H}$ is along the z-axis, the magnetisation vector can be written as

$$\mathbf{M} = \left(0, -(\chi_\perp - \chi_{||}) \sin\theta \cos\theta, -(\chi_\perp \cos^2\theta + \chi_{||} \sin^2\theta)\right) H$$

The expression for the torque reduces to

$$\begin{aligned} \frac{\tau_x}{V} &= -\mu_0 (\chi_\perp - \chi_{||}) H^2 \sin\theta \cos\theta \\ &\propto \mu_0 (g_c - g_a) H^2 \sin\theta \cos\theta \end{aligned} \tag{B.15}$$

since for the case of tetragonal symmetry, the principal g-axis $\hat{c}$ is along the normal to the plane of the sample, and the equivalent principal g-axes $\hat{a}$ and $\hat{b}$ are in the plane of the sample.

Since we know from Eqn. B.11 that $g_\theta = \sqrt{(g_a \sin\theta)^2 + (g_c \cos\theta)^2}$, the expression for torque in Eqn. B.15 may be rewritten as

$$\frac{\tau_x}{V} \propto \mu_0 H^2 \frac{\partial g_\theta^2}{\partial \theta} \cdot \frac{1}{g_a + g_c} \tag{B.16}$$

Appendix C

Single particle dispersion relation

A simple estimate of the single-particle dispersion for a body-centred tetragonal lattice is calculated using the tight binding approximation in this section.

Fig. C.1 shows a schematic of neighbouring staggered layers in a body-centred tetragonal lattice. The in-plane and intra-plane dispersion can be calculated using the tight binding approximation, taking into account nearest and next-nearest neighbouring atoms. In the tight binding approximation, the dispersion relation is expressed as

$$\epsilon(\mathbf{k}) = \Delta + \sum_{nn} V(\mathbf{R}) \cos(\mathbf{k} \cdot \mathbf{R}) \tag{C.1}$$

From Fig. C.1, we can see that the atom at the origin (layer n) has 4 next nearest neighbours in the same layer, at $\mathbf{R} = a(0, \pm 1, 0),\ a(\pm 1, 0, 0)$ and 8 nearest neighbours in consecutive layers n+1 and n-1, at $\mathbf{R} = a(\pm\frac{1}{2}, \pm\frac{1}{2}, \pm\frac{c}{a})$

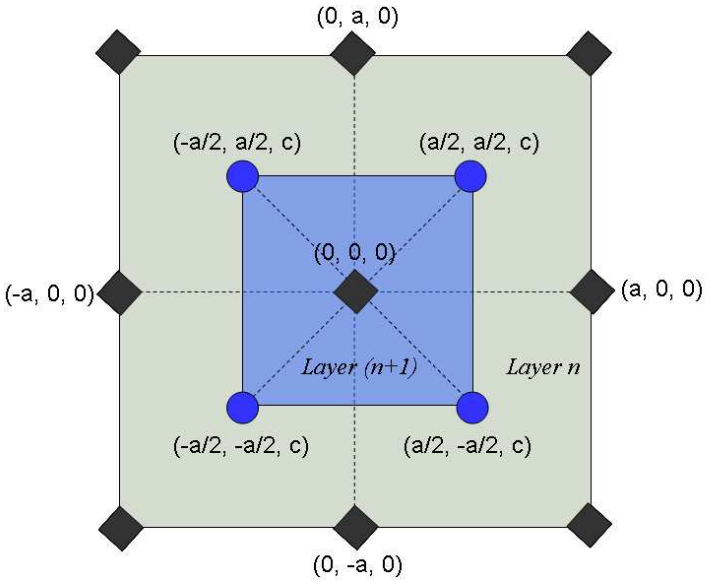

Figure C.1. Consecutive layers in a body-centred tetragonal lattice. Dimensions of the lattice are (2c, a, a). The diamonds represent atoms on the nth layer, and the circles represent atoms on the (n+1)th layer. The origin is represented by an atom on the nth layer, and the nearest and next nearest atoms are represented in the schematic.

Substituting the positional co-ordinates of the atoms neighbouring the origin in Eqn. C.1, the dispersion relation can now be written as

$$\begin{aligned}\epsilon(\mathbf{k}) \;=\; \Delta \;&+\; V[2\cos k_x \;+\; 2\cos k_y] \\ &+\; V\text{'}[2\cos(\frac{k_x}{2} \;+\; \frac{k_y}{2} \;+\; k_z) \\ &+\; 2\cos(\frac{k_x}{2} \;-\; \frac{k_y}{2} \;+\; k_z) \\ &+\; 2\cos(-\frac{k_x}{2} \;+\; \frac{k_y}{2} \;+\; k_z) \\ &+\; 2\cos(\frac{k_x}{2} \;+\; \frac{k_y}{2} \;-\; k_z)] \end{aligned} \tag{C.2}$$

where V is the potential energy between in-plane atoms, and V' is the potential energy between atoms on consecutive planes. The first two terms in the dispersion relation are from

in-plane next nearest neighbours, and the last six terms are from consecutive plane nearest neighbours.

Making use of the trigonometric identity

$$\begin{aligned}\cos(A + C + D) &= [\cos A \cos C \cos D - \cos A \sin C \sin D \\ &- \sin A \sin C \cos D - \sin A \cos C \sin D] \end{aligned} \tag{C.3}$$

the dispersion relation simplifies to the form

$$\epsilon(\mathbf{k}) = \Delta + V[2\cos k_y + 2\cos k_x] + V'[8\cos\frac{k_x}{2}\cos\frac{k_y}{2}\cos k_z] \tag{C.4}$$

REFERENCES

[1] Bramwell, S. T. & Gingras, M. J. P., Spin Ice State in Frustrated Magnetic Pyrochlore Materials. *Science* **294**, 1495 (2001).

[2] Manoharan, H. C., Lutz, C. P., & Eigler, D. M., Quantum mirages formed by coherent projection of electronic structure. *Nature* (London) **403**, 512 (2000).

[3] Finne, A. P. *et al.*, An intrinsic velocity-independent criterion for superfluid turbulence. *Nature* (London) **424**, 1022 (2003).

[4] Giamarchi, T. & Tsvelik, A. M., Coupled ladders in a magnetic field, *Phys. Rev. B.* **59**, 11398 (1999).

[5] Nikuni, T. *et al.*, Bose-Einstein Condensation of Dilute Magnons in $TlCuCl_3$. *Phys. Rev. Lett.* **84**, 5868 (2000).

[6] Andrews, M. R. *et al.*, Observation of Interference Between Two Bose Condensates. *Science* **275**, 637 (1997).

[7] Eisenstein, J. P. & MacDonald, A. H., Bose-Einstein condensation of excitons in bilayer electron system. *Nature* (London) **432**, 691 (2004).

[8] Rice, T. M., To Condense or Not to Condense, *Science* **298**, 760 (2002).

[9] Matsumota, M. *et al.*, Field- and pressure-induced magnetic quantum phase transitions in $TlCuCl_3$. *Phys. Rev. B* **69**, 054423 (2004).

[10] Sachdev, S., *Quantum Phase Transitions* (Cambridge University Press, 1999).

[11] Fisher, M. P. A. *et al.*, Boson localization and the superfluid-insulator transition. *Phys. Rev. B.* **40**, 546 (1989).

[12] Sebastian, S. E. *et al.*, Characteristic Bose-Einstein condensation scaling close to a quantum critical point in $BaCuSi_2O_6$. Phys. Rev. B. **72**, 100404(R) (2005).

[13] Sebastian, S. E. *et al.*, Dimensional reduction at a quantum critical point. (to appear in *Nature* (London)) (2006).

[14] Valla, T. *et al.*, Evidence for Quantum Critical Behavior in the Optimally Doped Cuprate $Bi_2Sr_2CaCu_2O_{8+\delta}$. *Science* **285**, 2110 (1999).

[15] Si, Q. *et al.*, Locally critical quantum phase transitions in strongly correlated metals. *Nature* **413**, 804 (2001).

[16] Mathur, N. D. *et al.*, Magnetically mediated superconductivity in heavy fermion compounds. *Nature* **394**, 39 (1998).

[17] Smith, R. W. & Keszler, D. A., Syntheses and Crystal Structures of the alpha- and beta-forms of the Orthoborate $Sr_2Cu(BO_3)_2$. *J. Solid State Chem.* **81**, 305 (1989).

[18] Sakurai, H., Tsuboi, N., Yoshimura, K., & Kosuge, K., Spin-Singlet State of $A_2CuB_2O_6$ (A=Sr, Ba) with a Layered Structure. *J. Phys. Soc. Jpn.* **71**, 999 (2001).

[19] Kageyama, H. *et al.*, Anomalous Magnetizations in Single Crystalline $SrCu_2(BO_3)_2$. *J. Phys. Soc. Jpn.* **68**, 1821 (1999).

[20] Sparta, K. M. & Roth, G., Reinvestigation of the structure of $BaCuSi_2O_6$ - evidence for a phase transition at high temperature. *Act. Crys. B.* **60**, 491 (2004).

[21] Sasago, Y. *et al.*, Temperature-dependent spin gap and singlet ground state in $BaCuSi_2O_6$. *Phys. Rev. B.* **55**, 8357 (1997).

[22] Matsubara, T. and Matsuda, H., A Lattice Model of Liquid Helium. *Prog. Theor. Phys.* **16**, 416 (1956).

[23] Mila, F., Ladders in a magnetic field: a strong coupling approach. *Eur Phys J B.* **6**, 201 (1998).

[24] Batista, C. D., private communication.

[25] Kawashima, N., Quantum Critical Point of the XY Model and Condensation of Field-induced Quasiparticles in Dimer Compounds. *J. Phys. Soc. Jpn.* **73**, 3219 (2004).

[26] Okamoto, H., Ce-Sb (Cerium-Antimony), *J. Phase Equilibria*, **22**, 88 (2001).

[27] Berke, H., Chemistry in Ancient Times: The Development of Blue and Purple Pigments. *Angew. Chem. Int. Ed.* **41**, 2483 (2002).

[28] Canfield, P. C. & Fisk, Z., Growth of single crystals from metallic fluxes. *Philos. Mag. B* **65**, 1117 (1992).

[29] Stern, R., private communication.

[30] Ronnow, H., private communication.

[31] Sebastian, S. E., *et al.*, High-field behavior of the spin gap compound $Sr_2Cu(BO_3)_2$. *Phys. Rev. B* **71**, 212405 (2005).

[32] Mozharivskyj, Y. & Miller, G., private communication.

[49] Yosida, K., *Theory of Magnetism* (Springer, 1998).

[34] Smith, R. W. & Keszler, D. A., Structure of $Ba_2Cu(BO_3)_2$. *Acta Cryst.* **c46**, 370 (1990).

[35] Zvyagin, S. & Krzystek, J., private communication.

[36] Watson, R. E. & Freeman, A. J., Hartree-Fock atomic scattering factors for the iron transition series. *Acta Cryst.* **14**, 27 (1961).

[37] Furrer, A. & Güdel, H. U., Interference Effects in Neutron Scattering from Magnetic Clusters. *Phys. Rev. Lett.* **39**, 657 (1977).

[38] Freltoft, T. *et al.*, Magnetic form factor of Cu in La_2CuO_4. *Phys. Rev. B.* **37**, 137 (1988).

[39] Akimitsu, J. & Ito, Y., Magnetic Form Factor of Cu^{2+} in K_2CuF_4. *J. Phys. Soc. Jpn.* **40**, 1621 (1976).

[40] Troyer, M., Tsunetsugu, H., & Würtz, D., Thermodynamics and spin gap of the Heisenberg ladder calculated by the look-ahead Lanczos algorithm. *Phys. Rev. B* **50**, 13515 (1994).

[41] Rüegg, Ch. *et al.*, Quantum Statistics of Interacting Dimer Spin Systems. *Phys. Rev. Lett.* **95**, 267201 (2005).

[42] Wessel, S., Olshanii, M., & Haas, S., Field-Induced Magnetic Order in Quantum Spin Liquids. *Phys. Rev. Lett.* **87**, 206407 (2001).

[43] Jaime, M. *et al.*, Magnetic-Field-Induced Condensation of Triplons in Han Purple Pigment $BaCuSi_2O_6$. *Phys. Rev. Lett.* **93**, 087203 (2004).

[44] Shindo, Y. & Tanaka, H., Localization of Spin Triplets in $Tl_{1-x}K_xCuCl_3$. *J. Phys. Soc. Jpn.* **73**, 2642 (2004).

[45] McDonald, R., private communication.

[46] Samulon, E. *et al.*, Low temperature structural phase transition and incommensurate lattice modulation in the spin gap compound $BaCuSi_2O_6$, www.arXiv.org/cond-mat/0512560 (2005).

[47] Preliminary inelastic neutron scattering measurements also indicate multiple values of J (Rüegg, Ch., private communication).

[48] Moriya, T., Anisotropic Superexchange Interaction and Weak Ferromagnetism. *Phys. Rev.* **120**, 91 (1960).

[49] Yosida, K., *Theory of Magnetism, Springer Series in Solid State Sciences volume 122*, Springer (Berlin, 1998).

[50] Hill, S., private communication.

[51] Zvyagin, S., Spin-Triplet Excitons in the $S = 1/2$ Gapped Antiferromagnet $BaCuSi_2O_6$: Electron Paramagnetic Resonance Studies, www.arxiv.org/cond-mat/0601017 (2006).

[52] Summers, M., private communication.

[53] Schneider-Muntau, H. J., Toth, J., & Weijers, H. W., Generation of the Highest Continuous Magnetic Fields. *IEEE Transactions on App. Superconductivity* **14**, 1245 (2004).

[54] Islam, Z., private communication.

[55] Rüegg, Ch. *et al.*, Bose-Einstein condensation of the triplet states in the magnetic insulator $TlCuCl_3$. *Nature* **423**, 62 (2003).

[56] Tanaka, H. *et al.*, Observation of Field-Induced Transverse Néel Ordering in the Spin Gap System $TlCuCl_3$. *J. Phys. Soc. Jpn.* **70**, 939 (2001).

[57] Oosawa, A. *et al.*, Specific heat study of the field-induced magnetic ordering in the spin-gap system $TlCuCl_3$, *Phys. Rev. B.* **63**, 134416 (2001).

[58] Campostrini, M. *et al.*, Critical behavior of the three-dimensional XY universality class. *Phys. Rev. B* **63**, 214503 (2001).

[59] Kawashima, N., private communication.

[60] Nohadani, O. *et al.*, Universal scaling at field-induced magnetic phase transitions. *Phys. Rev. B.* **69**, 220402(R) (2004).

[61] Harris, A. B., Effect of random defects on the critical behaviour of Ising models. *J. Phy. C.* **7**, 1671-1692 (1974).

[62] Vojta, T. & Sknepnek, R., Critical points and quenched disorder: from Harris criterion to rare regions and smearing. *Physica Status Solidi B.* **241**, 2118-27 (2004).

[63] Xu, C. & Moore, J. E., Geometric criticality for transitions between plaquette phases in integer-spin kagome XXZ antiferromagnets. *Phys. Rev. B* **72**, 064455-064459 (2005).

[64] Batista, C. D. & Nussinov, Z., Generalized Elitzur's theorem and dimensional reductions. *Phys. Rev. B* **72**, 045137-045146 (2005).

[65] Tewari, S., Toner, J. & Chakravarty, S., Floating phase in a dissipative Josephson junction array. *Phys. Rev. B* **72**, 060505(R) (2005).

[66] Horovitz, B., Phase transitions in layered superconductors. *Phys. Rev. B* **45**, 12632-12635 (1992).

[67] Pershan, P. S., *Structure of Liquid Crystal Phases* (World Scientific, Singapore, 1988).

[68] Emery, V. J. *et al.*, Quantum Theory of the Smectic Metal State in Stripe Phases. *Phys. Rev. Lett.* **85**, 2160-2163 (2000).

[69] O'Hern, C. S., Lubensky, C. S. & Toner, J., Sliding Phases in XY Models, Crystals, and Cationic Lipid-DNA Complexes. *Phys. Rev. Lett* **83**, 2745-2748 (1999).

[70] Fisher, D. S. & Hohenberg, P. C., Dilute Bose gas in two dimensions. *Phys. Rev. B* **37**, 4936-4943 (1988).

[71] Maltseva, M. and Coleman, P., Failure of geometric frustration to preserve a quasi-two-dimensional spin fluid. *Phys. Rev. B* **72**, 174415-1(R)-174415-5(R) (2005).

[72] Sachdev, S., Quantum Criticality: Competing Ground States in Low Dimensions. *Science* **288**, 475-480 (2000).

[73] Stockert, O. *et al.*, Two-Dimensional Fluctuations at the Quantum-Critical Point of $CeCu_{6-x}Au_x$. *Phys. Rev. Lett.* **80**, 5627-5630 (1998).

[74] Senthil, T. *et al.*, Deconfined Quantum Critical Points. *Science* **303**, 1490-1494 (2004).

[75] Millis, A. J., Effect of a nonzero temperature on quantum critical points in itinerant fermion systems. *Phys. Rev. B* **48**, 7183-7196 (1993).

[76] Glazkov, V. N. *et al.*, Spin-resonance modes of the spin-gap magnet $TlCuCl_3$ *Phys. Rev. B* **69**, 184410-184418 (2004).

[77] Rüegg, Ch. *et al.*, Pressure-Induced Quantum Phase Transition in the Spin-Liquid $TlCuCl_3$. *Phys. Rev. Lett.* **93**, 257201 (2004).